

ISSN 0352-9045

Informacije MIDEM

*Journal of Microelectronics,
Electronic Components and Materials*
Vol. 46, No. 3(2016), September 2016

*Revija za mikroelektroniko,
elektronske sestavne dele in materiale*
letnik 46, številka 3(2016), September 2016



Informacije MIDEM 3-2016

Journal of Microelectronics, Electronic Components and Materials

VOLUME 46, NO. 3(159), LJUBLJANA, SEPTEMBER 2016 | LETNIK 46, NO. 3(159), LJUBLJANA, SEPTEMBER 2016

Published quarterly (March, June, September, December) by Society for Microelectronics, Electronic Components and Materials - MIDEM.
Copyright © 2016. All rights reserved. | Revija izhaja trimesečno (marec, junij, september, december). Izdaja Strokovno društvo za mikroelektroniko, elektronske sestavne dele in materiale – Društvo MIDEM. Copyright © 2016. Vse pravice pridržane.

Editor in Chief | Glavni in odgovorni urednik

Marko Topič, University of Ljubljana (UL), Faculty of Electrical Engineering, Slovenia

Editor of Electronic Edition | Urednik elektronske izdaje

Kristijan Brecl, UL, Faculty of Electrical Engineering, Slovenia

Associate Editors | Odgovorni področni uredniki

Vanja Ambrožič, UL, Faculty of Electrical Engineering, Slovenia

Arpad Bürmen, UL, Faculty of Electrical Engineering, Slovenia

Danjela Kuščer Hrovatin, Jožef Stefan Institute, Slovenia

Matija Pirc, UL, Faculty of Electrical Engineering, Slovenia

Matjaž Vidmar, UL, Faculty of Electrical Engineering, Slovenia

Editorial Board | Uredniški odbor

Mohamed Akil, ESIEE PARIS, France

Giuseppe Buja, University of Padova, Italy

Gian-Franco Dalla Betta, University of Trento, Italy

Martyn Fice, University College London, United Kingdom

Ciprian Iliescu, Institute of Bioengineering and Nanotechnology, A*STAR, Singapore

Malgorzata Jakubowska, Warsaw University of Technology, Poland

Marc Lethiecq, University of Tours, France

Teresa Orłowska-Kowalska, Wrocław University of Technology, Poland

Luca Palmieri, University of Padova, Italy

International Advisory Board | Časopisni svet

Janez Trontelj, UL, Faculty of Electrical Engineering, Slovenia - Chairman

Cor Claeys, IMEC, Leuven, Belgium

Denis Donlagić, University of Maribor, Faculty of Elec. Eng. and Computer Science, Slovenia

Zvonko Fazarinc, CIS, Stanford University, Stanford, USA

Leszek J. Golonka, Technical University Wrocław, Wrocław, Poland

Jean-Marie Haussonne, EIC-LUSAC, Octeville, France

Barbara Malič, Jožef Stefan Institute, Slovenia

Miran Mozetič, Jožef Stefan Institute, Slovenia

Stane Pejovnik, UL, Faculty of Chemistry and Chemical Technology, Slovenia

Giorgio Pignatelli, University of Perugia, Italy

Giovanni Soncini, University of Trento, Trento, Italy

Iztok Šorli, MIKROIKS d.o.o., Ljubljana, Slovenia

Hong Wang, Xi'an Jiaotong University, China

Headquarters | Naslov uredništva

Uredništvo Informacije MIDEM

MIDEM pri MIKROIKS

Stegne 11, 1521 Ljubljana, Slovenia

T. +386 (0)1 513 37 68

F. + 386 (0)1 513 37 71

E. info@midem-drustvo.si

www.midem-drustvo.si

Annual subscription rate is 160 EUR, separate issue is 40 EUR. MIDEM members and Society sponsors receive current issues for free. Scientific Council for Technical Sciences of Slovenian Research Agency has recognized Informacije MIDEM as scientific Journal for microelectronics, electronic components and materials. Publishing of the Journal is cofinanced by Slovenian Research Agency and by Society sponsors. Scientific and professional papers published in the journal are indexed and abstracted in COBISS and INSPEC databases. The Journal is indexed by ISI® for Sci Search®, Research Alert® and Material Science Citation Index™. |

Letna naročnina je 160 EUR, cena posamezne številke pa 40 EUR. Člani in sponzorji MIDEM prejema posamezne številke brezplačno. Znanstveni svet za tehnične vede je podal pozitivno mnenje o reviji kot znanstveno-strokovni reviji za mikroelektroniko, elektronske sestavne dele in materiale. Izdajo revije sofinancirajo ARRS in sponzorji društva. Znanstveno-strokovne prispevke objavljene v Informacijah MIDEM zajemamo v podatkovne baze COBISS in INSPEC. Prispevke iz revije zajema ISI® v naslednje svoje produkte: Sci Search®, Research Alert® in Materials Science Citation Index™.

Content | Vsebina

Review scientific paper

S. Pevec, B. Lenardič, D. Đonlagić: 113
 Micromachining of All-Fiber Photonic Micro-
 Structures for Microfluidic Applications

I. M. Milosavljević, D. P. Krčum, L. V. Saranovac: 120
 Design and Analysis of Differential Passive Circuits
 for I/Q Generation in 60 GHz Integrated Circuits

Pregledni znanstveni članek

S. Pevec, B. Lenardič, D. Đonlagić:
 Mikroobdelava povsem vlakenskih fotonskih
 mikrostruktur za področje mikrofluidnih aplikacij

I. M. Milosavljević, D. P. Krčum, L. V. Saranovac:
 Načrtovanje in analiza diferencialnih pasivnih vezij
 za generiranje I/Q v 60 GHz integriranih vezij

Original scientific paper

W. Tangsrirat: 130
 Dual-Mode Sinusoidal Quadrature Oscillator with
 Single CCCTA and Grounded Capacitors

T. Pečnik, S. Glinšek, B. Kmet, B. Malič: 136
 Solution-derived $Ba_{0.5}Sr_{0.5}TiO_3$ Thin-film Capacitors
 in Metal-insulator-metal Configuration

R. Kimovec, H. Helmers, A. W. Bett, M. Topič: 142
 Temperature and Injection Current dependent
 Electroluminescence for Evaluation of
 Single-Junction Single-Segment
 GaAs Laser Power Converter

M. Podhraški, J. Trontelj: 149
 Linear Incremental Displacement Measurement
 System with Microtransformers

M. Makarovič, J. Walker, E. Khomyakova, A. Benčan,
 B. Malič, T. Rojac: 154
 Control of Electrical Conductivity in $0.7BiFeO_3-$
 $0.3SrTiO_3$ Ferroelectric Ceramics Via Thermal Treat-
 ment in Nitrogen Atmosphere and Mn Doping

Front page:
 Spatial electroluminescence image of six-segment
 GaAs laser power converter (Kimovec et al.)

Izvirni znanstveni članki

W. Tangsrirat:
 Dvojni sinusni kvadrantni oscillator z enosnim CC-
 CTA in ozemljenimi kondenzatorji

T. Pečnik, S. Glinšek, B. Kmet, B. Malič:
 Tankoplastni kondenzatorji na osnovi $Ba_{0.5}Sr_{0.5}TiO_3$,
 pripravljenega s sintezo v raztopini, s konfiguracijo
 kovina - dielektrik - kovina

R. Kimovec, H. Helmers, A. W. Bett, M. Topič:
 Vpliv temperature in vzbujalnega toka na elektro-
 luminescenca enosegmentnih enospojnih
 pretvornikov laserske moči

M. Podhraški, J. Trontelj:
 Sistem z mikrotransformatorji za inkrementalno
 merjenje linearnega pomika

M. Makarovič, J. Walker, E. Khomyakova, A. Benčan,
 B. Malič, T. Rojac:
 Kontrola električne prevodnosti v feroelektrični
 keramiki $0.7BiFeO_3-0.3SrTiO_3$ z žganjem v dušikovi
 atmosferi in dopiranjem z Mn

Naslovnica:
 Slika prostorske elektroluminescenca šest-
 segmentnega pretvornika laserske moči
 narejenega iz GaAs (Kimovec et al.)

Editorial | Uvodnik

Dear Reader,

In summer all journals listed in SCIE eagerly waited for the Journal Citation Reports® (JCR) by Thompson Reuters and journals' impact factor (IF) values for 2015. In early autumn also data for SNIP (Source Normalized Impact per Paper) — one of several metrics available on ScienceDirect — in 2015 came out. IFs are counted as a metrics that provide a snapshot of performance and help establish benchmarks for growth. We are pleased to see that metrics for our journal is improving:

JCR IF (2015) = 0,433 and ScienceDirect SNIP (2015) = 0,393.

Editorial Board is pleased that efforts and dedication to high quality harvest success.

Associate Editor Professor Slavko Amon decided to step down due to retirement. We are truly grateful for his 14 years of dedicated work and contribution to the success of the journal.

Associate Editor Professor Andrej Žemva decided to step down due to too many duties, especially since he is the Editor-in-Chief of another scientific journal *Elektrotehniški vestnik*. We are truly grateful for his 5 years of dedicated work and contribution to the success of the journal.

A new member of Editorial Board, Professor Arpad Buermen has been elected by Executive Board of the MIDE M Society in June 2016. He will serve as the Associate Editor for Electronics.

Please join the members of Editorial Board of the *Informacije MIDE M - Journal of Microelectronics, Electronic Components and Materials* in thanking Prof. Slavko Amon and Prof. Andrej Žemva for their valuable contribution and congratulating Prof. Arpad Buermen on his new position as the Associate Editor for Electronics!

We look forward to receiving your next manuscript(s) in our on-line submission platform:

<http://ojs.midem-drustvo.si/index.php/InfMIDEM>

Last but not least, this issue brings 2 review and 5 original scientific papers. Enjoy reading them!

Prof. Marko Topič
Editor-in-Chief

P.S.

All papers published in *Informacije MIDE M* –Journal of Microelectronics, Electronics Components and Materials (since 1986) can be access electronically for free at <http://midem-drustvo.si/journal/home.aspx>. A search engine is provided to use it as a valuable resource for referencing previous published work and to give credit to the results achieved from other groups.

Micromachining of All-Fiber Photonic Micro-Structures for Microfluidic Applications

Simon Pevec¹, Borut Lenardič² and Denis Donlagić¹

¹University of Maribor, Faculty of Electrical Engineering and Computer Science, Maribor, Slovenia

²Optacore d.o.o., Ljubljana, Slovenia

Abstract: Maskless micromachining of all-fiber photonics' structures, based on the selective etching of structure forming optical fibers (SFF) is presented. A maskless micromachining process can reform or reshape a section of an optical fiber into a complex 3D photonic microstructure. This proposed micromachining process is based on the introduction of phosphorus pentoxide (P₂O₅) into silica glass through standard fiber manufacturing technology. Micro-machining is presented as a highly effective tool for the realization of new solutions in the design of optical sensors and microfluidic devices.

Keywords: Micromachining; optical fibers; optical sensors; phosphorus pentoxide; selective etching; microstructures.

Mikroobdelava povsem vlakenskih fotonских mikrostruktur za področje mikrofluidnih aplikacij

Izvleček: Predstavljena je mikroobdelava na osnovi selektivnega jedkanja posebnega optičnega vlakna v namene izdelave mikrofotonskih struktur. Proces mikroobdelave brez maskiranja sloni na vgradnji fosforjevega pentoksida (P₂O₅) v steklena optična vlakna skozi postopek standardne proizvodnje optičnih vlaken. Mikroobdelava je predstavljena kot zelo učinkovito orodje za realizacijo novih rešitev na področju načrtovanja senzorjev in mikrofluidnih naprav.

Ključne besede: Mikroobdelava; optična vlakna; optični senzorji; fosforjev pentoksid; selektivno jedkanje; mikrostrukture.

*Corresponding Author's e-mail: simon.pevec@um.si

1 Introduction

Photonic micro-structures are being increasingly used in a number of applications, ranging from optical telecommunications [1-3] to biomedical sensor [4-6]. Direct implementation of micro-devices can extend their use and allow many important advantages and novel functionality. Existing solutions for optical fiber micromachining are mostly based on laser techniques. Reshaping of SiO₂ optical fiber is typically realized by laser sources operating in ultraviolet (UV) or middle-infrared (MIR), where they have sufficient absorption of light in the SiO₂ [7]. UV excimer lasers [8, 9] and femtosecond lasers [10-14] have been successfully applied as efficient tool for optical fiber micromachining. However all direct laser techniques have a common need for individual and precision guiding of the laser beam over cylindrical optical fiber, which is complex, expen-

sive and time-consuming task. Beside laser techniques, there are also other techniques like lithographic processes [15, 16], micromachining by dry etching [17] and by focused ion beam [18-21]. Lithographic process requires many process steps, dry etching is related with time-consuming and low selectivity etching, focused ion beam technique is also time-consuming and cost-inefficient and as such unsuitable for production.

This paper presents a cost effective, mask-less micromachining process that can re-shape a section of an optical fiber into a complex 3D photonic microstructure. Micromachining based on selective etching provides a unique way for efficient design and production of complex 3D photonic all-fiber microstructures and devices [22-25]. The selective chemical etching utilizes a phenomenon where the introduction of dopants into

silica glass affects the etching rate of the glass when exposed to etching solution (usually HF). When purposely designed and properly doped optical fibers are combined/fusion spliced with standard fibers, selective etching can be exploited for the manufacturing of micro-structures on the tip, along or within the optical fibers. Structures produced by this process are made entirely of silica glass, do not utilize any adhesives or foreign materials, and can thus sustain harsh chemical and temperature conditions. Thus selective etching based micromachining involves production of SFF that involves preform production, mechanical reshaping of the preform and fiber drawing, fusion-splicing of these fibers with standard fibers, and etching of such assemblies into final photonics microstructures or devices. Thus after proper SFF production, the device production is accomplished by a sequence of fiber cleave and splice sequence(s) that are followed by (wet) etching.

This proposed micromachining process is mainly based on the introduction of P_2O_5 into silica, which can be effectively removed upon exposing the fiber to the etching medium. These preferentially etchable P_2O_5 doped areas within the fiber cross section can thus serve as sacrificial layers, thus allowing for the economical creation of complex all-fiber devices, which will be presented as result of proposed micromachining technology.

2 Etching solutions and etching selectivity

Etching selectivity S of doped region is defined as the ratio between the etching rate of the doped (v_{xx}), and that of the pure silica (v_{SiO_2}).

$$S = \frac{v_{xx}}{v_{SiO_2}} \quad (1)$$

The S depends on the dopant type, dopant concentration, etching medium and temperature. During investigation several differently doped fiber preforms contained between one and five different doped layers of P_2O_5 concentrations were produced to study the impact of P_2O_5 .

Preforms with known refractive index profiles (one typical refractive index profile is shown in Fig. 1) were in first step cut into approximately 1 to 2 cm long samples using a low speed diamond saw. The samples were then etched in etching medium. Depending on the composition of the doped glass, an etching time of between 1 min and 3 h was used to obtain well-defined surface relief. The etching vessel was temperature stabilized and

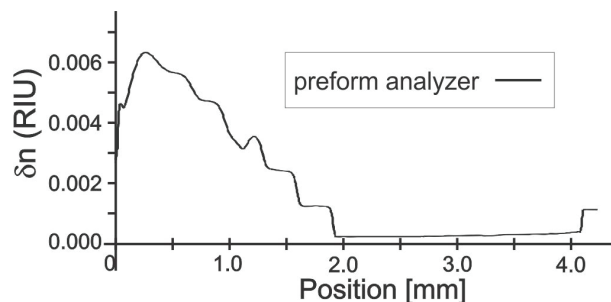


Figure 1: Preform analyzer data obtained after MCVD preform production.

also vibrated to provide acid-mixing and the removal of etching by-products from the sample's surface. The etched-preform samples were then cut in the axial direction through their centers, and were then analyzed/measured under an optical microscope. An example of such an etched preform measurement is shown in Fig. 2. The initial preform diameter and dimensions of the removed doped region were then used to determine the average v_{xx}/v_{SiO_2} ratio of the individual layers of etched preform.

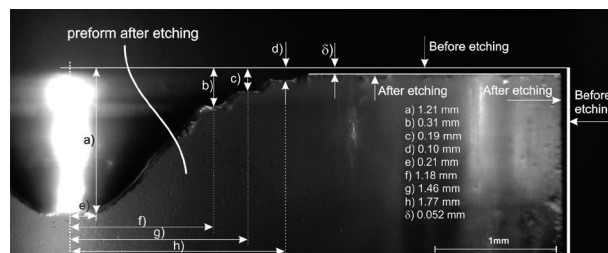


Figure 2: Selectivity measurement of P_2O_5 doped preform obtained by comparison of geometrical shape of preform before and after etching.

The preform analyzer data and the etching data were then combined to obtain a relationship between the etching selectivity S and the refractive index change caused by doping, which was further correlated to the dopant molar concentration [26].

Some dopants strongly increase S , while the others provide limited effect on the S at comparable concentration levels. From all researched dopants, P_2O_5 proved to be of particular interest for fiber micromachining. As shown in Fig. 3, the P_2O_5 doping of silica can provide very high etching selectivity S , even at low P_2O_5 concentrations. Composition of an etching agent can also strongly influence the etching selectivity. Other dopants can provide other benefits, such as strong index increase whilst providing very limited impact on the S (e.g. TiO_2).

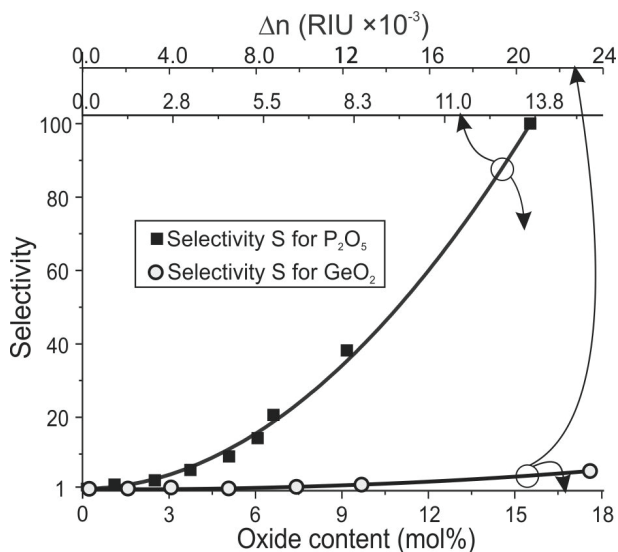


Figure 3: Selectivity as a function of P_2O_5 and GeO_2 in 40 % hydrofluoric acid at 25°C.

Great impact on selectivity has also temperature of hydrofluoric acid (HF), where by reducing the temperature from 40 to -25 °C, selectivity of P_2O_5 doped sample with higher dopant concentration (7.9 mol %) is increased from 28 to 39 as shown in Fig. 4.

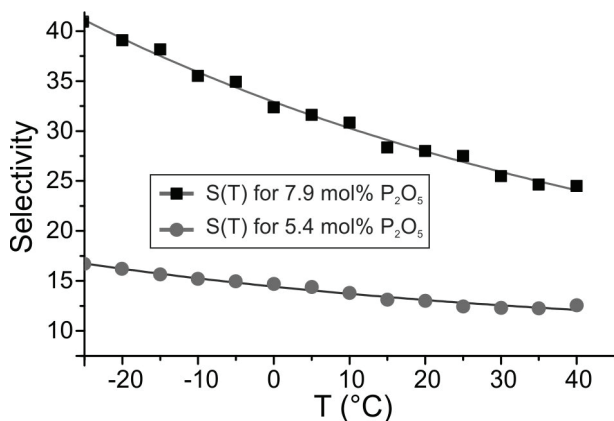


Figure 4: Selectivity as a function of temperature for two different P_2O_5 doped preform, etched in 40 % HF.

Reducing the temperature has also negative impact on etching process, because it significantly slows down the absolute etching rate and thus increase the time required for the formation of the microstructure. Furthermore by adding isopropyl-alcohol (IPA) to HF, IPA-HF etching solutions work particularly well in combination with P_2O_5 doping where doubling or even tripling of the etching selectivity can be achieved.

3 Micromachining of all-fiber photonics devices

Fiber devices are created by splicing short section of SFF at the end-of lead or in-between two lead fibers. One, very simple example produced by selective etching based on P_2O_5 doping is shown in Fig. 6. Here the micro-resonator on the optical fiber tip is presented. Micro-resonators have found applications within various photonic systems [27] such as sensors, filters, coupling devices, etc., but are difficult to produce. A cross section of the SFF, used for creation of resonator, is shown in Fig. 5 and consists of pure silica core, a large P_2O_5 region (5.7 mol%), and a thin pure SiO_2 outer-layer with the same glass transition temperature as the lead-in fiber-cladding and, thus, allows for straightforward splicing between them.

In this case the SFF was spliced between two coreless fibers, where the second coreless fiber was shortened to a length of about 15 μm as shown in Fig. 6b and then etched for sufficient time in HF.

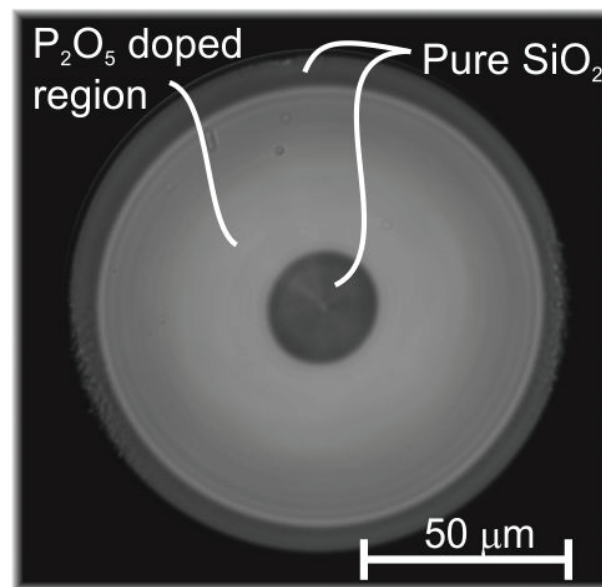


Figure 5: Optical microscopic cross-sectional view of SFF intended for micro-structure formation.

The etchant first uniformly etched the entire structure, but once the pure silica outer-layer of the SFF was removed and HF came into contact with the P_2O_5 -doped region, it preferentially removed this region entirely, leaving behind the final structure shown in Fig. 6a. The total etching time was 12 min in 40 % HF at 25 °C.

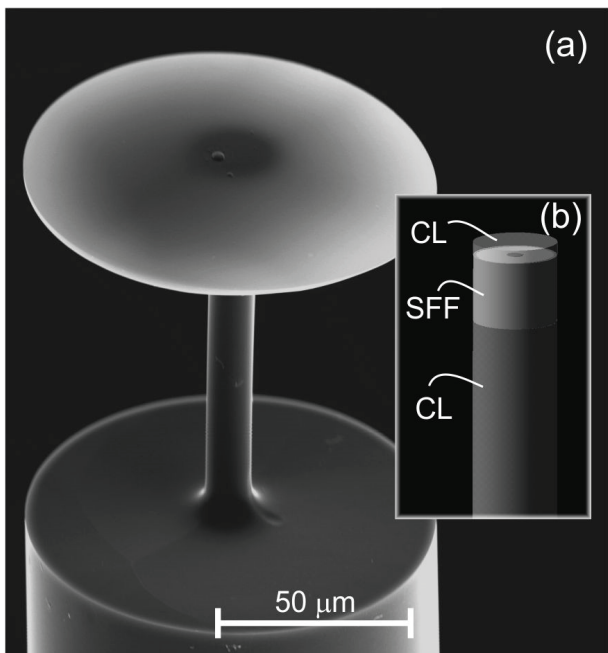


Figure 6: (a) Scanning electron microscope view of the produced micro-resonator, (b) Fiber structure before etching (after cleaving and splicing).

Depending of the device design, etching of SFF can be performed before or after splicing. Below are given few more typical examples of structures produced by application of splicing, cleaving and etching of SFFs.

The first device shown in Fig. 7a is an all-fiber optical microcell that allows for the direct insertion of liquids, gases or solids within the optical path of the transmission fiber. The micro-cell can be used as a transmission cell or as a miniature Fabry-Perot resonator. The total transmission loss of the microcell in Fig. 7a was less than 1 dB at 1550 nm, when immersed in water. Various lengths of micro-cells can be produced ranging from few tenths to few 1000 μm.

Another example device that can be effectively produced by this method is shown in Fig. 7b, and presents a miniature, all-silica, dual-parameter Fabry-Perot sensor for simultaneous measurement of surrounding fluid's refractive index (RI) and temperature. This sensor permits a full temperature-compensated high resolution RI measurement in range of 10^{-7} RIU, that can be used to determine very small changes in fluid structure or composition. All-silica design provides high chemical and thermal inertness, while the miniature size provides opportunities for measuring very small (nL) fluid volumes.

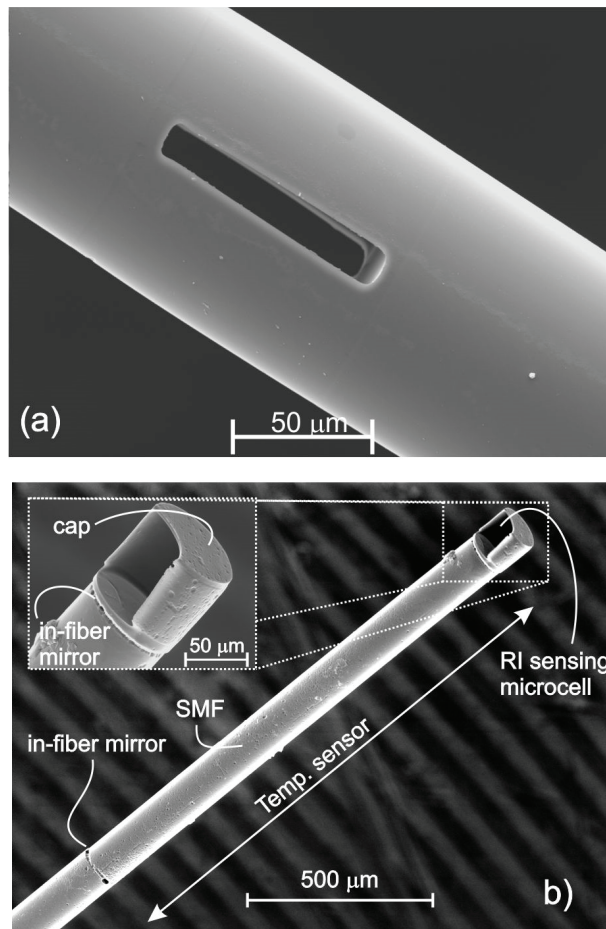


Figure 7: Microstructure devices: (a) Microcell [28], (b) Refractive index – temperature sensor [29].

Next example shown in Fig. 8a presents an all glass, Fabry-Perot, fiber-optic pressure sensor. It is the world's smallest commercial available pressure sensor [30], with outer diameter less than 125 μm, and is produced by proposed technology in few sequential steps on the tip of multi-mode lead-in optical fiber. Membrane thickness for typical pressure sensor is round 2 μm, which allow high pressure sensitivity needed for medical performance requirements. A sensitivity of 1100 nm/bar was also achieved which is, to our knowledge, the highest all-glass miniature sensor sensitivity reported in the literature. This robust sensor also demonstrated very high resistance to overload, which is an important advantage for practical usage of the sensor in realistic applications. The proposed miniature all-glass pressure sensor design is, therefore, a good candidate for applications where size, cost, material inertness, mechanical and chemical resistance as well as insensitivity to electromagnetic interferences are important concerns. Beside all advantages coming from all silica glass optical fiber design, this sensor can achieve high resolution and repeatability, very low drift, and fast response time.

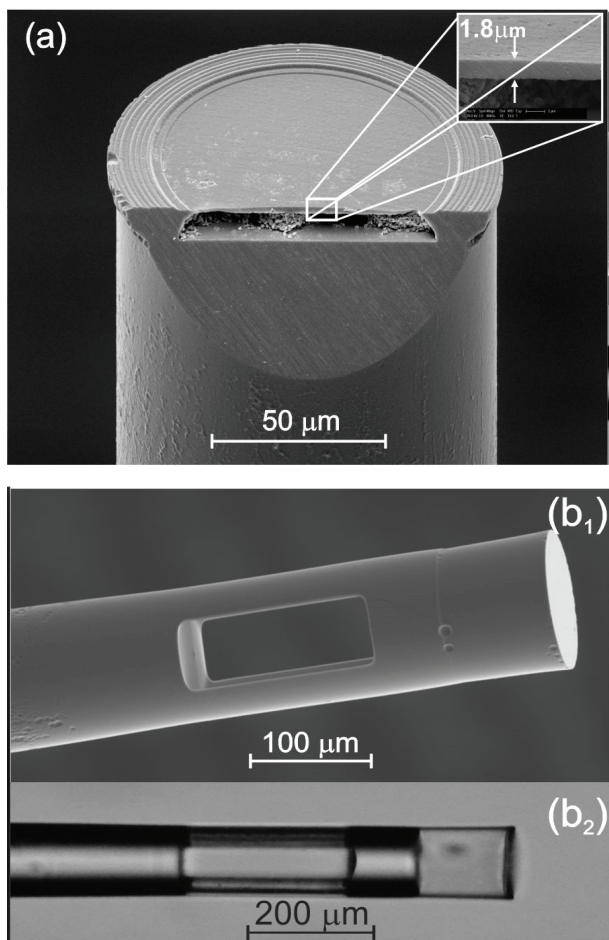


Figure 8: Microstructure devices: (a) Pressure sensor [31], (b₁) SEM photo and (b₂) optical microscope photo of Pressure – refractive index sensor respectively [32].

Another example shows one of more complex devices that can be produced by proposed technology, where microcell with pressure sensor was joined in series; it is multi parameter (multi cavity) Fabry-Perot sensor for simultaneous measurements of pressure and refractive index. Figure 8 (b₁) shows scanning microscope (SEM) image, and Fig. 8 (b₂) shows the same sensor under an optical microscope. These sensor was created at the tip of an optical fiber with a diameter that is equal to the standard fiber diameter, and length that does not exceeded 600 μm. High measurement resolutions better than 0.1 mBar and 2×10^{-5} RIU can be achieved by using spectral interrogation and a FT-based measurement algorithm.

Next example in Fig. 9a shows nanowire-based refractive index sensor created on the tip of a single mode optical fiber configured as Fabry-Perot interferometer. Proposed micromachining technique including tapering allows creation of fiber coupled silica nanowires with radius between 200 and 600 nm. Nanowire sensor is made entirely of silica and includes a mechanical

structure that provides stable operation and easy handling and packaging. High measuring spectral sensitivity as 800 nm/RIU and low temperature sensitivity in water are typical sensor characteristics. Sensor might be an especially attractive platform for use in compact biochemical sensors, which utilize active surfaces, for example in various label-free detection-sensing schemes.

One more example presented in Fig. 9b shows Fabry-Perot strain sensor created on the tip of a standard multi-mode fiber. Sensor's great advantage is simplicity of its production process that includes production of SFF (inset on Fig. 9b), which is cleaved, etched, and spliced between lead fibers in order to form final sensor. Tested sensors were successfully applied to strain-measurements exceeding 3000 με, which accommodate most of requirements encountered in practical industrial applications. A strain-resolution of 0.5 με, high temperature range exceeding 650 °C, and low temperature intrinsic sensitivity below 0.04 nm/°C are typical characteristics for that kind of sensor.

The last device shown in row is miniature all-silica fiber-optic sensor for simultaneous measurements of relative humidity (RH) and temperature. The sensor is composed of two cascaded Fabry-Perot interferometers (FPIs) as shown in Fig. 9c. The first FPI consists of a short silica micro-wire (diameter is cca. 13 μm) coated by a thin layer of porous silica, and forms a RH sensing part. The second section created on the sensor tip forms a temperature measuring part. The typical total length of produced sensor is less than 2 mm, while diameter doesn't exceed 125 μm. The sensor has good dynamic performances (rise time in few second range), it cover broad RH measuring range (0-100 %RH), and has linear characteristics for both measurement parameters with sensitivity of 0.48 degree/%RH and 3.7 degree/°C.

All sensors and devices have all glass structure, high environmental robustness, and a miniature design, which in any of the cases does not exceed the diameter of a standard optical fiber (i.e. 125 μm) and has an active length of less than 1.5 mm (more details can be found in appropriate references). All devices are robust and allow easy handling and packaging, especially those designed and fabricated on the tip of the optical fiber. Small dimensions, chemical resistance and robustness make sensors suitable for microfluidic applications.

Since a single customized SFF production may result in the manufacturing of a large number of devices, the proposed process potentially presents a versatile and cost-efficient way of producing all-fiber devices or device sub-assemblies.

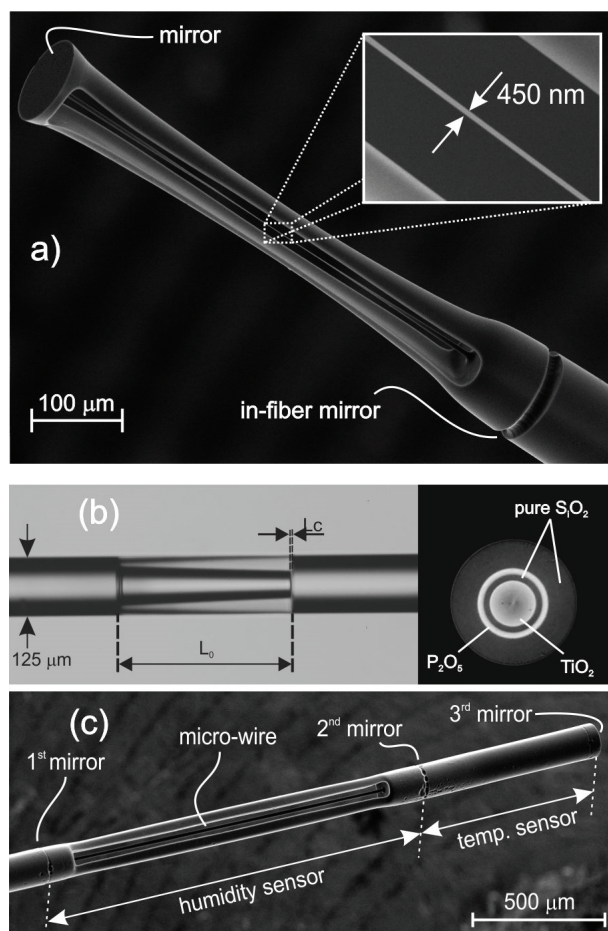


Figure 9: Microstructure devices: (a) Nano-wire refractive index sensor [33], (b) Strain sensor [34], and (c) Relative humidity – temperature sensor [35].

4 Conclusions

An effective technique for production of all fiber devices through application of selective etching and specially designed SFF was presented. The proposed technique provides versatile and potential cost-efficient way of all fiber device manufacturing through design and production of specialty SFFs.

5 Acknowledgments

Authors would like to thank to Slovenian research agency (Grant No. P2-0368 and L2-5494) and Optacore team for supplying specialty fiber required for the sensor production.

6 References

1. H. Toshiyoshi, "Micro electro mechanical devices for fiber optic telecommunication," *Jsm Int J B-Fluid T* 47, 439-446 (2004).
2. A. Q. Liu and X. M. Zhang, "A review of MEMS external-cavity tunable lasers," *J Micromech Microeng* 17, R1-R13 (2007).
3. W. H. Ko, "Trends and frontiers of MEMS," *Sensor Actuat a-Phys* 136, 62-67 (2007).
4. X. D. Hoa, A. G. Kirk, and M. Tabrizian, "Towards integrated and sensitive surface plasmon resonance biosensors: A review of recent progress," *Biosens Bioelectron* 23, 151-160 (2007).
5. T. Takahata, K. Matsumoto, and I. Shimoyama, "A wide wavelength range optical switch using a flexible photonic crystal waveguide and silicon rods," *J Micromech Microeng* 20(2010).
6. R. Bashir, "BioMEMS: state-of-the-art in detection, opportunities and prospects," *Adv Drug Deliver Rev* 56, 1565-1586 (2004).
7. R. Kitamura, L. Pilon, and M. Jonasz, "Optical constants of silica glass from extreme ultraviolet to far infrared at near room temperature," *Appl Optics* 46, 8118-8133 (2007).
8. J. Greuters and N. H. Rizvi, "Laser micromachining of optical materials with a 157nm fluorine laser," *P Soc Photo-Opt Ins* 4941, 77-83 (2003).
9. Z. L. Ran, Y. J. Rao, H. Y. Deng, and X. Liao, "Miniature in-line photonic crystal fiber etalon fabricated by 157 nm laser micromachining," *Opt Lett* 32, 3071-3073 (2007).
10. G. Della Valle, R. Osellame, and P. Laporta, "Micromachining of photonic devices by femtosecond laser pulses," *J Opt a-Pure Appl Op* 11(2009).
11. I. B. Sohn, M. S. Lee, J. S. Woo, S. M. Lee, and J. Y. Chung, "Fabrication of photonic devices directly written within glass using a femtosecond laser," *Opt Express* 13, 4224-4229 (2005).
12. Y. J. Rao, M. Deng, D. W. Duan, X. C. Yang, T. Zhu, and G. H. Cheng, "Micro Fabry-Perot interferometers in silica fibers machined by femtosecond laser," *Opt Express* 15, 14123-14128 (2007).
13. T. Wei, Y. K. Han, H. L. Tsai, and H. Xiao, "Miniaturized fiber inline Fabry-Perot interferometer fabricated with a femtosecond laser," *Opt Lett* 33, 536-538 (2008).
14. A. A. Said, M. Dugan, S. de Man, and D. Iannuzzi, "Carving fiber-top cantilevers with femtosecond laser micromachining," *J Micromech Microeng* 18(2008).
15. C. Liberale, G. Cojoc, P. Candeloro, G. Das, F. Gentile, F. De Angelis, and E. Di Fabrizio, "Micro-Optics Fabrication on Top of Optical Fibers Using Two-Photon Lithography," *Ieee Photonic Tech L* 22, 474-476 (2010).

16. H. Guckel, "High-aspect-ratio micromachining via deep x-ray lithography," *P IEEE* 86, 1586-1593 (1998).
17. J. Bierlich, J. Kobelke, D. Brand, K. Kirch, J. Dellith, and H. Bartelt, "Nanoscopic Tip Sensors Fabricated by Gas Phase Etching of Optical Glass Fibers," *Photonic Sensor* 2, 331-339 (2012).
18. Y. K. Kim, A. J. Danner, J. J. Raftery, and K. D. Choquette, "Focused ion beam nanopatterning for optoelectronic device fabrication," *IEEE J Sel Top Quant* 11, 1292-1298 (2005).
19. P. Olivero, S. Rubanov, P. Reichart, B. C. Gibson, S. T. Huntington, J. Rabeau, A. D. Greentree, J. Salzman, D. Moore, D. N. Jamieson, and S. Praver, "Ion-beam-assisted lift-off technique for three-dimensional micromachining of freestanding single-crystal diamond," *Adv Mater* 17, 2427-+ (2005).
20. D. Iannuzzi, S. de Man, C. J. Alberts, J. W. Berenschot, M. C. Elwenspoek, A. A. Said, and M. Dugan, "Fiber-top micromachined devices - art. no. 700403," 19th International Conference on Optical Fibre Sensors, Pts 1 and 2 7004, 403-403 (2008).
21. D. Iannuzzi, S. Deladi, V. J. Gadgil, R. G. P. Sanders, H. Schreuders, and M. C. Elwenspoek, "Monolithic fiber-top sensor for critical environments and standard applications," *Appl Phys Lett* 88(2006).
22. M. S. Ferreira, J. Bierlich, S. Unger, K. Schuster, J. L. Santos, and O. Frazao, "Post-Processing of Fabry-Perot Microcavity Tip Sensor," *IEEE Photonic Tech L* 25, 1593-1596 (2013).
23. S. Mononobe and M. Ohtsu, "Fabrication of a pencil-shaped fiber probe for near-field optics by selective chemical etching (vol 14, pg 2231, 1996)," *J Lightwave Technol* 15, 162-162 (1997).
24. S. Pevec, E. Cibula, B. Lenardic, and D. Donlagic, "Micromachining of Optical Fibers Using Selective Etching Based on Phosphorus Pentoxide Doping," *IEEE Photonics J* 3, 627-632 (2011).
25. R. M. Andre, S. Pevec, M. Becker, J. Dellith, M. Rothhardt, M. B. Marques, D. Donlagic, H. Bartelt, and O. Frazao, "Focused ion beam post-processing of optical fiber Fabry-Perot cavities for sensing applications," *Opt Express* 22, 13102-13108 (2014).
26. M. M. Bubnov, M. E. Dianov, O. N. Ogorova, S. L. Semjonov, A. N. Guryanov, V. F. Khopin, and E. M. DeLiso, "Fabrication and investigation of single-mode highly phosphorus-doped fibers for Raman lasers," in *Proc. SPIE*, (2000), pp. 12-22.
27. T. M. Benson, S. V. Boriskina, P. Sewell, A. Vukovic, S. C. Greedy, and A. I. Nosich, "Micro-optical resonators for microlasers and integrated optoelectronics - Recent advances and future challenges," *Nato Sci Ser II-Math* 216, 39-70 (2006).
28. D. Donlagic, "All-fiber micromachined microcell," *Opt Lett* 36, 3148-3150 (2011).
29. S. Pevec and D. Donlagic, "High resolution, all-fiber, micro-machined sensor for simultaneous measurement of refractive index and temperature," *Opt Express* 22, 16241-16253 (2014).
30. "World-class fiber optic sensing solutions", retrieved www.fiso.com.
31. E. Cibula, S. Pevec, B. Lenardic, E. Pinet, and D. Donlagic, "Miniature all-glass robust pressure sensor," *Opt Express* 17, 5098-5106 (2009).
32. S. Pevec and D. Donlagic, "Miniature fiber-optic sensor for simultaneous measurement of pressure and refractive index," *Opt Lett* 39, 6221-6224 (2014).
33. S. Pevec and D. Donlagic, "Nanowire-based refractive index sensor on the tip of an optical fiber," *Appl Phys Lett* 102(2013).
34. S. Pevec and D. Donlagic, "All-fiber, long-active-length Fabry-Perot strain sensor," *Opt Express* 19, 15641-15651 (2011).
35. S. Pevec and D. Donlagic, "Miniature all-silica fiber-optic sensor for simultaneous measurement of relative humidity and temperature," *Opt Lett* 40, 5646-5649 (2015).

Arrived: 31. 08. 2016

Accepted: 22. 09. 2016

Design and analysis of differential passive circuits for I/Q generation in 60 GHz integrated circuits

Ivan M. Milosavljević^{1,2}, Dušan P. Krčum^{1,2}, Lazar V. Saranovac¹

¹*Department of Electronics, School of Electrical Engineering, University of Belgrade, Belgrade, Serbia*

²*NovelIC Microsystems, Belgrade, Serbia*

Abstract: I/Q generation circuit design is of great importance within the design of modern radars integrated on chip, as well as in high-speed communication circuits operating at millimeter wave frequencies. Due to increased robustness on process variations and noise, differential signaling and differential I/Q generators are of particular interest. Several passive topologies suitable for usage in the commercially available 130 nm SiGe BiCMOS process are presented and evaluated. These topologies are: branch-line coupler (BLC), broadside coupler (BSC), poly-phase filter (PPF) and quadrature all-pass filter (QAF). The first three topologies are implemented and the obtained results are compared to results published previously. The designed PPF has a total phase error of $\pm 2.5^\circ$ over a 40 GHz bandwidth and this is the most desired solution if the total available area is a limiting factor. Transmission lines required for the design of BLC and BSC are small enough, making such structures easy to implement using today's mainstream technologies. BLC is a reliable and widely used solution for I/Q generation at almost any microwave frequency. Designed BLC has a phase error of $\pm 1.7^\circ$ over a 7 GHz bandwidth. BSC has proved to be the best solution for I/Q generation in the 60 GHz band. The designed solution has a smaller area than BLC, a phase error of only $\pm 5^\circ$ over a 40 GHz bandwidth and $\pm 1^\circ$ over a 7 GHz bandwidth.

Keywords: millimeter-wave passive circuits; I/Q generation; 90° hybrid coupler; branch-line coupler; broadside coupler; poly-phase filter; quadrature all-pass filter

Načrtovanje in analiza diferencialnih pasivnih vezij za generiranje I/Q v 60 GHz integriranih vezjih

Izveček: Načrtovanje I/Q generiranih vezij ima velik pomen v modernih integriranih radarjih, kakor tudi pri komunikacijskih vezjih visokih hitrostih v območju milimetrskih valovnih dolžin. Zaradi proizvodne robustnosti in šuma, so diferencialni I/Q generatorji zelo pomembni. Predstavljene so številne pasivne topologije uporabne v komercialni 130 nm SiGe BiCMOS tehnologiji, in sicer: linijski sklopnik (BLC), hibridni sklopnik (BSC), polifazni filter (PPF) in kvadraturni polnopenepustni filter (QAF). Prve tri topologije so uporabljene in primerjane s prej objavljenimi rezultati. Načrtovan PPF ima skupno fazno napako $\pm 2.5^\circ$ pri 40 GHz pasovni širini in je najugodnejša rešitev, če imamo omejitve s prostorom. Prenosne linije, ki so potrebne za BLC in BSC so dovolj majne, da lahko ti topologiji uporabimo z uporabo današnjih tehnologij. BLC je zanesljiva in najbolj uporabljena rešitev v mikrovalovnih frekvencah. Fazna napaka načrtanega BLC je $\pm 1.7^\circ$ v 7 GHz pasovni širini. Najugodnejša rešitev v 60 GHz pasu je BSC. Potrebuje manjšo površino in ima fazno napako $\pm 5^\circ$ v 40 GHz pasu in $\pm 1^\circ$ v 7 GHz pasu.

Ključne besede: milimeterska valovna pasivna vezja; I/Q generacija; 90° hibridni sklopnik; vejni sklopnik; polifazni filter; kvadraturni polnopenepustni filter

* Corresponding Author's e-mail: ivan.milosavljevic@novelic.com

1 Introduction

Today's millimeter-wave integrated circuits are primarily intended for communication and radar sensing applications. Advancements in silicon-based technology processes allowed the very high scale integration, making complete millimeter-wave systems integrated into a single chip. In these complex systems, usually there is a need for the generation of in-phase (I) and quadrature (Q) signals [1-5]. As an example, for blocks such as I/Q modulators [6], frequency multipliers [7], or vector-modulators [8-10], it is mandatory to have supporting circuits that provide the desired 90° phase shift between the input signals, in cases when quadrature signals are not provided by the local oscillator (LO). Direct I/Q signal generation from the LO requires the design of a quadrature voltage controlled oscillator (QVCO). Although the design of a conventional parallel-coupled QVCO at millimeter-wave frequencies is feasible and reported in [11], the approach suffers from very high phase noise, and therefore its usage is limited. There are other QVCO state-of-the-art techniques based on injection- [12] and magnetic-coupling [13] that improve phase-noise, but their complexity and reliability issues rise with frequency. At microwave frequencies 90° phase generation can be provided by active quadrature dividers [14]. The use of dividers requires the VCO operating at twice the nominal frequency, therefore at higher millimeter-wave frequencies this is not a suitable topology. Another approach is using injection-locked frequency multipliers [15], that also suffer from similar problems as the approach with QVCO. Furthermore, using active circuits for I/Q generation requires current-hungry and more sophisticated designs at millimeter-wave frequencies. In opposite to active circuits, passive circuits do not consume power. However, they introduce some losses that often need to be compensated, and the total loss per branch cannot be smaller than the theoretical minimum of 3 dB. Besides consumption, the key advantages of passive circuits are design simplicity and reliability. Consequently, a natural choice for I/Q signal generation at millimeter-wave frequencies is a passive circuit.

There are various ways of generating quadrature signals with passive circuits based on quarter-wave ($\lambda/4$) coupled and transmission line millimeter-wave structures. The limiting factor for quarter-wave structures, also known in literature as 90° hybrid couplers, is chip area which is directly related to signal wavelength. This is the reason why these structures are much more interesting nowadays when the majority of high-speed communication systems operating frequencies are shifted to the millimeter-wave area. Passive quarter-wave structures for microwave frequencies have been

investigated at various substrates. The investigations are mainly focused on miniaturization of quarter-wave coupled structures, as reported in [16, 17]. Most of them only deal with single-ended circuits, not suitable for integration in high-performance integrated circuits. Therefore this paper is focused only on topologies that have differential counterparts, in order to minimize sensitivity to noise and undesired couplings. On the other hand, passive circuits for quadrature generation are also designed from lumped components. The main representatives are RC and RLC based circuits and a vast number of papers comprised of circuits at millimeter-wave frequencies have been reported [18-20].

The article is organized as follows: Section 2 shows theoretical basics of different passive circuits for I/Q generation. Implementation of circuits and simulation results obtained with electromagnetic (EM) solvers are shown in Section 3, followed by conclusions in Section 4.

2 Passive circuits for I/Q generation

The main parameters of passive circuits for I/Q generation are reflection coefficients, insertion loss, coupling, directivity, bandwidth, phase imbalance, amplitude imbalance, isolation between output ports and chip area. The priority of parameters is determined by specific application. Typically in millimeter-wave integrated circuits, the highest priority parameters are phase imbalance, insertion loss and chip area.

Based on physical phenomena of quadrature generation, passive circuits are divided in two main categories: I/Q generators based on distributed structures (transmission lines) and I/Q generators based on lumped components.

2.1 Distributed

Transmission line-based passive circuits provide 90° phase shift using quarter-wave segments of transmission lines. The most basic representative is the one with $\lambda/4$ transmission line inserted in the quadrature signal path. This approach requires a power divider for splitting the input signal in two signals of equal power. If a Wilkinson power divider [21] is used, significant chip area is required. In Figure 1, differential structures based on 90° transmission lines are shown. The input differential signal is LO, and the outputs are differential in-phase (I) and quadrature (Q) signals. Conventional approach shown in Figure 1 (a) suffers from narrowband operation, which can be improved using the Schiffman technique shown in Figure 1 (b) [22]. With this technique, performance is improved at the

expense of chip area. Both implementations are impractical in millimeter-wave integrated circuits due to increased area and attenuation.

Alternatively, distributed structures based on concentrated coupling and coupled transmission lines are widely used in millimeter-wave integrated circuits.

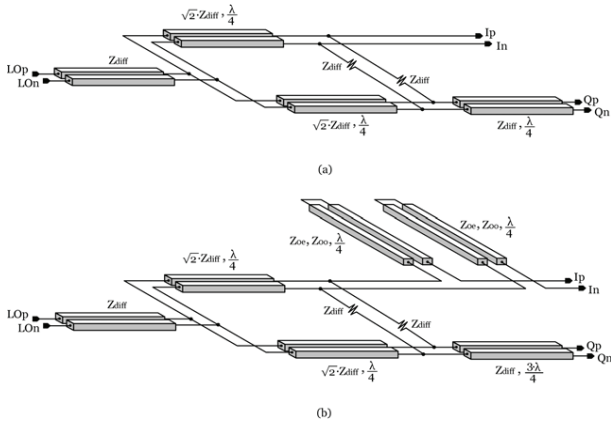


Figure 1: (a) 90° transmission line based power divider, (b) Schiffman 90° power divider.

2.1.1 Concentrated coupling

Branch-line coupler (BLC) is a representative of transmission lines concentrated coupling. Conventional BLC hybrid is shown in Figure 2 (a). Since it occupies considerable chip area, reduction of transmission lines length is proposed in [16], by inserting shunt capacitance at the end of the transmission lines. This is shown in Figure 2 (b).

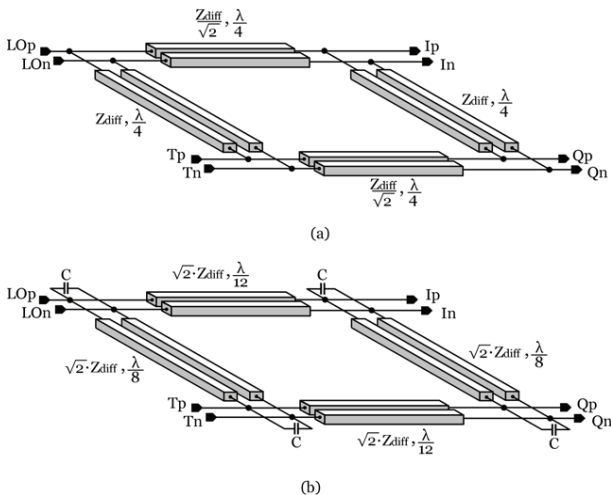


Figure 2: (a) Conventional branch-line coupler, (b) Reduced size branch-line coupler.

The relationships between electrical lengths of branch-line θ_1 and through-line θ_2 , the differential characteristic impedance Z , the nominal differential impedance Z_{diff} and shunt capacitance C in reduced-size BLC hybrid are given as

$$\theta_1 = \arcsin\left(\frac{Z_{diff}}{Z}\right), \tag{1}$$

$$\theta_2 = \arcsin\left(\frac{Z_{diff}}{\sqrt{2}Z}\right), \tag{2}$$

$$\omega CZ_{diff} = \sqrt{1 - \left(\frac{Z_{diff}}{Z}\right)^2} + \sqrt{2 - \left(\frac{Z_{diff}}{Z}\right)^2}. \tag{3}$$

In Figure 2 (b) it is given commonly used case when $Z_{diff}/Z=1/\sqrt{2}$, $\theta_1 = 30^\circ$ and $\theta_2 = 45^\circ$. These values are very suited for practical implementations. Additionally, a technique of meandering is implemented whenever applicable to reduce total chip area.

2.1.2 Coupled line

In microwave theory, I/Q generators based on coupled lines are known as directional couplers. Directional couplers are easily constructed from two $\lambda/4$ coupled transmission lines. The coupling effect is achieved by broadside coupling or edge-side coupling, as shown in Figure 3. The coupling ratio between two broadside coupled metal layers is given by

$$k = \frac{Z_{0e} - Z_{0o}}{Z_{0e} + Z_{0o}} = \sqrt{\epsilon_r} \times k_{air}, \tag{4}$$

Where Z_{0e} and Z_{0o} are even- and odd-mode impedances of the coupled lines, ϵ_r is the relative permittivity of the substrate, and k_{air} is the coupling factor of the two lines in air.

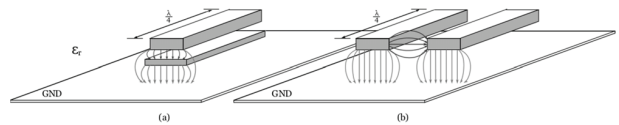


Figure 3: (a) Broadside coupling, (b) Edge-side coupling.

In integrated realizations, the broadside coupler (BSC) is suitable for implementation, and its vertical approach saves chip area. An important issue is that the distributed capacitance from the broadside coupled lines to the ground is asymmetric. Therefore, the width of transmission lines must be asymmetric to minimize asymmetry and optimize bandwidth, as shown in Figure 3 (a).

Alternatively, edge-side coupled structures shown in Figure 3 (b) can be used. They are very simple to design, but suffer from several issues. Due to its inhomogeneous dielectric nature, modal velocities of even-

and odd-modes are different. This difference leads to poor isolation and, consequently, worse directivity of the coupler. In order to overcome this problem, modal velocities should be equalized. Within practical solutions for equalization, the most suitable one for integrated circuit (IC) design is the placement of capacitors between input and output ports. However, even after applying this technique, overall performance of edge-side coupler remains mediocre. The edge-side coupler also suffers from reliability issues due to fabrication and tolerance problems.

As a solution, multiple transmission lines are interdigitated in edge-side couplers. This structure is known as a Lange coupler [23], and the key design parameter is the voltage coupling coefficient c . Improved coupling helps in relaxing fabrication and tolerance problems. Millimeter-wave designs of single-ended unfolded Lange coupler are reported in [8, 24], etc. Differential Lange coupler requires two single-ended Lange structures that significantly increase the area and complexity of the circuit, therefore they are rarely used.

2.2 Lumped components based

Passive circuits for quadrature signal generation can be realized using basic circuit elements such as resistors, capacitors and inductors. Mentioned elements can easily be implemented in currently available silicon-based processes. This approach in generation of quadrature signals leads to simple, inexpensive and very compact design. However, this design has large losses and a significant central frequency shift which is temperature and process dependent. Circuits for I/Q generation that use lumped elements are unable to handle larger power levels. In practical designs, two main circuit topologies are used: poly-phase filter (PPF) and quadrature all-pass filter (QAF).

2.2.1 Poly-phase filters

PPF quadrature generation is based on phase shaping using combination of low-pass and high-pass RC filters. Low-pass (LPF) and high-pass filter (HPF) transfer functions are given by

$$H_{LPF}(j\omega) = \frac{1}{1 + j\omega RC}, \quad (5)$$

$$H_{HPF}(j\omega) = \frac{j\omega RC}{1 + j\omega RC}. \quad (6)$$

Corresponding arguments are:

$$\theta_{LPF} = -\arctg(\omega RC), \quad (7)$$

$$\theta_{HPF} = \frac{\pi}{2} - \arctg(\omega RC). \quad (8)$$

If the values of the components in LPF and HPF are chosen as $RC = \frac{1}{\omega_0}$, where ω_0 is radial frequency of an input signal, phase shift through a LPF is -45° and through HPF is $+45^\circ$, while attenuation is equal in both paths.

The first order PPF achieves a narrowband quadrature generation and has a wide phase variation over process and temperature. More robust design can be obtained using higher order PPF. Second order PPFs are widely used, as shown in Figure 4. In order to reduce influence of the process variations, component values of each PPF stage are chosen for a different central frequency:

$$R_1 C_1 = \frac{1}{\omega_1}, \quad (9)$$

$$R_2 C_2 = \frac{1}{\omega_2}. \quad (10)$$

Relationship between the input radial frequency and poles of PPF is given by

$$\omega_1 \omega_2 = \omega_0^2, \quad (11)$$

where $\omega_1 < \omega_0 < \omega_2$.

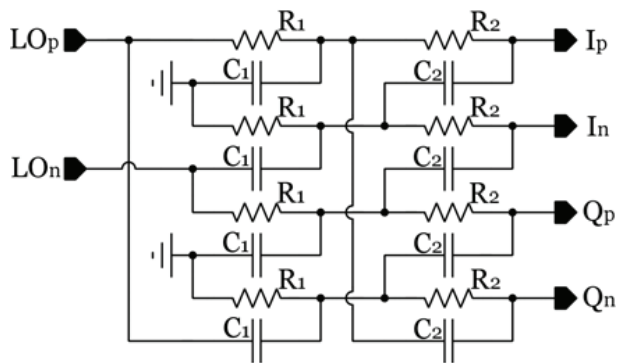


Figure 4: Second order PPF schematic.

2.2.2 Quadrature all-pass filter

QAF is used for phase shaping of quadrature output signals. In Figure 5, is shown the schematic of a fully differential QAF.

Theory of operation is similar to PPF. Namely, QAF also uses combination of LPF and HPF for adequate phase shift between the output signals. Transfer functions between LO input and I and Q outputs are given in equations (12) and (13):

$$H_I(j\omega) = \frac{R + j\omega L}{R + j\left(\omega L - \frac{1}{\omega C}\right)}, \quad (12)$$

$$H_Q(j\omega) = \frac{R + \frac{1}{j\omega C}}{R + j\left(\omega L - \frac{1}{\omega C}\right)}. \quad (13)$$

Figure 5: LC based QAF schematic.

Phase difference between QAF outputs can be derived from the previous transfer functions, and after simplification the final expression for the QAF phase difference is:

$$\theta_{QAF} = \arctg \left(\frac{\omega^2 LC + 1}{\omega \left(RC - \frac{L}{R} \right)} \right). \quad (14)$$

In order to make the phase difference between I and Q signals equal to 90°, the resistance value should be

$$R = \sqrt{\frac{L}{C}}, \quad (15)$$

and for equal attenuation in both paths

$$LC = \left(\frac{1}{\omega_0} \right)^2. \quad (16)$$

3 Implementation and simulation results

In this section, different passive I/Q generators are implemented using a commercially available 130 nm SiGe BiCMOS technology with seven metal layers shown in Figure 6.

In all implementations solid metal 1 is used as circuit ground. All passive circuits are simulated in 2.5D planar EM solver based on method of moments (MoM), and verified in 3D full-wave solver based on finite element method (FEM). The comparison between simulation results is given for all designed circuits. The results obtained with MoM based simulator are shown as dashed lines, and the results obtained with FEM based simulator as solid lines. Impact of the mismatch and process variations of resistors and capacitors on phase and

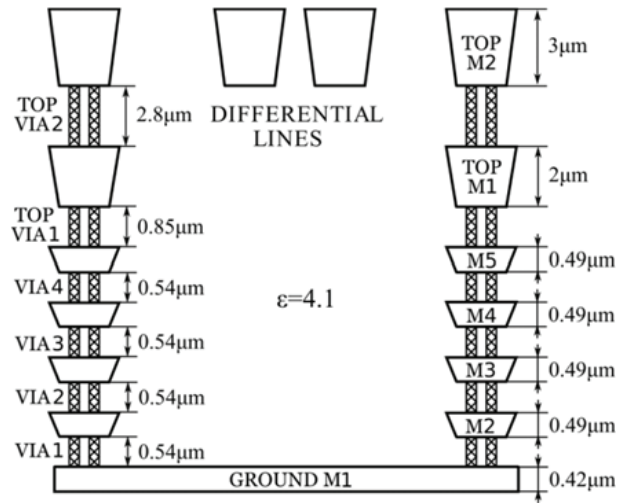


Figure 6: Technology metal stack.

amplitude imbalance is simulated for all circuits using Monte Carlo simulations. Influence of the output load mismatch is also analyzed. Output impedances of both I and Q loads are varied in range 80% - 120% of nominal 100 Ω differential impedance. Effect of the mismatch and process variations and load mismatch is analyzed on single frequency of 60 GHz and characterized using ±3σ (standard deviation).

3.1 Branch-line coupler

Implementation of differential reduced-size BLC is presented in this subsection. Transmission lines are implemented in 3 μm thick top metal 2. Differential impedance of branch-line and through-line is 141.4 Ω, which corresponds to lines of width 3 μm and spacing 17 μm. Transformation to a differential impedance of 100 Ω at input and output ports is achieved by reducing line spacing to 7 μm and retaining same widths. According to equation (3), 43 fF differential capacitor value is obtained. Metal-insulator-metal (MIM) capacitors are used. In this technology, the bottom electrode of the MIM capacitor is connected to metal 5 and the

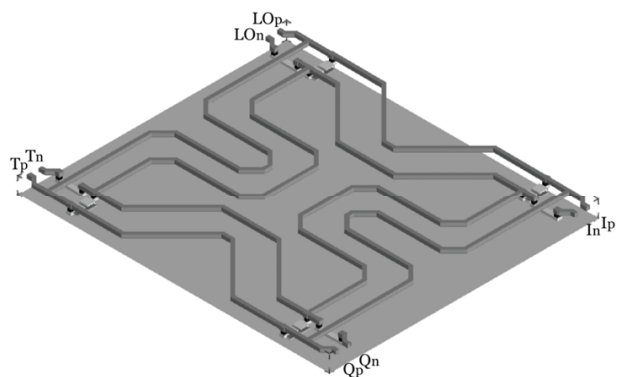


Figure 7: 3D preview of the differential branch-line coupler.

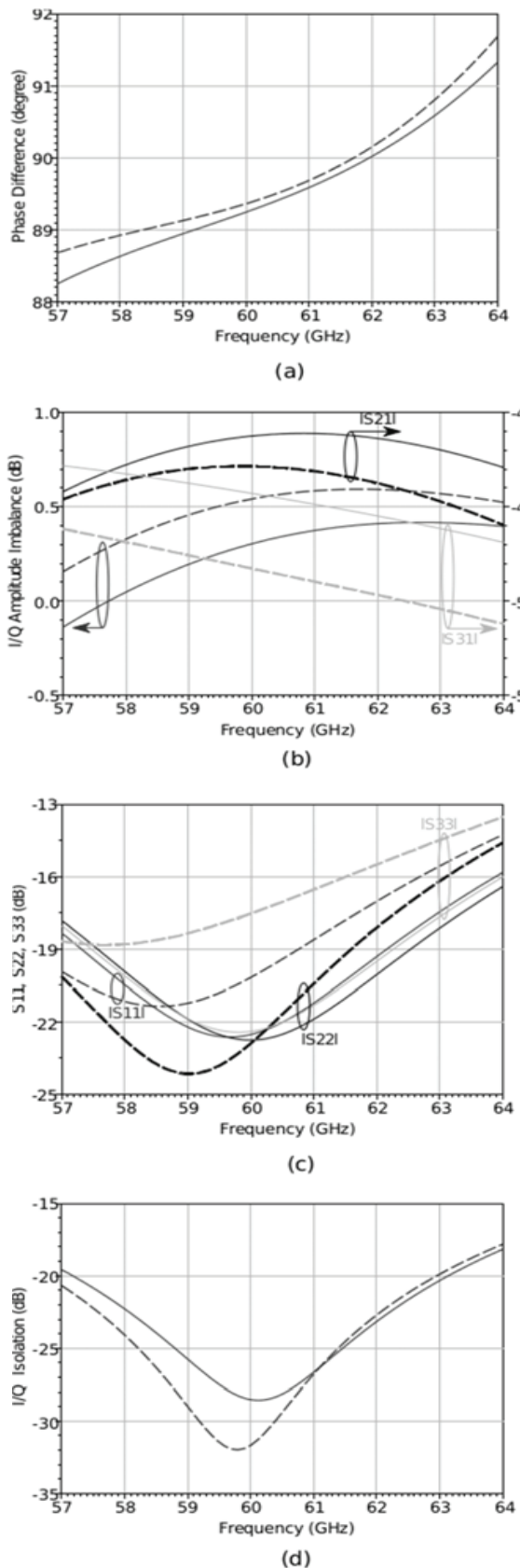


Figure 8: The performance of differential branch-line coupler: (a) phase difference, (b) insertion loss, (c) reflection coefficient, (d) isolation.

top electrode to top metal 1. Thus, two serial capacitors with twice the capacitance are used instead of a single differential capacitor. Capacitors are made in such a way to fit between differential lines and are connected in metal 5. 3D preview of the reduced-size BLC is shown in Figure 7. A meandering technique is used to reduce the overall BLC area, which is $267 \mu\text{m} \times 230 \mu\text{m}$.

The termination port is connected to a 100Ω resistor and the performance of the 60 GHz BLC obtained by MoM and FEM based simulators are shown in Figure 8.

The BLC exhibits excellent performance in a 7 GHz bandwidth. Phase imbalance of the BLC is lower than 1.7° , and amplitude imbalance is lower than 0.4 dB. Reflection coefficients at input and outputs are lower than -14 dB. Performing process and mismatch Monte Carlo simulations gave us the insight in circuit's behavior under mentioned conditions. It is noticed that phase and amplitude imbalance does not vary more than 2.42° and 0.14 dB in the case of process and mismatch variations of the termination resistor and MIM capacitors. Major contributor on phase and amplitude imbalance deviation is the process variation of MIM capacitors and this should be taken into account in design process of reduced-size BLC. I/Q load mismatch effect on the phase imbalance is lower than 0.76° , while the amplitude imbalance is negligible.

3.2 Broadside coupler

Differential input and output signals of the BSC are implemented in top metal 2 layer. Transmission lines are optimized to a differential impedance of 100Ω . The width of lines is $3.5 \mu\text{m}$ and spacing is $4.5 \mu\text{m}$. Coupled $\lambda/4$ lines are implemented in top metal 1 and metal 5 to achieve high coupling efficiency. Inter-layer distance is $0.85 \mu\text{m}$. It requires the coupling coefficient k of $1/\sqrt{2}$, and according to equation (4) values for even- and odd-mode impedances are approximately 241.5Ω and 41.4Ω . The widths of coupled lines are calculated from the EM simulation and top metal width of $5 \mu\text{m}$ and bottom metal width of $8 \mu\text{m}$ are obtained. In Figure 9, the geometry of 60 GHz differential BSC is shown. Aggressive meandering of the coupled lines is performed to minimize chip area. The BSC dimensions are $190 \mu\text{m} \times 170 \mu\text{m}$.

Termination impedances T1 and T2 are chosen to be asymmetric in order to achieve very low phase mismatch. In this way the amplitude difference is consciously sacrificed. Termination impedance T1 is 20Ω , and termination impedance T2 is 50Ω . The performance of the 60 GHz BSC obtained by MoM and FEM simulators are shown in Figure 10.

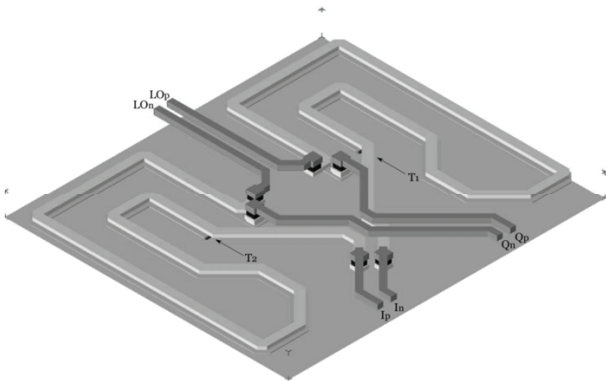


Figure 9: 3D preview of the differential broadside coupler.

In the 40 GHz bandwidth, phase imbalance of the BSC is lower than 5°, and amplitude imbalance is lower than 2 dB. Reflection coefficients at inputs and outputs are lower than -10 dB, thus an excellent matching is achieved without any additional matching structures. Impact of the mismatch and process variations of termination resistors on phase and amplitude imbalance is lower than 1.1° and 0.18 dB. Also, the load mismatch effect on the phase and amplitude imbalance is lower than 1.5° and 0.25 dB.

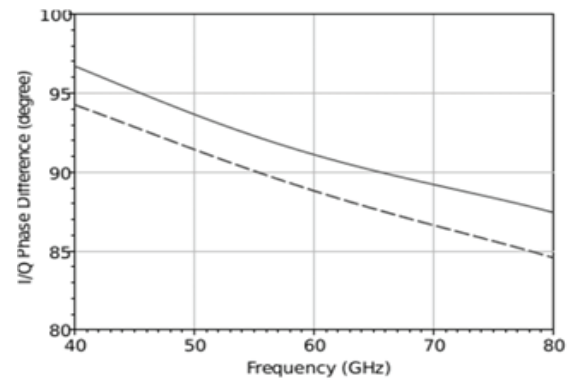
3.3 Poly-phase filter

Two stage PPF is designed for 60 GHz band as follows. Central operating frequency f_1 for the first stage is 62.25 GHz, and for the second stage f_2 is 59.25 GHz. Capacitance is chosen to be the same in both stages and equal to 39 fF. This is quite small value for the given technology, thus the series connection of four capacitors with capacitance of 156 fF is used. The resistance of the first stage is then $R_1 = 64.75\Omega$, and the resistance of the second stage is $R_2 = 68\Omega$. Dimensions of the designed PPF are 130 μm x 80 μm , and 3D preview is shown in Figure 11.

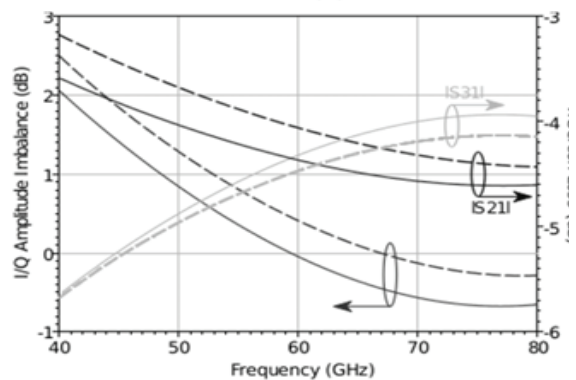
The performance of the 60 GHz PPF are shown in Figure 12. The phase imbalance is less than 2.5° at a 40 GHz range, but the PPF has significantly poorer matching.

Impact of the mismatch and process variations of resistors and MIM capacitors on the phase and amplitude imbalance is lower than 0.6° and 0.1 dB making PPF very robust to mismatch and process variations. Load mismatch effect on the phase and amplitude imbalance is lower than 3.8° and 1 dB, which shows that the PPF is very sensitivity on output load mismatch.

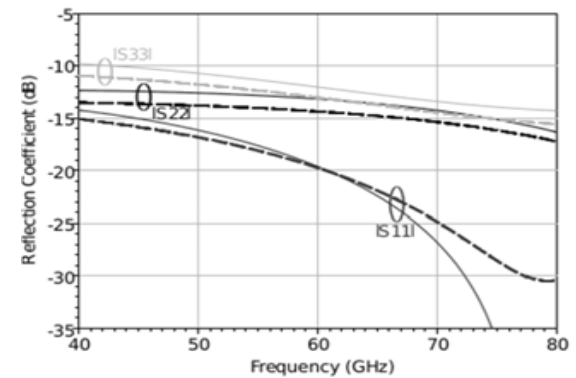
The performance summary is shown in Table 1.



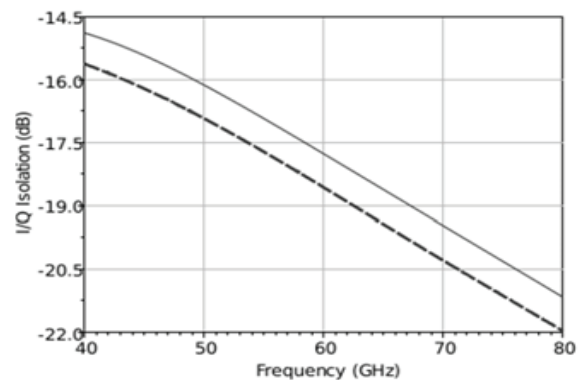
(a)



(b)



(c)



(d)

Figure 10: The performance of differential broadside coupler: (a) phase difference, (b) insertion loss, (c) reflection coefficient, (d) isolation.

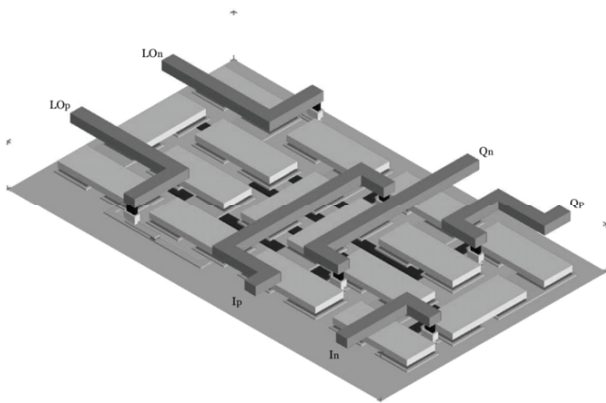


Figure 11: 3D preview of the 60 GHz poly-phase filter.

4 Conclusion

An overview of I/Q generation circuits for the 60 GHz band is presented in this paper. The three most suitable and most common topologies are chosen to be designed in a modern BiCMOS process.

In comparison to other I/Q generation circuits, BSC exhibits the best performance. The main advantages of this design over other references is a small area and small phase error over a 40 GHz frequency range. Insertion loss is comparable to theoretical values, thus it does not require an additional amplification stage. In a 7 GHz bandwidth around 60 GHz it presents supreme performance. All of these parameters highlight BSC as the first choice for an I/Q generation block in modern CMOS designs, in millimeter-wave integrated circuits. A possible drawback of this design is the usage of a specific metal stack. Depending on the vertical spacing between metal layers used for the implementation of the coupler, desired even- and odd-mode impedances may not be achievable.

On the other hand, BLC is implemented in the same metal layer and does not have the technology related drawbacks. Small areas can be obtained using meandering and capacitive termination of $\lambda/4$ lines. However, using capacitive termination of $\lambda/4$ lines leads to increased phase and amplitude deviation related with process and mismatch variations of used capacitors. Phase error in a 7 GHz bandwidth around 60 GHz is noticeably low and all ports are well matched. Insertion loss and output isolation are equally good as for BSC. However, BLC occupies a larger area than BSC.

A poly-phase filter is used as the third I/Q generation circuit for applications in the 60 GHz band. This solution can be used in situations where area is critical. However, PPF has huge insertion losses and has large sensitivity on the output load impedance mismatch. These

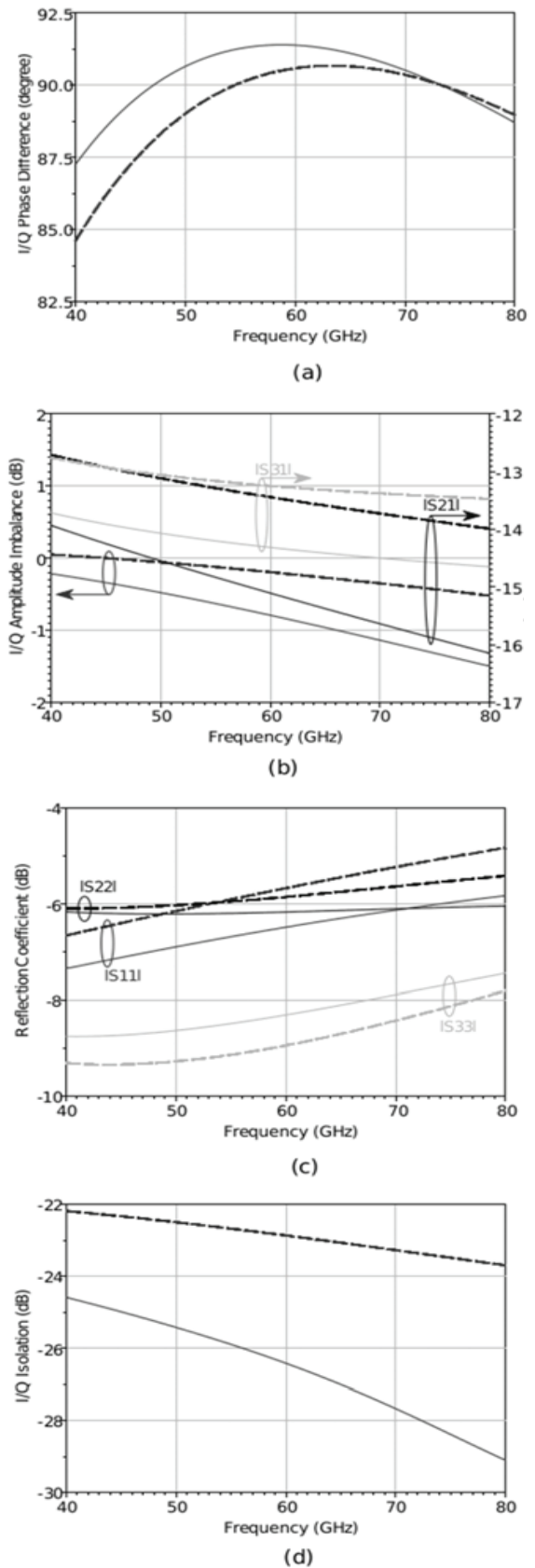


Figure 12: The performance of the 60 GHz poly-phase filter: (a) phase difference, (b) insertion loss, (c) reflection coefficient, (d) isolation.

Table 1: Overview of 60 GHz passive circuits for I/Q generation.

Reference	Type	Pol. ^a	BW [GHz]	$ S_{ii} ^b$ [dB]	$ S_{ij} ^c$ [dB]	$ S_{32} $ [dB]	PI [°]	AI [dB]	Area [μm^2]
[1]	BLC	S.e.	7	-11	-6	-14	± 3.6	± 0.75	370x270
[24]	Lange	S.e.	60	-16	-4.5	-14	± 9.6	± 2.25	300x160
[24]	Lange	S.e.	60	-13	-4.5	-11	± 11.5	± 1.75	160x120
[5]	BSC	S.e.	30	-15	-4.5	N/A	± 3	± 0.75	280x200
[6]	BSC	Diff.	40	-13	-5	N/A	± 5.3	± 0.6	350x175
[25]	BLC	Diff.	7	N/A	N/A	N/A	± 4	± 0.5	400x550
[18]	PPF	Diff.	2	N/A	-10	N/A	± 2.1	N/A	210x200
This work ^d	BLC	Diff.	7	-14	-4.5	-17	± 1.7	± 0.4	267x230
This work ^d	BSC	Diff.	40	-10	-4.5	-15	± 5	± 1.5	190x170
This work ^d	PPF	Diff.	40	-5	-14	-22	± 2.5	± 0.75	130x80

^a polarity (Pol.): single ended (S.e.) or differential (Diff.)

^b input and output reflection coefficients: worst or any known values

^c insertion loss: average or any known value

^d simulation results

are the reasons why PPF requires additional output buffer amplifiers. PPF matching is also poor, and additional matching networks are mandatory. The greatest advantage of PPF is its robustness on process and mismatch variations, and a very small phase difference over a very wide frequency range.

5 References

1. C. Marcu, D. Chowdhury, C. Thakkar, J.D. Park, L.K.Kong, M. Tabesh, Y. Wang, B. Afshar, A. Gupta, A. Arbabian, S. Gambini, R. Zamani, E. Alon, and A.M. Niknejad, "A 90 nm CMOS Low-Power 60 GHz Transceiver With Integrated Baseband Circuitry," *IEEE Journal of Solid-State Circuits*, vol. 44, pp. 3434–3447, December 2009.
2. K.J. Koh, J.W. May, and G.M. Rebeiz, "A Millimeter-Wave (40–45 GHz) 16-Element Phased-Array Transmitter in 0.18- μm SiGe BiCMOS Technology," *IEEE Journal of Solid-State Circuits*, vol. 44, pp. 1498–1509, May 2009.
3. M. Tabesh, J. Chen, C. Marcu, L. Kong, S. Kang, A.M. Niknejad, and E. Alon, "A 65 nm CMOS 4-Element Sub-34 mW/Element 60 GHz Phased-Array Transceiver," *IEEE Journal of Solid-State Circuits*, vol. 46, pp. 3018–3032, December 2011.
4. Y. Zhao, E. Ojefors, K. Aufinger, T.F. Meister, and U.R. Pfeiffer, "A 160-GHz Subharmonic Transmitter and Receiver Chipset in an SiGe HBT Technology," *IEEE Transactions on Microwave Theory and Techniques*, vol. 60, pp. 3286–3299, October 2012.
5. I. Nasr, H. Knapp, K. Aufinger, R. Weigel, and D. Kissinger, "A 50–100-GHz Highly Integrated Octave-Bandwidth Transmitter and Receiver Chipset in 0.35- μm SiGe Technology," *IEEE Transactions on Microwave Theory and Techniques*, vol. 62, pp. 2118–2131, September 2014.
6. M. Abbasi, S. Carpenter, H. Zirath, and F. Dielacher, "A 80–95 GHz direct quadrature modulator in SiGe technology," in *2014 IEEE 14th Topical Meeting on Silicon Monolithic Integrated Circuits in RF Systems (SiRF)*, Newport Beach, 2014, pp. 56–58, IEEE.
7. W.L. Chan and J.R. Long, "A 56–65 GHz Injection-Locked Frequency Tripler With Quadrature Outputs in 90-nm CMOS," *IEEE Journal of Solid-State Circuits*, vol. 43, pp. 2739–2746, December 2008.
8. M.D. Tsai and A. Natarajan, "60GHz passive and active RF-path phase shifters in silicon," in *2009. RFIC 2009. IEEE Radio Frequency Integrated Circuits Symposium*, Boston, 2009, pp. 223–226, IEEE.
9. C. Zhou, L. Zhang, Y. Wang, Z. Yu, and H. Qian, "A 4-bit CMOS phase shifter for millimeter-wave phased arrays," *Analog Integrated Circuits and Signal Processing*, vol. 79, pp. 461–468, June 2014.
10. A. Vahdati, D. Parveg, M. Varonen, M. Karkkainen, D. Karaca, and K.A.I. Halonen, "W-band phase shifter in 28-nm CMOS," *Analog Integrated Circuits and Signal Processing*, vol. 84, pp. 399–408, September 2015.
11. K. Scheir, G. Vandersteen, Y. Rolain, and P. Wambacq, "A 57-to-66GHz quadrature PLL in 45nm digital CMOS," in *2009. ISSCC 2009. IEEE International Solid-State Circuits Conference - Digest of Technical Papers*, San Francisco, 2009, pp. 494–495, IEEE.
12. X. Yi, C.C. Boon, H. Liu, J.F. Lin, and W.M. Lim, "A 57.9-to-68.3 GHz 24.6 mW Frequency Synthesizer

- With In-Phase Injection-Coupled QVCO in 65 nm CMOS Technology," *IEEE Journal of Solid-State Circuits*, vol. 49, pp. 347–359, February 2014.
13. U. Decanis, A. Ghilioni, E. Monaco, A. Mazzanti, and F. Svelto, "A Low-Noise Quadrature VCO Based on Magnetically Coupled Resonators and a Wideband Frequency Divider at Millimeter Waves," *IEEE Journal of Solid-State Circuits*, vol. 46, pp. 2943–2955, December 2011.
 14. J.F. Buckwalter, A. Babakhani, A. Komijani, and A. Hajimiri, "An Integrated Subharmonic Coupled-Oscillator Scheme for a 60-GHz Phased-Array Transmitter," *IEEE Transactions on Microwave Theory and Techniques*, vol. 54, pp. 4271–4280, December 2006.
 15. A. Musa, R. Murakami, T. Sato, W. Chiavipas, K. Okada, and A. Matsuzawa, "A 58-63.6GHz quadrature PLL frequency synthesizer in 65nm CMOS," in 2010 IEEE Asian Solid State Circuits Conference (A-SSCC), Beijing, 2010, pp. 1–4, IEEE.
 16. T. Hirota, A. Minakawa, and M. Muraguchi, "Reduced Size Branch-Line and Rat-Race Hybrids for Unipolar MMIC's," *IEEE Transactions on Microwave Theory and Techniques*, vol. 38, no. 3, pp. 270–275, March 1990.
 17. J. Kim and J.G. Yook, "A Miniaturized 3 dB 90° Hybrid Coupler Using Coupled-Line Section With Spurious Rejection," *IEEE Microwave and Wireless Components Letters*, vol. 24, no. 11, pp. 766–768, November 2014.
 18. M.G.M. Notten and H. Veenstra, "60GHz Quadrature Signal Generation with a Single Phase VCO and Polyphase Filter in a 0.25µm SiGe BiCMOS technology," in *IEEE Bipolar/BiCMOS Circuits and Technology Meeting*, 2008, pp. 178–181, IEEE.
 19. I. Sarkas, M. Khanpour, A. Tomkins, P. Chevalier, P. Garcia, and S.P. Voinigescu, "W-band 65-nm CMOS and SiGe BiCMOS transmitter and receiver with lumped I-Q phase shifters," in 2009. RFIC 2009. *IEEE Radio Frequency Integrated Circuits Symposium*, Boston, 2009, pp. 441–444, IEEE.
 20. W. Shin and G.M. Rebeiz, "60 GHz active phase shifter using an optimized quadrature all-pass network in 45nm CMOS," in 2012 IEEE MTT-S International Microwave Symposium Digest (MTT), Canada, 2012, pp. 1–3, IEEE.
 21. E.J. Wilkinson, "An N-Way Hybrid Power Divider," *IRE Transactions on Microwave Theory and Techniques*, vol. 8, pp. 116–118, January 1960.
 22. B.M. Schiffman, "A New Class of Broad-Band Microwave 90-Degree Phase Shifters," *IRE Transactions on Microwave Theory and Techniques*, vol. 6, pp. 232–237, April 1958.
 23. J. Lange, "Interdigitated Strip-Line Quadrature Hybrid," in 1969 G-MTT International Microwave Symposium. 1969, pp. 10–13, IEEE.
 24. M.K. Chirala and B.A. Floyd, "Millimeter-Wave Lange and Ring-Hybrid Couplers in a Silicon Technology for E- Band Applications," in 2006. *IEEE MTT-S International Microwave Symposium Digest*. 2006, pp. 1547–1550, IEEE.
 25. B.A. Floyd, S.K. Reynolds, U.R. Pfeiffer, T. Zwick, T. Beukema, and B. Gaucher, "SiGe bipolar transceiver circuits operating at 60 GHz," *IEEE Journal of Solid- State Circuits*, vol. 40, pp. 156–167, January 2005.

Arrived: 17. 05. 2016

Accepted: 22. 08. 2 016

Dual-Mode Sinusoidal Quadrature Oscillator with Single CCCTA and Grounded Capacitors

Worapong Tangsrirat

Faculty of Engineering, King Mongkut's Institute of Technology Ladkrabang (KMITL), Ladkrabang, Bangkok, Thailand

Abstract: In this work, a sinusoidal quadrature oscillator which simultaneously generates voltage and current signal outputs is proposed. It contains only a single current-controlled conveyor transconductance amplifier (CCCTA) and two grounded capacitors. The proposed oscillator has the advantage features of resistorless structure realization, electronic frequency control, availability of two explicit voltage and current quadrature outputs, and low sensitivity figure. Moreover, the parasitic elements existing at the CCCTA terminals are taken into account. The performance of the proposed oscillator circuit was verified using PSPICE simulation with acceptable results.

Keywords: Current-Controlled Conveyor Transconductance Amplifier (CCCTA); Quadrature Oscillator; Resistorless circuits; Voltage-mode and current-mode circuits.

Dvojni sinusni kvadrantni oscillator z enosnim CCCTA in ozemljenimi kondenzatorji

Izveček: V članku je predstavljen je kvadrantni oscilator, ki vzporedno generira napetostni in tokovni signal. Vsebuje le en tokovno krmiljeno vezje transkonduktančnega ojačevalnika in dva ozemljena kondenzatorja. Predlagano vezje je brez uporov, vsebuje elektronski nadzor frekvence, omogoča dva ločena napetostna in tokovna izhoda in izkazuje nizko občutljivost. Upoštevani so parazitni elementi na CCCTA terminalih. Lastnosti oscilatorja so bile preverjene v PSPICE okolju.

Ključne besede: tokovno krmiljeno vezje transkonduktančnega ojačevalnika; brez uporovno vezje; napetostno in tokovno vezje

*Corresponding Author's e-mail: drworapong@gmail.com

1 Introduction

Sinusoidal quadrature oscillator or two-phase sinusoidal oscillator is a kind of the sinusoidal oscillators that provides explicit two signal outputs with 90° phase shift from the same structure. Accordingly, it performs an essential circuit block employed a wide range of applications in modern electronic and communication systems, control systems, and signal processing. There are many attempts recently in designing sinusoidal quadrature oscillators based on various types of modern active components [1-16]. However, many of them make use of at least two active components [1-12]. Only few circuits can provide both voltage and current quadrature signals from the same configuration [11-14]. These oscillator realizations contains an excessive number of

external passive components, i.e., at least four passive components. The recent current-mode quadrature oscillators based on single current differencing transconductance amplifier (CDTA) were introduced in [15-16]. The previous work in [15] employs only one CDTA and three passive components (including two virtually grounded passive components that are floating in the non-ideal sense). In [16], a compact single CDTA-based quadrature oscillator with three external passive components was reported. This circuit requires a floating capacitor, which is not favorable for further integration.

In 2008, the recently defined active circuit element, the so-called current-controlled conveyor transconductance amplifier (CCCTA), was introduced [17]. This de-

vice is a modified conception of the current conveyor transconductance amplifier (CCTA) [18], in which its parasitic resistance seen at the x-terminal (R_x) is variable electronically by adjusting an external biasing current. This property provides the advantage of realizing electronically controllable analog function circuits without external passive resistor requirement. Since its introduction, the CCCTA has numerous applications in a class of analog signal processing solutions and circuits [17], [19-21].

This paper presents a sinusoidal oscillator with variable oscillation frequency, able to provide explicitly quadrature voltage and current outputs from the same circuit configuration. The proposed quadrature oscillator employs only one CCCTA and two grounded capacitors. A detailed analysis shows that the oscillator circuit includes low active and passive sensitivities and has good frequency stability. Moreover, the effects of the CCCTA parasitic elements on the oscillator performance are also discussed. Simulation results with PSPICE using standard 0.35- μm BiCMOS process parameters are performed to verify the practical utility and validity of the realized circuit.

2 Principle of the CCCTA and its realization

Basically, the CCCTA can be realized through a cascade connection of second generation current-controlled conveyor (CCCII) and multi-output transconductance amplifier. Fig.1 shows the electrical symbol and equivalent circuit of the CCCTA. It is shown that this device consists of two input terminals (y and x) and two output terminals (z and $o\pm$). An ideal property of the CCCTA is described by the following matrix :

$$\begin{bmatrix} i_y \\ v_x \\ i_z \\ i_{o\pm} \end{bmatrix} = \begin{bmatrix} 0 & 0 & 0 & 0 \\ R_x & 1 & 0 & 0 \\ 1 & 0 & 0 & 0 \\ 0 & 0 & \pm g_m & 0 \end{bmatrix} \begin{bmatrix} i_x \\ v_y \\ v_z \\ v_{o\pm} \end{bmatrix} \quad (1)$$

where R_x represents the parasitic serial resistance at the x-terminal, and g_m denotes the effective small-signal transconductance gain of the CCCTA. As described in eq. (1), the x-terminal has a parasitic resistance R_x where its value usually depends on an external supplied current. The y-terminal exhibits the high-input impedance terminal, while the z and o-terminals are two types of high-output impedance terminals.

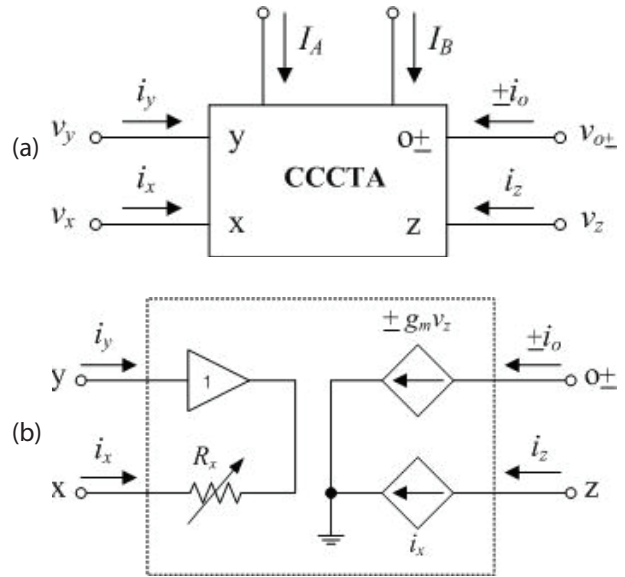


Figure 1: The CCCTA. (a) circuit symbol (b) equivalent circuit.

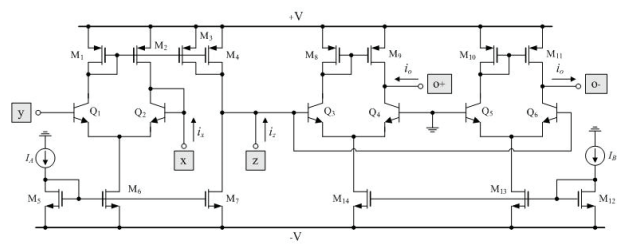


Figure 2: BiCMOS realization of the CCCTA.

One possible realization of the CCCTA in BiCMOS technology is shown in Fig.2 [22]. The circuit is mainly composed of second-generation current-controlled conveyor (Q_1 - Q_2 , M_1 - M_7) and dual-output transconductance amplifier (Q_3 - Q_6 , M_8 - M_{14}). Referring to Fig.2, the parasitic resistance R_x of the CCCTA has been derived as :

$$R_x \cong \frac{2V_T}{I_A} \quad (2)$$

where V_T is the thermal voltage, whose value is approximately 26 mV at 27°C. Note from eq.(2) that the value of R_x depends on the external DC bias current I_A . Assuming transistors Q_3 - Q_5 as well as M_8 - M_{11} are matched, the expression of g_m can be given by :

$$g_m = \frac{i_o}{v_z} = \frac{I_B}{2V_T} \quad (3)$$

Also note that the g_m -value is controllable electronically and linearly by changing the I_B -value.

3 Proposed dual-mode sinusoidal quadrature oscillator

Fig.3 shows a canonic sinusoidal oscillator that produces voltage and current quadrature outputs explicitly. The circuit constructs from only one CCCTA and two grounded capacitors without needing any external passive resistor. The state-space equations for this configuration is obtained as [23]-[24] :

$$\begin{bmatrix} \dot{v}_1 \\ \dot{v}_2 \end{bmatrix} = \begin{bmatrix} a_{11} & a_{12} \\ a_{21} & a_{22} \end{bmatrix} \begin{bmatrix} v_1 \\ v_2 \end{bmatrix} \quad (4)$$

where

$$a_{11} = a_{22} = 0, \quad a_{12} = -\frac{g_m}{C_1} \quad \text{and} \quad a_{21} = \frac{1}{R_x C_2} \quad (5)$$

From the above autonomous state-space expression, the characteristic equation of the circuit can be derived as :

$$s^2 - (a_{11} + a_{22})s + (a_{11}a_{22} - a_{12}a_{21}) = 0 \quad (6)$$

The condition of oscillation and the frequency of oscillation (ω_o) from eq.(6) are expressed, respectively, by

$$a_{11} + a_{22} = 0 \quad (7)$$

and

$$\omega_o = \sqrt{a_{11}a_{22} - a_{12}a_{21}} \quad (8)$$

This means that the circuit will oscillate with no oscillation condition at the oscillation frequency of

$$\omega_o = \sqrt{\frac{g_m}{R_x C_1 C_2}} \quad (9)$$

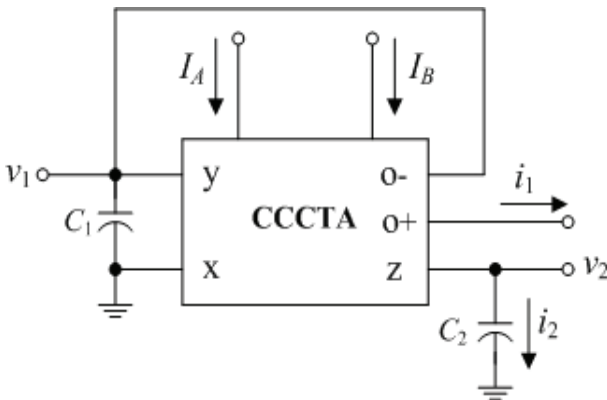


Figure 3: Proposed dual-mode sinusoidal quadrature oscillator.

It is obvious that the ω_o is electronically tunable through the transconductance gain (g_m) and/or parasitic resistance (R_x) of the CCCTA. Thus, the circuit can work as an electronically variable frequency quadrature oscillator.

Considering the proposed configuration of Fig. 3, the two output voltages marked v_1 and v_2 are related as :

$$v_1 = jk_1 v_2 \quad (10)$$

where $k_1 = \omega_o R_x C_2$. Eq.(10) represents a 90°-phase difference between both voltages, showing the quadrature property of the proposed oscillator. Furthermore, in case of $k_1 = 1$, the amplitudes of two quadrature outputs will also be equal. In addition, it is crucial to note that the quadrature output voltages v_1 and v_2 are not in low-impedance levels, hence external voltage buffers are necessary

Also from Fig.3, the relation for two output currents (i_1 and i_2) can be given by the following matrix equation.

$$\begin{bmatrix} i_1 \\ i_2 \end{bmatrix} = \begin{bmatrix} 0 & -\frac{g_m}{C_2} \\ \frac{1}{R_x C_1} & 0 \end{bmatrix} \begin{bmatrix} i_1 \\ i_2 \end{bmatrix} \quad (11)$$

It is seen that, in this case, the relationship between two quadrature current outputs i_1 and i_2 can be obtain as :

$$i_2 = jk_2 i_1 \quad (12)$$

where $k_2 = \omega_o C_2 / g_m$. Clearly, for $k_2 = 1$, two marked explicit quadrature current outputs have equal magnitude. It is also to be noted that the circuit provides the output current i_1 from the high-impedance terminal (terminal o+) but the output current i_2 can be obtained across C_2 . Therefore, for explicit dual-mode utilization, an external buffering unit would be required for sensing and taking out the current i_2 .

According to eq. (9), the relative sensitivity of ω_o with respect to active and passive components can be obtained as :

$$S_{g_m}^{\omega_o} = \frac{1}{2}, \quad S_{R_x}^{\omega_o} = -\frac{1}{2}, \quad S_{C_1}^{\omega_o} = -\frac{1}{2} \quad \text{and} \quad S_{C_2}^{\omega_o} = -\frac{1}{2} \quad (13)$$

All of which are lower than unity in magnitude.

4 Effects of the CCCTA Parasitic Elements

Fig.4 shows the practical model of the CCCTA. As it is seen, there are parasitic resistances and capacitances

from terminals y, z and o± to the ground ($R_y // C_y$, $R_z // C_z$ and $R_o // C_o$), and a serial parasitic resistance R_x at the x-terminal. It is further to be noted that the typical values of parasitic resistances R_y , R_z and R_o are in the range of several MΩ, whereas parasitic capacitances C_y , C_z and C_o are within a few fFs. Consider the CCCTA parasitic elements in the proposed oscillator of Fig.3. It is clear that the external grounded capacitors C_1 and C_2 are parallel connected at the terminals y and z, respectively. The effects of parasitic capacitances at corresponding terminals could be adsorbed, as they merge with external capacitance values. Hence, the total impedance at the y-terminal can be approximated to :

$$Z_y \cong \frac{(R_y // R_o)}{(R_y // R_o)C_1s + 1} \tag{14}$$

For the working frequencies,

$$\omega \gg \frac{1}{(R_y // R_o)C_1} = \omega_y \tag{15}$$

Z_y can be further reduced to the value of $1/C_1s$, which is practically not affected by $R_y // R_o$. In a similar way, at the z-terminal, the influence of R_z can also be alleviated for operation at frequencies:

$$\omega \gg \frac{1}{R_z C_2} = \omega_z \tag{16}$$

As a result, it can be realized from eqs. (15) and (16) that the frequency range at low frequencies should be selected as [25]:

$$\omega_L \gg 10 \times \max \{ \omega_y, \omega_z \} \tag{17}$$

Furthermore, it should be considered that there is a high-frequency limitation owing to the parasitic impedances ($R_o // C_o$) in parallel at the terminal o+. Thus, the extra pole introduced at the terminal o+ can be expressed as : $\omega_o \cong 1/(R_o C_o)$. To exhibit the ideal characteristic, the operating frequency range at high frequencies is found as :

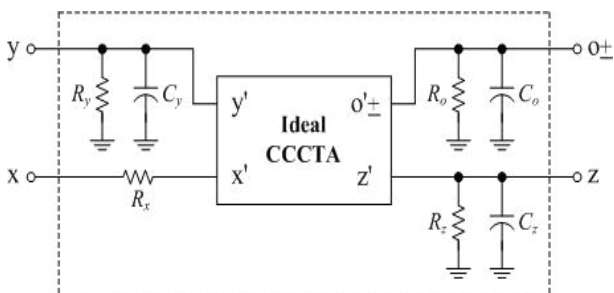


Figure 4: Practical model of the CCCTA including parasitic elements.

$$\omega_H \ll 0.1 \times \min \{ \omega_o \} \tag{18}$$

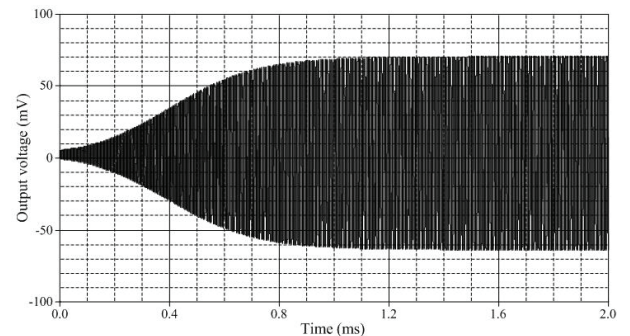
Finally, combining eqs.(17) and (19), the useful frequency range of the proposed oscillator can be defined as :

$$\omega_L \ll \omega \ll \omega_H \tag{19}$$

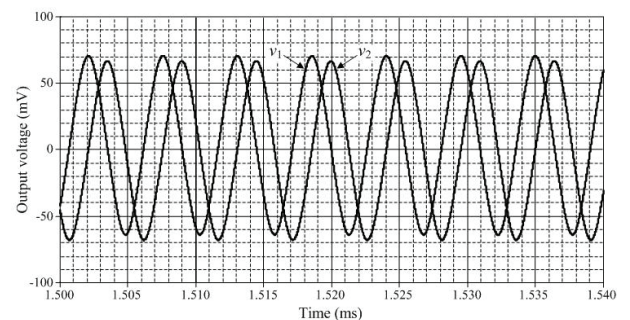
5 Computer Simulation and Performance Verification

The proposed dual-mode sinusoidal oscillator as depicted in Fig.3 was simulated using PSPICE program. In simulation purpose, the CCCTA structure given in Fig.2 was employed with standard 0.35-μm BiCMOS process parameters using supply voltages of +V = -V = 1 V. The aspect ratios (W/L in μm/μm) of the MOS transistors were set to 7/0.7 and 8.5/0.7 for all the NMOS and PMOS transistors respectively.

By choosing $C_1 = C_2 = 0.4$ nF, $I_A = I_B = 25$ μA, the proposed oscillator circuit of Fig.3 was designed to oscillate at $f_o = \omega_o / 2\pi \cong 191$ kHz. By performing time-domain analysis, the simulated transient waveforms for quadrature voltage and current outputs of the proposed oscillator are shown in Figs.5 and 6, respectively. As obtained from simulation results, the frequency of oscillation (f_o) was observed as 185 kHz. Fig.7 also shows the simulated fre-

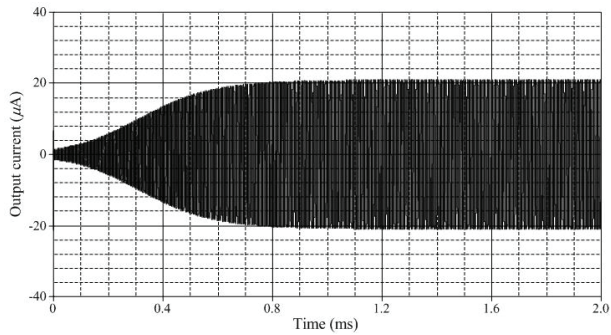


(a)

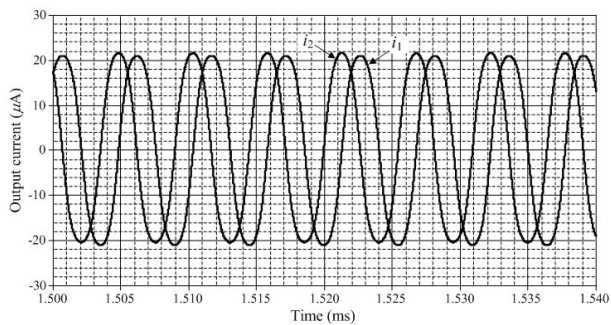


(b)

Figure 5: Simulated time-domain responses for v1 and v2. (a) initial-stage responses, (b) steady-state responses



(a)



(b)

Figure 6: Simulated time-domain responses for i_1 and i_2 . (a) initial-stage responses, (b) steady-state responses

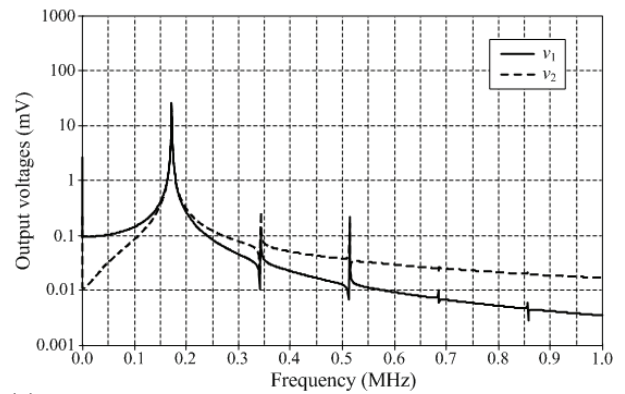
frequency spectrums of both voltage and current quadrature output waveforms, and the observed values of total harmonic distortion (THD) at all the outputs were less than 2.89%. To further demonstrate the electronic frequency controllability of the oscillator, the variation of f_o as a function of I_o ($= I_A = I_B$) is plotted in Fig.8.

6 Concluding Remarks

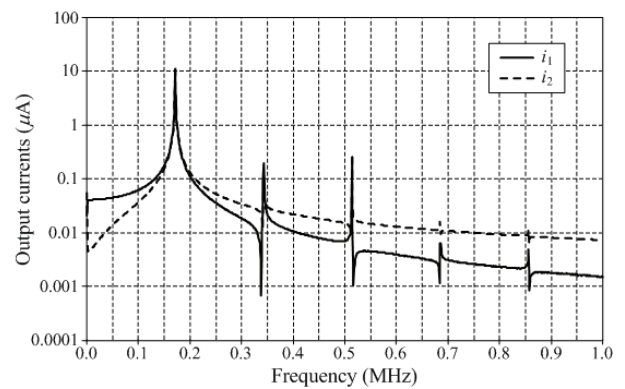
A generalized scheme to realize a resistorless dual-mode sinusoidal quadrature oscillator using one CCCTA and only two grounded capacitors is presented. The presented circuit is capable of simultaneously generating two quadrature voltage outputs and two quadrature current outputs. The frequency of oscillation can be made electronically tunable by external DC biasing currents of the CCCTA. Also, the circuit sensitivity study and parasitic element effects were discussed. The circuit performance is verified by PSPICE simulation results.

7 Acknowledgement

This work was supported by the Faculty of Engineering, King Mongkut's Institute of Technology Ladkrabang (KMUTL).



(a)



(b)

Figure 7: Simulated frequency spectrums of the proposed quadrature oscillator of Fig.3. (a) for v_1 and v_2 , (b) for i_1 and i_2

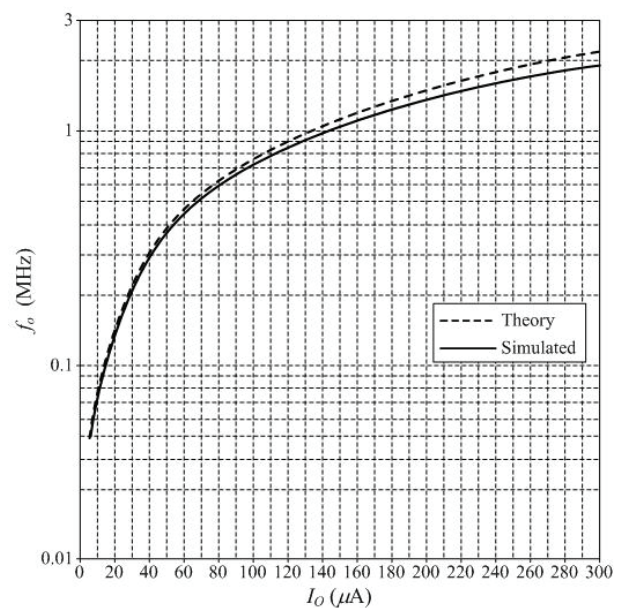


Figure 8: Electronic tuning of f_o with I_o .

8 References

1. A. U. Keskin, D. Biolek, "Current-mode quadrature oscillator using current differencing transconductance amplifiers (CDTA)", *IEE Proc. Circuits Devices Syst.*, vol.153, no.3, pp.214-218, 2006.
2. A. Lahiri, "New current-output quadrature oscillator using CDTA", *IEICE Electronics Express*, vol.6, no.3, pp.135-140, 2009.
3. W. Tangsrirat, W. Tanjaroen, "Current-mode sinusoidal quadrature oscillator with independent control of oscillation frequency and condition using CDAs", *Indian J. Pure Appl. Phys.*, vol.48, pp.363-366, 2010.
4. S. Maheshwariang, B. Chaturvedi, "High output impedance CMQOs using DVCCs and grounded components", *Int. J. Circ. Theor. Appl.*, vol.39, pp.427-435, 2011.
5. N. Minhaj, "Current conveyor-based voltage-mode two-phase and four-phase quadrature oscillator", *Int. J. Electron.*, vol.94, no.6-8, pp.663-669, 2007.
6. W. Tangsrirat, S. Pisitchalermping, "CDBA-based quadrature sinusoidal oscillator", *Frequenz*, vol.61, no.3-4, pp.102-104, 2007.
7. W. Tangsrirat, D. Prasertsom, T. Piyatat, W. Surakamponorn, "Single-resistance-controlled quadrature oscillator using current differencing buffered amplifiers", *Int. J. Electron.*, vol.95, no.11, pp.1119-1126, 2008.
8. W. Tangsrirat, T. Pukkalanun, W. Surakamponorn, "CDBA-based universal biquad filter and quadrature oscillator", *Active Passive Electron. Comp.*, vol.2008, Article ID 24717, 6 pages, doi : 10.1155/2008/247171, 2008.
9. S. Maheshwariang, J. Mohan, D. S. Chauhan, "High input impedance voltage-mode universal filter and quadrature oscillator", *J. Circuits Syst. Comput.*, vol.19, no.7, pp.1597-1607, 2010.
10. N. Herencsar, K. Vrba, J. Koton, A. Lahiri, "Realisations of single-resistance-controlled quadrature oscillator using a generalized current follower transconductance amplifier and a unity-gain voltage-follower", *Int. J. Electron.*, vol.97, no.8, pp.897-906, 2010.
11. S. Maheshwariang, I. A. Khan, "Novel single resistance controlled quadrature oscillator using two CDBAs", *J. Active Passive Electron. Devices*, vol.2, pp.137-142, 2007.
12. A. Lahiri, "Novel voltage/current-output quadrature oscillator using current differencing transconductance amplifier", *Analog Integr. Circ. Sig. Process.*, vol.61, no.2, pp.199-203, 2009.
13. A. Lahiri, "Explicit-current-output quadrature oscillator using second-generation current conveyor or transconductance amplifier", *Radioengineering*, vol.18, no.4, pp.522-526, 2009.
14. J. W. Horng, C. L. Hou, C. M. Chang, H. P. Chou, C. T. Lin, Y. H. Wen, "Quadrature oscillator with grounded capacitors and resistors using FDCClIs", *ETRI Journal*, vol.28, no.4, pp.486-494, 2006.
15. W. Jaikla, M. Siripruchyanun, J. Bajer, D. Biolek, "A simple current-mode quadrature oscillator using single CDTA", *Radioengineering*, vol.17, no.4, pp.33-40, 2008.
16. J. Jin, C. Wang, "Single CDTA-based current-mode quadrature oscillator", *Int. J. Electron. Commun. (AEU)*, vol.66, pp.933-936, 2012.
17. M. Siripruchyanun, W. Jaikla, "Current controlled current conveyor transconductance amplifier (CCCCTA): a building block for analog signal processing", *Electrical Engineering*, vol. 90, no. 6, pp. 443-453, 2008.
18. R. Prokop, V. Musil, "New modern circuit block CCTA and some its applications", *Proceedings of the Fourteenth International Scientific and Applied Science Conference-Electronics (ET-2005)*, Book 5, Sofia, pp.93-98, 2005.
19. R. Sotner, J. Jerabek, R. Prokop, K. Vrba, "Current gain controlled CCTA and its application in quadrature oscillator and direct frequency modulator", *Radioengineering*, vol.20, no.1, pp.317-326, 2011.
20. W. Jaikla, A. Noppakarn, S. Lawanwisut, "New gain controllable resistor-less current-mode first order allpass filter and its application", *Radioengineering*, vol.21, no.1, pp.312-316, 2012.
21. W. Jaikla, S. Siripongdee, P. Suwanjan, "MISO current-mode biquad filter with independent control of pole frequency and quality factor", *Radioengineering*, vol.21, no.3, pp.886-891, 2012.
22. W. Tangsrirat, "Simple BiCMOS CCCTA design and resistorless analog function realization", *The Scientific World Journal*, vol. 2014, Article ID 423979, 7 pages, <http://dx.doi.org/10.1155/2014/423979>, 2014.
23. R. C. Dorf, R. H. Bishop, *Modern Control Systems, 11th-edition*, New Jersey, Pearson prentice Hall, 2008.
24. S. S. Gupta, R. Senani, "State variable synthesis of single resistance controlled grounded capacitor oscillator using only two CFOAs", *IEE Proc. Circuits Devices Syst.*, vol.145, no.2, pp.135-138, 1998.
25. W. Tangsrirat, T. Pukkalanun, "Structural generation of two integrator loop filters using CDAs and grounded capacitors", *Int. J. Circ. Theor. Appl.*, vol.39, no.1, pp.31-45, 2011.

Arrived: 02. 07. 2016

Accepted: 01. 09. 2016

Solution-derived $Ba_{0.5}Sr_{0.5}TiO_3$ thin-film capacitors in metal-insulator-metal configuration

Tanja Pečnik^{1,2}, Sebastjan Glinšek³, Brigita Kmet¹, Barbara Malič^{1,2}

¹Electronic Ceramics Department, Jožef Stefan Institute, Ljubljana, Slovenia

²Jožef Stefan International Postgraduate School, Ljubljana, Slovenia

³CEA Grenoble, LETI, Minatec Campus, Grenoble, France

Abstract: The $Ba_{0.5}Sr_{0.5}TiO_3$ (BST 50/50) thin films with the thicknesses ~ 250 nm were deposited on polycrystalline alumina substrates by Chemical Solution Deposition. The films were prepared by the multi-step annealing process at 750 °C, 800 °C and 900 °C and the effect of the annealing temperature on the phase composition, microstructure and dielectric properties of the films was studied. All BST 50/50 films crystallize in a pure perovskite phase after heating in a rapid thermal annealing furnace. The microstructure of the film annealed at 750 °C is granular with ~ 30 nm sized grains. As the annealing temperature increases to 800 °C the granular microstructure remains and the average lateral grain size increases to ~ 70 nm, while the film annealed at 900 °C consists of predominantly columnar grains with the average lateral size ~ 100 nm. The kHz-range dielectric permittivity increases from 350 for the film annealed at 750 °C to 480 for the film annealed at 900 °C.

Keywords: (Ba,Sr)TiO₃; thin films; microstructure; dielectric properties

Tankoplastni kondenzatorji na osnovi $Ba_{0.5}Sr_{0.5}TiO_3$, pripravljenega s sintezo v raztopini, s konfiguracijo kovina - dielektrik - kovina

Izveček: Tanke plasti $Ba_{0.5}Sr_{0.5}TiO_3$ (BST 50/50) z debelino ~ 250 nm smo pripravili na podlagah polikristaliničnega aluminijevega oksida s sintezo v raztopini. Vzorci smo pripravili z večstopenjskim segrevanjem pri temperaturah 750 °C, 800 °C in 900 °C in raziskovali vpliv temperature segrevanja na fazno sestavo, mikrostrukturo in dielektrične lastnosti plasti. Ugotovili smo, da vse plasti BST 50/50 kristalizirajo v čisti perovskitni fazi in da je mikrostruktura plasti, segretil pri temperaturi 750 °C fino zrnata, s ~ 30 nm velikimi zrnji. Z višjo temperaturo segrevanja, 800 °C, se je povprečna velikost zrn povečala na ~ 70 nm. Mikrostrukturo plasti, žganih pri 900 °C, sestavljajo pretežno stebričasta zrna s povprečno lateralno velikostjo ~ 100 nm. Dielektričnost plasti, izmerjena v kHz frekvenčnem območju, se je s povišanjem temperature segrevanja s 750 °C na 900 °C povečala s 350 na 480.

Ključne besede: (Ba,Sr)TiO₃; tanke plasti; mikrostruktura; dielektrične lastnosti

*Corresponding Author's e-mail: tanja.pecnik@ijs.si

1 Introduction

Barium strontium titanate $Ba_xSr_{1-x}TiO_3$, $x=0-1$ (BST) is a complex perovskite material, whose phase transition temperature (Curie temperature) from paraelectric to ferroelectric phase is tuned by the Ba/Sr ratio, from ~ 0 K for $x=0$ to ~ 400 K for $x=1$. Consequently also the dielectric properties of BST are tuned by the composition. In the paraelectric phase, yet close above the Curie temperature, the BST exhibits high dielectric per-

mittivity and tunability, i.e. electric-field dependence of dielectric permittivity, but also low dielectric losses in GHz frequency range, which makes it suitable for the use in tunable microwave devices [1], [2].

In the case of solution-derived thin films different factors such as film thickness, grain size and shape [3–7], porosity [8], residual stress [6], [9], interaction with the electrodes [1], etc., strongly modify the response of the

films and therefore their effect should be considered. For example Sinnamon et al. [10] prepared BST 50/50 thin films with the thicknesses in the range from 15 nm to 1.5 μm by pulsed laser deposition on $\text{SrRuO}_3/\text{MgO}$ substrates. The authors showed that as the film thickness increased from 15 nm to 1.5 μm the respective average lateral grain size increased from 80 nm to 460 nm. Consequently, the dielectric permittivity, measured at 10 kHz, strongly increased from around 50 for the thinnest to 650 for the thickest film. Aygün et al. [7] studied the influence of the annealing process, i.e. one-, two- or multi-step, on the microstructure of $\sim 550\text{-nm}$ -thick BaTiO_3 thin films deposited by spin-coating on copper foils. When the films were prepared by one-step annealing, where multiple deposits were annealed only once at 900 °C, the films consisted of a granular microstructure with ~ 100 nm large grains and fine pores between the grains. The films prepared by the multi-step annealing, where each of many deposits was annealed separately at 900 °C, consisted of a dense and columnar microstructure with the average lateral grain size ~ 185 nm. The authors found that the change of the granular to the columnar microstructure and a reduced level of porosity strongly influenced the kHz-range dielectric permittivity (measured at room temperature) of the films; the dielectric permittivity increased from ~ 1500 for the BaTiO_3 film with the granular microstructure to above 3000 for the film with the columnar microstructure.

In this work we focused on the preparation of $\text{Ba}_{0.5}\text{Sr}_{0.5}\text{TiO}_3$ (BST 50/50) thin-film capacitors in a metal-insulator-metal configuration on platinized alumina substrates. We studied the influence of the annealing temperature on the phase composition, microstructure and dielectric properties of the films, measured in the kHz range and at room temperature.

2 Materials and methods

The BST 50/50 coating solution was synthesized from the earth-alkaline acetates ($\text{Ba}(\text{CH}_3\text{COO})_2$, 99.999 %, Alfa Aesar, $\text{Sr}(\text{CH}_3\text{COO})_2$, 99.81 %, Alfa Aesar) and Ti-butoxide ($\text{Ti}(\text{OC}_4\text{H}_9)_4$, 99.61 %, Fluka). The acetates were dried before use and then dissolved in acetic acid (100 %, Merck) and Ti-butoxide was diluted by the 2-methoxyethanol ($\text{CH}_3\text{OCH}_2\text{CH}_2\text{OH}$, 99.3+ %, Sigma Aldrich). The two solutions were mixed for 2 hours at room temperature and the concentration of the solution was adjusted to 0.25 M.

Prior deposition of the films the platinum with the thickness of ~ 100 nm was RF-sputtered on polished alumina substrates (99.6 %, 3.95 g/cm^3 , $25.4\text{ mm} \times 25.4$

$\text{mm} \times 0.26\text{ mm}$, Coorstek). The BST 50/50 solution was then deposited on the substrates by spin-coating, followed by drying at 200 °C for 2 min and pyrolysis at 350 °C for 2 min. After each deposition-drying-pyrolysis step the films were heated in a rapid thermal annealing furnace (LPT, TM100-BT) at temperatures between 750 °C and 900 °C with the heating rate of 15 K/s. The time of annealing of the first deposit was 15 min, intermediate deposits were annealed for 5 min and the final deposit for 60 min. The deposition-drying-pyrolysis-annealing steps (multi-step annealing) were repeated seven times to reach the final thickness of ~ 250 nm.

The phase composition of all BST 50/50 thin films was determined by PANalytical X'Pert PRO MPD X-ray diffractometer (XRD) with $\text{CuK}\alpha 1$ radiation. The XRD patterns were recorded in a 2θ region from 10 ° to 50 ° with the step of 0.017 ° and the exposure time of 100 s.

The surface and cross-section microstructures of the films were analyzed with a field-emission scanning electron microscope (FE-SEM, JSM-7600F, JEOL). The average lateral grain sizes of the BST 50/50 films were determined by the linear-intercept method based on the FE-SEM surface micrographs.

For investigation of dielectric properties in the kHz frequency range Cr/Au top electrodes with a diameter of 0.4 mm were deposited by magnetron sputtering (5 Pa, Milano, Italy). Capacitance-voltage characteristics, measured at 100 kHz, were recorded with the following DC biasing scheme: $0\text{ V} \rightarrow +5\text{ V} \rightarrow 0\text{ V} \rightarrow -5\text{ V} \rightarrow 0\text{ V}$.

3 Results and discussion

3.1 Phase composition

The XRD patterns of BST 50/50 films annealed at 750 °C and 900 °C are shown in Figure 1. The platinized alumina substrate is added as a reference. Since the intensities of the substrate are much higher than the intensities of the perovskite BST 50/50 phase, the peaks belonging to the substrate were reduced and are denoted by *. According to the XRD analysis all films (not shown here for the film annealed at 800 °C) crystallize in a randomly oriented perovskite phase. With increasing annealing temperature the intensities of the perovskite diffraction peaks increase and the full width at half maximum decreases, indicating improved crystallinity of the films and larger crystallite sizes.

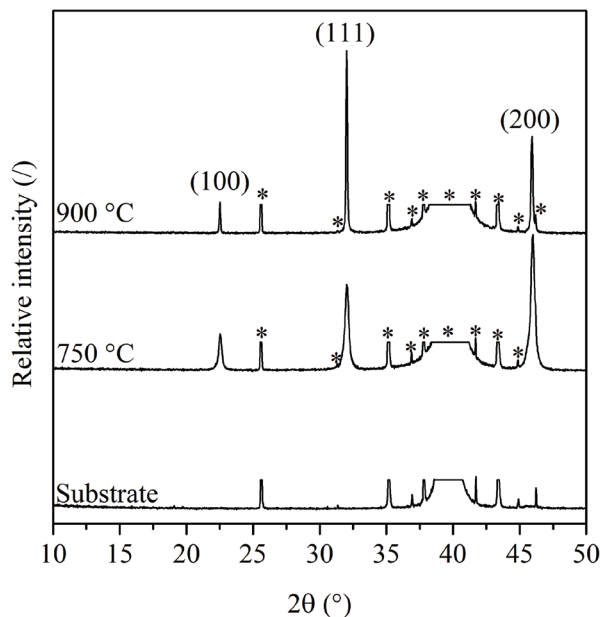


Figure 1: XRD patterns of the BST 50/50 films prepared on platinized alumina substrate at 750 °C and 900 °C. The peaks corresponding to the perovskite phase are denoted with the Miller indices [11]. The pattern of the substrate is also shown as a reference. * - reduced peaks of the substrate.

3.2 Microstructure

The FE-SEM cross-section and plan-view micrographs of BST 50/50 films annealed at temperatures between 750 °C and 900 °C are presented in Figures 2 and 3. The thickness of the film annealed at 750 °C, determined from the cross-section micrograph, is 260 nm and decreases to 210 nm as the annealing temperature increases to 900 °C. The decrease of the film thickness with increasing annealing temperature, shown also in Figure 4, indicates densification of the films.

The film annealed at 750 °C consists of equiaxed grains with the average lateral size of approximately 30 nm. The surface micrograph presented in Figure 3 shows that the microstructure of the film is uniform with some fine pores between the grains. A similar granular microstructure with the grains of a few tens of nm has been commonly observed in the case of the solution-derived BaTiO_3 , SrTiO_3 and BST thin films prepared by one- or two-step annealing processes and forms via predominantly homogenous nucleation mechanism [5], [12], [13].

With increasing the annealing temperature to 800 °C the average lateral grain size increases to approximately 70 nm and the porosity and pore size decrease, as is observed from the surface microstructure of the film in Figure 3. With further increase of the anneal-

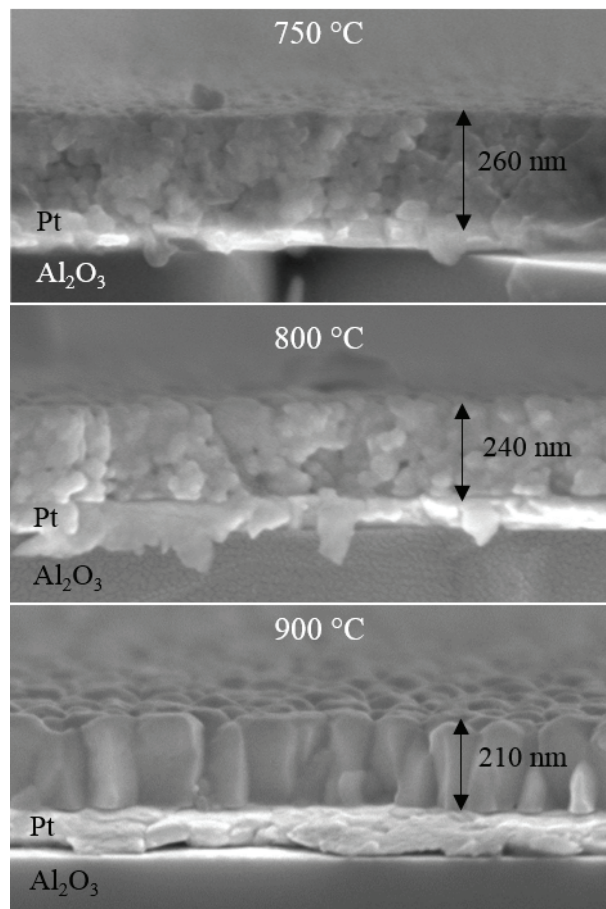


Figure 2: The FE-SEM cross-section micrographs of the BST 50/50 films annealed at temperatures between 750 °C and 900 °C.

ing temperature to 900 °C the average lateral grain size increases to almost 100 nm, the microstructure is uniform, dense and predominantly columnar with the grains that extend through the whole film thickness, as is shown in Figure 2. The dependence of the grain size on the annealing temperature is shown also in Figure 4; evidently the microstructure is coarsening in parallel with the enhanced densification, evidenced as the decrease of the film thickness. The dense microstructure of the film annealed at 900 °C is related to the multi-step heat treatment where each deposit is annealed after drying and pyrolysis, which was also reported for solution-derived BaTiO_3 , SrTiO_3 and BST thin films prepared by the multi-step annealing process by different research groups [5], [7], [14], [15].

3.3 Dielectric properties

Dielectric permittivity and losses of the BST 50/50 thin films annealed at temperatures between 750 °C and 900 °C are plotted in Figure 5. The dielectric permittivity and losses of the BST 50/50 film annealed at 750 °C are 350 and 0.037, measured at 100 kHz and room tem-

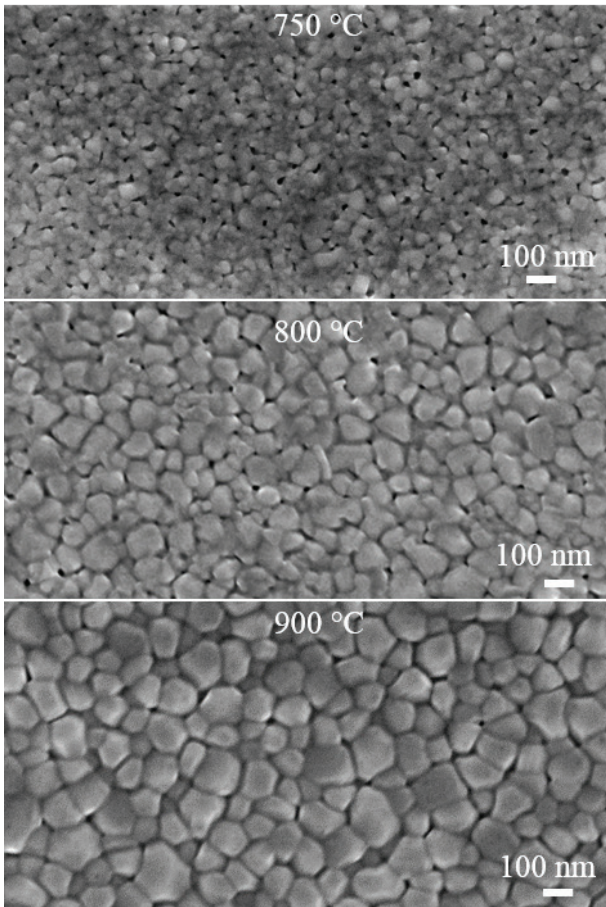


Figure 3: The FE-SEM surface micrographs of the BST 50/50 films annealed at temperatures between 750 °C and 900 °C.

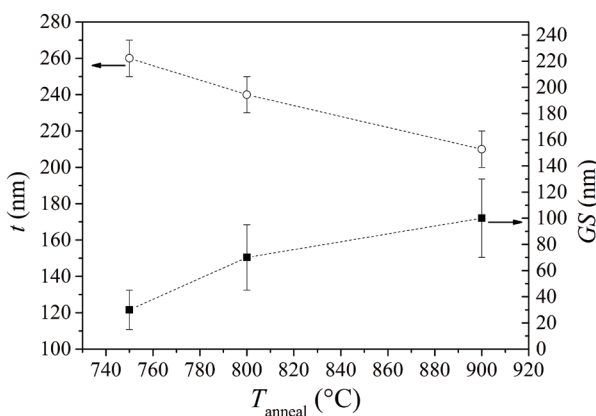


Figure 4: The dependence of the film thickness t and grain size GS on the annealing temperature T_{anneal} of the BST 50/50 thin films.

perature. With increasing the annealing temperature to 900 °C the dielectric permittivity increases to 480 and the losses remain similar, around 0.042. We connect the increase of the dielectric permittivity of the BST

50/50 films with increasing annealing temperature to the change of the granular and porous to the columnar and dense microstructure of the films, which is consistent with observations from the literature [5], [7], [15].

The voltage / electric-field dependence of the permittivity and dielectric losses of BST 50/50 film, which was annealed at 750 °C, measured at 100 kHz and 300 K, is presented in Figure 6. The tunability, expressed as the ratio of the permittivity at 0 V and 5 V, is 1.3 (23 %).

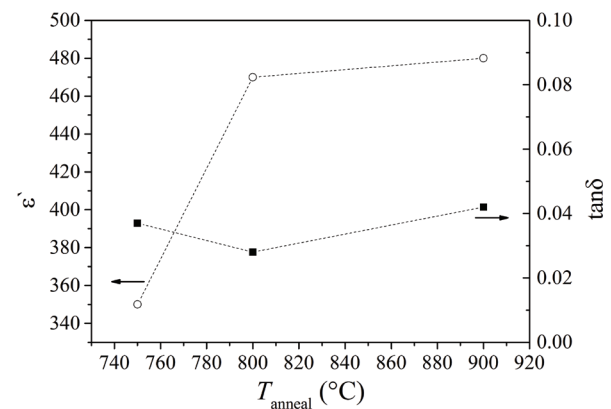


Figure 5: Dielectric permittivity ϵ' and dielectric losses $\tan\delta$ of BST 50/50 thin films annealed at temperatures (T_{anneal}) between 750 °C and 900 °C. The dielectric properties were measured at 100 kHz and at room temperature.

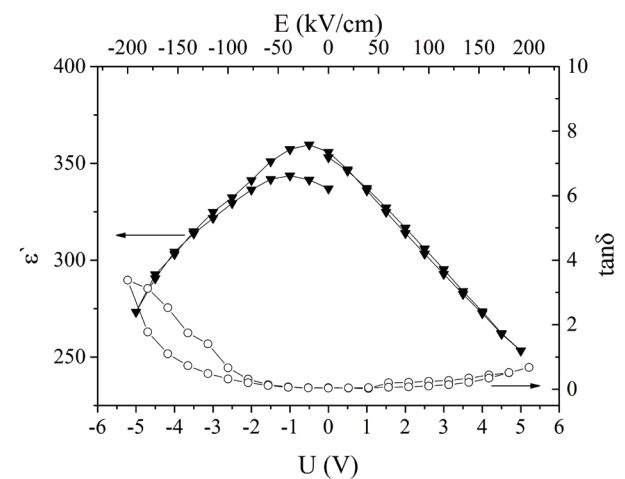


Figure 6: The voltage (and field) dependence of the dielectric permittivity and losses for the BST 50/50 film annealed at 750 °C, measured at 100 kHz and room temperature.

A hysteresis is observed in both curves (see Figure 6) as well as an increase of the dielectric losses as the electric field exceeds -80 kV/cm. The origin for the hysteresis in the films in the paraelectric phase could be related to the presence of polar-nano regions [16] or to the pres-

ence of oxygen vacancies and space charges at the interface between the film and the substrate and/or at the grain boundaries [17]. However, explaining this phenomenon by a specific mechanism would require a further study.

4 Conclusions

The effect of the annealing temperature on the phase composition, microstructure and dielectric properties of solution-derived BST 50/50 films prepared on platinumized alumina substrates was studied. According to the XRD analysis all films crystallized in a pure perovskite phase after rapid annealing at temperatures between 750 °C and 900 °C. The FE-SEM analysis revealed that the film prepared at 750 °C was 260 nm thick and that the thickness decreased to 210 nm with increasing annealing temperature to 900 °C, indicating improved densification. The film annealed at 750 °C consisted of approximately 30-nm-sized equiaxed grains. The surface microstructure was uniform and some fine pores were observed between the grains. As the annealing temperature increased to 800 °C the grains were around 70 nm in size and the porosity and pore size decreased. When the BST 50/50 film was annealed at higher temperature, i.e. 900 °C, it consisted of columnar grains with average lateral grain size around 100 nm. The dielectric permittivity of the film annealed at 750 °C was 350 and it increased to 480 with increasing annealing temperature to 900 °C, which we relate to the change of the grain size and shape and reduced level of porosity.

5 Acknowledgments

This work was supported by the Slovenian Research Agency (P2-0105, PR-05026 and J2-5482).

6 References

1. A. K. Tagantsev, V. O. Sherman, K. F. Astafiev, J. Venkatesh, and N. Setter, "Ferroelectric Materials for Microwave Tunable Applications," *Journal of Electroceramics*, vol. 11, no. 1, pp. 5–66, 2004.
2. P. Bao, T. J. Jackson, X. Wang, and M. J. Lancaster, "Barium strontium titanate thin film varactors for room-temperature microwave device applications," *Journal of Physics D: Applied Physics*, vol. 41, no. 6, pp. 063001–1–21, 2008.
3. M. H. Frey, Z. Xu, P. Han, and D. A. Payne, "The role of interfaces on an apparent grain size effect on the dielectric properties for ferroelectric barium titanate ceramics," *Ferroelectrics*, vol. 206–207, pp. 337–353, 1998.
4. K. Kageyama, A. Sakurai, A. Ando, and Y. Sakabe, "Thickness effects on microwave properties of (Ba,Sr)TiO₃ films for frequency agile technologies," *Journal of the European Ceramic Society*, vol. 26, no. 10–11, pp. 1873–1877, 2006.
5. S. Hoffmann and R. Waser, "Control of the morphology of CSD-prepared (Ba,Sr)TiO₃ thin films," *Journal of the European Ceramic Society*, vol. 19, no. 6–7, pp. 1339–1343, 1999.
6. T. Pečnik, S. Glinšek, B. Kmet, and B. Malič, "Combined effects of thickness, grain size and residual stress on the dielectric properties of Ba_{0.5}Sr_{0.5}TiO₃ thin films," *Journal of Alloys and Compounds*, vol. 646, pp. 766–772, 2015.
7. S. M. Aygün, J. F. Ihlefeld, W. J. Borland, and J.-P. Maria, "Permittivity scaling in Ba_{1-x}Sr_xTiO₃ thin films and ceramics," *Journal of Applied Physics*, vol. 109, no. 3, pp. 034108–1–5, 2011.
8. T. Ostapchuk, J. Petzelt, I. Rychetský, V. Porokhonsky, B. Malič, M. Kosec, and P. Vilarinho, "Influence of porosity on the dielectric response and central-mode dynamics in PbZrO₃ ceramics," *Ferroelectrics*, vol. 298, no. 1, pp. 211–218, 2004.
9. E. A. Fardin, A. S. Holland, K. Ghorbani, E. K. Akdogan, W. K. Simon, A. Safari, and J. Y. Wang, "Polycrystalline Ba_{0.6}Sr_{0.4}TiO₃ thin films on r-plane sapphire: Effect of film thickness on strain and dielectric properties," *Applied Physics Letters*, vol. 89, no. 18, pp. 182907–1–3, 2006.
10. L. J. Sinnamon, M. M. Saad, R. M. Bowman, and J. M. Gregg, "Exploring grain size as a cause for 'dead-layer' effects in thin film capacitors," *Applied Physics Letters*, vol. 81, no. 4, pp. 703–705, 2002.
11. "PDF 00-039-1395." JCPDS-International Center for Diffraction Data, Newton Square, 2002.
12. R. W. Schwartz, P. G. Clem, J. A. Voigt, E. R. Byhoff, M. Van Stry, T. J. Headley, and N. A. Missert, "Control of microstructure and orientation in solution-deposited BaTiO₃ and SrTiO₃ thin films," *Journal of the American Ceramic Society*, vol. 82, no. 9, pp. 2359–2367, 1999.
13. B. Malič, I. Boerasu, M. Mandeljc, M. Kosec, V. Sherman, T. Yamada, N. Setter, and M. Vukadinovic, "Processing and dielectric characterization of Ba_{0.3}Sr_{0.7}TiO₃ thin films on alumina substrates," *Journal of the European Ceramic Society*, vol. 27, no. 8–9, pp. 2945–2948, 2007.
14. C. Jia and K. Urban, "Microstructure of columnar-grained SrTiO₃ and BaTiO₃ thin films prepared by chemical solution deposition," *Journal of Materials Research*, vol. 13, no. 8, pp. 2206–2217, 1998.
15. K. Kageyama, T. Hosokura, T. Nakaiso, and H. Takagi, "Dielectric properties of (Ba,Sr)TiO₃ thin

- films with varied microstructures prepared by the chemical solution deposition method for thin-film capacitors and ferroelectric varactors," *IEEE transactions on ultrasonics, ferroelectrics, and frequency control*, vol. 57, no. 10, pp. 2198–204, 2010.
16. H. W. Jang, A. Kumar, S. Denev, M. D. Biegalski, P. Maksymovych, C. W. Bark, C. T. Nelson, C. M. Folkman, S. H. Baek, N. Balke, C. M. Brooks, D. A. Tenne, D. G. Schlom, L. Q. Chen, X. Q. Pan, S. V. Kalinin, V. Gopalan, and C. B. Eom, "Ferroelectricity in strain-free SrTiO₃ thin films," *Physical Review Letters*, vol. 104, no. 19, pp. 197601–1–4, 2010.
 17. X. H. Zhu, L. P. Yong, H. F. Tian, W. Peng, J. Q. Li, and D. N. Zheng, "The origin of the weak ferroelectric-like hysteresis effect in paraelectric Ba_{0.5}Sr_{0.5}TiO₃ thin films grown epitaxially on LaAlO₃," *Journal of Physics: Condensed Matter*, vol. 18, no. 19, pp. 4709–4718, 2006.

Arrived: 31.08.2016

Accepted: 22.09.2016

Temperature and Injection Current dependent Electroluminescence for Evaluation of Single-Junction Single-Segment GaAs Laser Power Converter

Rok Kimovec¹, Henning Helmers², Andreas W. Bett² and Marko Topič¹

¹University of Ljubljana, Faculty of Electrical Engineering, Ljubljana, Slovenia

²Fraunhofer Institute for Solar Energy Systems ISE, Freiburg, Germany

Abstract: The spatial electroluminescence intensity and spectral measurements of photovoltaic devices under forward bias have proved to be fast and reliable characterization tools. They enable quick evaluation of material and manufacturing quality and provide information linked to local performance of photovoltaic devices in different operating conditions.

In this work, EL images of single-junction single-segment GaAs laser power converters (LPC) and their emission spectra depending on the injection current and LPC temperature are presented and analyzed. A shift of the EL emission peak to smaller energies and a decrease in EL intensity with increasing temperature are observed in spectrally resolved EL measurements. Negative temperature coefficients dEL/dT of EL intensity depending on the injection current are extracted from spatially resolved EL measurements. EL images of the LPCs under low and high injection currents are presented and evaluated.

Keywords: electroluminescence; laser power converter; Power-over-Fiber; power-by-light; spatial electroluminescence; spectral electroluminescence; LPC

Vpliv temperature in vzbujalnega toka na elektroluminiscenco enosegmentnih enospojnih pretvornikov laserske moči

Izveček: Meritve prostorske in spektralne elektroluminiscence fotovoltaičnih struktur so se izkazale za zanesljivo in hitro karakterizacijsko orodje. Omogočajo nam vpogled v kvaliteto uporabljenega materiala in izdelave struktur ter nam podajo možnost vpogleda v spreminjanje kazalcev učinkovitosti pri spreminjajočih delovnih pogojih.

V tem delu so predstavljene meritve in analiza prostorske in spektralne elektroluminiscence v odvisnosti od delovne temperature in vzbujalnega toka za primer enosegmentnega enospojnega pretvornika laserske moči izdelanega iz GaAs. Z višanjem temperature se intenziteta izsevane svetlobe zmanjša, izsevani spekter pa se premakne proti nižjim energijam. Iz analize prostorske elektroluminiscence je izračunan negativni temperaturni koeficient intenzitete izsevane svetlobe dEL/dT pri različnih vzbujalnih tokovih. Predstavljena je analiza slik prostorske elektroluminiscence za primer majhnega in velikega vzbujalnega toka.

Ključne besede: elektroluminiscenca; pretvornik laserske moči; Moč-po-vlaknu; prostorska elektroluminiscenca; spektralna elektroluminiscenca

* Corresponding Author's e-mail: rok.kimovec@fe.uni-lj.si

1 Introduction

Electroluminescence (EL) in photovoltaic (PV) devices is a phenomenon occurring due to radiative recombination of electrically excited charge carriers, resulting

in the emission of photons from the PV device structure. The measurement of EL, coupled with theoretical knowledge, has become an important tool in assessing performance of PV devices in both scientific and indus-

trial environments [1–4], due to fast acquisition times of modern imaging devices.

For purposes of Power-over-Fiber (PoF) (or “power-by-light”) [5, 6], where optical energy in the form of laser light is transferred through electrically nonconductive optical fiber, special types of PV devices (laser power converters (LPC)) are utilized to convert monochromatic light to electricity [7, 8]. As for all other PV devices, performance of LPCs is upwards limited [9] and it can be evaluated to some extent by the use of spatially and spectrally resolved EL measurements.

The aim of this work is to gain insight into spatially and spectrally resolved characterization techniques and performance of LPCs under various operation temperatures and current densities.

2 Motivation

PoF is an emerging technology used for powering various electronic devices in extreme environments, where benefits such as galvanic isolation and electromagnetic compatibility overcome the additional cost and complexity of such power supply systems [10, 11].

To gain in-depth understanding of PoF systems, evaluation of individual components has to be undertaken. In this work we concentrate on assessing the performance of LPCs using advanced spatially resolved characterization techniques. The LPC is the part of the system which is converting monochromatic light into electricity, thus providing electrical energy to an electronic device at a remote location. Since such systems are used for powering a variety of electronic devices (e.g. sensors [12], cameras [13], actuators, etc.) in many different environments (e.g. space [14], high magnetic fields [15], etc.), they must perform well in different operating conditions, such as variation in temperature and power requirements for different electronic devices.

In order to understand the behavior and performance of LPCs in different working conditions better, an analysis of EL at various temperatures and injection currents has been performed and is presented in this paper.

3 Description of specimen

The investigated LPC sample is a single-junction single-segment (SJ-SS) GaAs photovoltaic device fabricated at Fraunhofer ISE. The active region is a 3.65 μm thick *pin*-stack with an n-type emitter of 120 nm thickness.

It employs 25 nm AlInP window-layer on top of the emitter which acts as a passivation layer (front surface field). The p-doped base layer follows a back surface field (BSF) layer in order to passivate the rear side of the active solar cell. A schematic representation of the device structure is shown in Figure 1 (a). The chip area is 3 mm x 3 mm square with front contact circular busbar design, which covers 2 mm² of the area. An image of the device under test (DUT) is shown in Figure 1 (b).

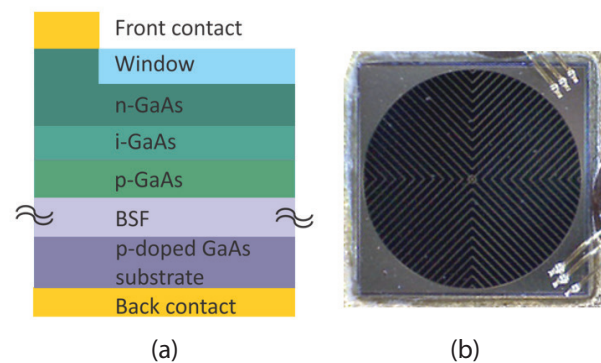


Figure 1: (a) Schematic of the investigated LPC. (b) Top view of 3 mm x 3 mm square LPC sample. Even though the device is wire bonded to a TO-header in two corners only the top right connection was used for measurement.

4 Experimental setup

In the following the experimental setup and procedures are described, that have been used to measure the spatially and spectrally resolved EL of SJ-SS GaAs LPC at the Laboratory of Photovoltaics and Optoelectronics at the Faculty of Electrical Engineering, University of Ljubljana. The results of the measurements of a SJ-SS GaAs LPC are presented and discussed.

4.1 General measurement description

To perform EL measurements, the LPC sample has been mounted on a temperature controlled chuck and placed into a light proof box, ensuring that only light irradiated by the LPC is measured.

Measurements of injection current and voltage were realized by four-wire connection at various injection current values, provided by an HP E363X series laboratory power supply operating in constant current mode. Current and voltage signals were measured with a pair of HP 34401A multimeters.

The measurement procedure for both spatial and spectral EL was as follows:

- Setting of desired injection current
- Setting of desired temperature

- Setting of acquisition time once the temperature was stable, to avoid saturation of the camera/spectrometer
- Measurement of spatial/spectral EL

4.2 Spatially resolved measurement setup

To obtain spatially resolved images a FLI MLx285 scientific camera was used, employing a Sony ICX285 CCD sensor (actively cooled to 0°C). The primary lens on the camera was a Schneider Optics NR56-534. Since the magnification with the primary lens was insufficient to take images of the small area LPC, a microscope objective was mounted on the primary lens with use of tube extenders and a custom made adapter. The described setup enables to acquire sharp EL images of small area LPCs with a resolution higher than 500x500 pixels.

4.3 Spectrally resolved measurement setup

EL spectra were measured with an Ocean Optics HR4000 spectrometer equipped with 600 μm core multimode optical fiber and cosine corrector. The setup was calibrated with a NIST traceable Ocean Optics LS-1-CAL light source prior to the EL measurements. The optical fiber input connector equipped with the cosine corrector was placed in close proximity above the LPC. At large injection currents the current distribution is expected to be non-uniform, leading to large differences of EL irradiation through the front surface of the LPC. Care was taken to assure that all irradiated light from the device under test was coupled into the fiber.

Even though the spectrum acquisition system was calibrated prior to measurement, it should be noted that such measurement systems are insufficient to measure absolute irradiance values, so that all spectral measurements results are expressed in arbitrary units. Still, they can serve for relative comparison of LPCs at varying operating conditions.

5 Results

5.1 Spatially resolved measurements

To perform analysis of images captured by the CCD camera, two corrections of the raw data were performed. First, the dark image was subtracted from all images. Second, individual pixel values were divided by acquisition time, resulting in each pixel value presented in counts per second acquired by the CCD. Further details on the measurement procedure and image manipulation procedure can be found elsewhere [16].

Acquired images from spatially resolved EL enable to perform two different types of analysis. First it is a quali-

tative analysis in which the material homogeneity can be evaluated at low injection currents. At high injection currents on the contrary, the influence of the busbar and sheet series resistances on the current distribution can be seen through the top layers of the device. The results of such an analysis are shown in Figure 2 and Figure 3 for two different injection currents (1 mA, 400 mA). Under the injection current of 1 mA (Figure 2) the LPC shows a mostly uniform electroluminescence across the whole cell area, which can be attributed to a homogeneous material quality of the GaAs crystal.

With an injection current of 400 mA (Figure 3), the measured EL intensity distribution across the LPC area decreases from the top right corner to the bottom left corner. This behavior can be explained by non-ideal contacting of the specimen. Opposed to an ideal contacting in each corner of the device, wire bonds were

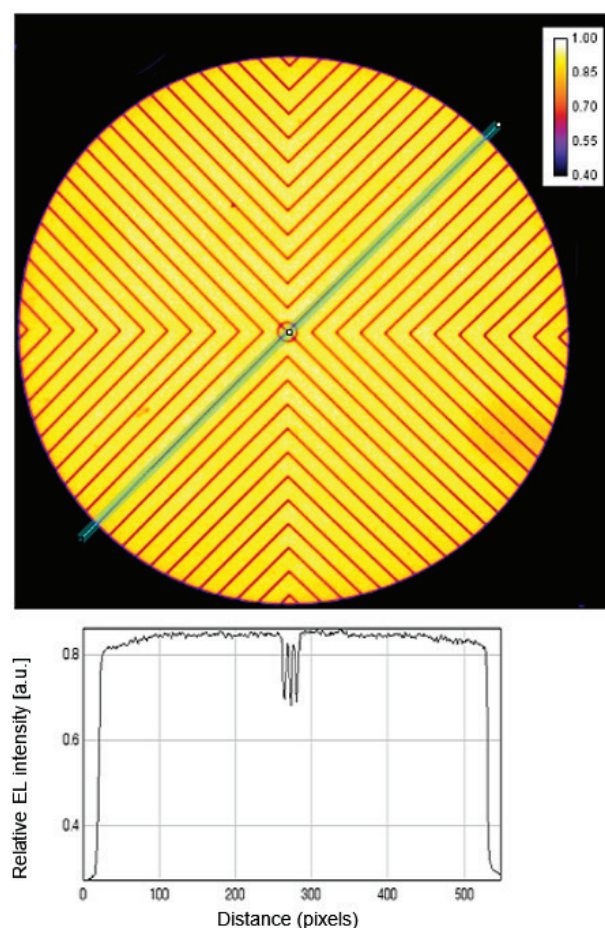


Figure 2: Top: Normalized EL image of a SJ-SS GaAs LPC at an injection current of 1 mA. The metallized front grid is visible as dark lines in the EL image. Bottom: Plot of the normalized EL along line scan, marked with cyan, showing an even distribution of the current. Note that the line used for the line scan is actually a rectangle, which covers a narrow area of the LPC beside the central finger.

only placed in the top right and bottom right corner (compare Fig. 1b), of which only the three wire bonds in the top right corner were electrically contacted during the measurements described in this work. Thus, the injected current needs to redistribute from the top right corner to the rest of the busbar metallization. For high current conditions the narrowest sections of the busbar represent a significant bottleneck to the current flow, resulting in a significant voltage drop at those points. For a device contacted in all four corners, this voltage drop would not occur and the EL profile is expected to be radially symmetrical, with the EL signal decaying from the border to the center of the active area. A second effect is seen as a decay of EL from the top right corner to the center of the LPC. This effect can be explained by a voltage drop at the grid and top

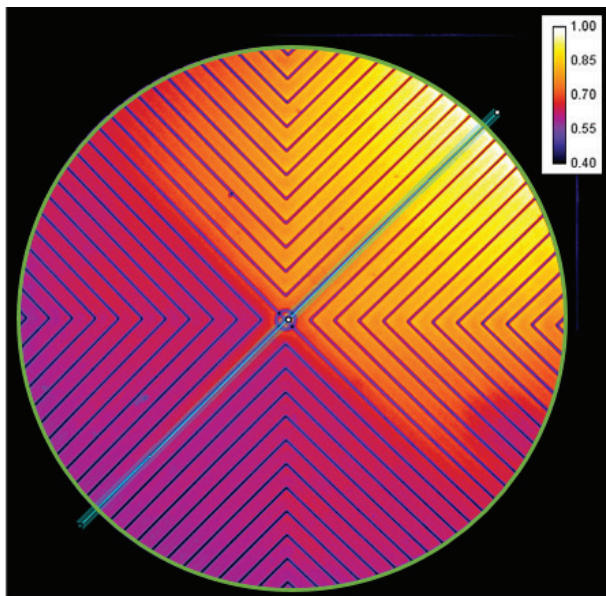


Figure 3: Top: Normalized EL image of a SJ-SS GaAs LPC with injection current 400 mA. The metallized front grid is visible as dark lines in the EL image. Bottom: Plot of normalized EL along a line scan, marked with cyan, showing a combination of various resistances on the EL profile through the active area. Note that the line used for the line scan is actually a rectangle, which covers an area of the LPC beside the central finger. The green circle marks the central active region, taken for calculations of the relative quantitative analysis.

surface resistance and would stay the same, regardless the connection of the LPC to the external contacts. A combination of both effects, can be clearly seen in normalized EL along the line scan, marked with a cyan line in Figure 3. To mitigate resistance losses from lateral conduction above the pn-junction, recent designs of LPCs employ a so-called lateral conduction layer [17]. This layer is composed of a highly doped material with a bandgap larger than the photon energy of the impinging light – making it transparent for the used laser wavelength.

In addition to the qualitative assessment of the current distribution, the spatially resolved EL measurements can also be assessed for a relative quantitative analysis. Therefore, the mean pixel value of the circular active region (marked with a green circle in Figure 3) is calculated and used for normalization of all EL images (various injection currents and temperatures). In Figure 4 the resulting counts per second are plotted, as recorded by the CCD camera after subtraction of the dark image. Consequently, this value corresponds to the dependency of the EL intensity on the injection current and temperature.

The shapes of the EL curves can be described by a power-law current dependence [18].

$$EL_{\frac{counts}{s}}(T) = k_{CCD} C(T) I^{b(T)} \tag{1}$$

k_{CCD} is the efficiency of CCD sensor and optics and $C(T)$ and $b(T)$ are in general temperature dependent coefficients. Similar behavior of EL vs. current was previously observed for various photovoltaic devices [16], [19, 20].

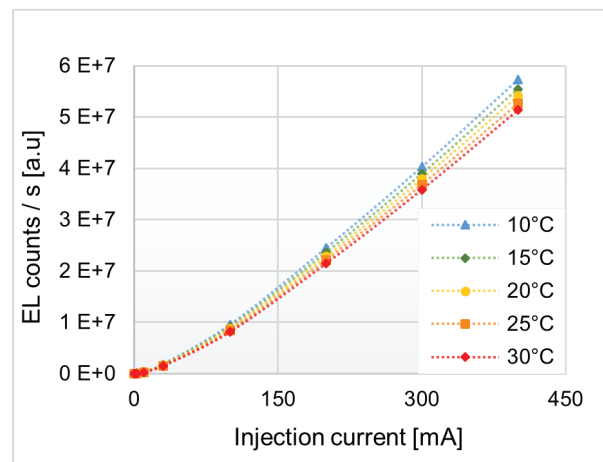


Figure 4: Plot of EL intensity vs. injection current from SJ-SS GaAs LPC extracted from mean pixel values of processed EL images at various temperatures.

In Figure 6 the EL intensity is plotted normalized to the value at $T=10^{\circ}\text{C}$ as a function of temperature. As can be seen, for all injection currents the EL intensity decreases with increasing temperature. The corresponding negative temperature coefficient depends on injection currents. Increasing temperature has a larger impact on EL for lower injection currents as seen in Figure 5. Temperature coefficients dEL/dT change from $-1.5\ \%/^{\circ}\text{C}$ for injection current of 1 mA to $-0.5\ \%/^{\circ}\text{C}$ for injection current of 400 mA.

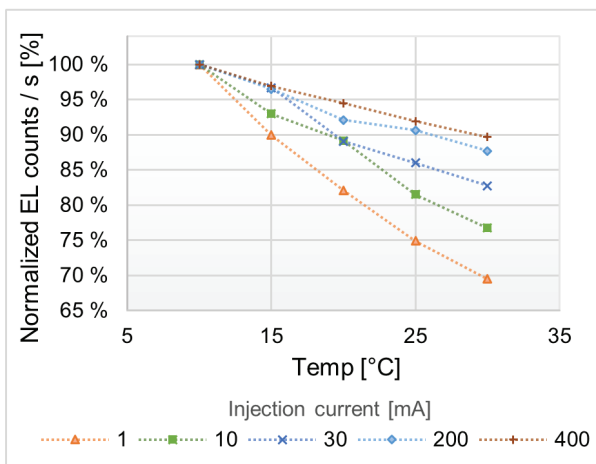


Figure 5: Temperature dependence of the EL intensity extracted from mean pixel values of processed EL images at different injection currents.

5.2 Spectrally resolved measurements

While spatially resolved EL characterization enables quick, qualitative analysis, it lacks information on the spectral distribution of the emitted light. Since the spectrum of emitted light corresponds to the bandgap of the direct semiconductor, it provides information about the change of the absorber material’s bandgap with temperature. As can be seen in Figure 6, increasing temperature results in two different effects: Firstly, the EL emission peak is shifted to lower energies, as expected due to the dilation of the crystal lattice and corresponding decrease in bandgap described by the following equation [21]:

$$E_g = E_0 - \alpha \frac{T^2}{T + \beta} \quad (2)$$

where E_g is the bandgap and E_0 , α and β are material dependent parameters. The measured temperature coefficient $dE_{g_meas}/dT = -0.46\ \text{meV/K}$ agrees well with the published value for that temperature range $dE_{g_pub}/dT = 0.45\ \text{meV/K}$ [22, 23].

Secondly, it provides insight into how EL emission decreases with rising temperature. While the slope at low-

er energies (i.e. below the bandgap) remains constant, the slope at higher energies (i.e. above the bandgap) decreases with increasing temperature. This has been observed and explained before [4].

In a PoF system, the LPC is illuminated by a laser diode. Since the laser diode will typically be temperature controlled, the wavelength and thus photon energy of the laser will be constant. With maximal absorption current generation results of the impinging monochromatic light is maximized.

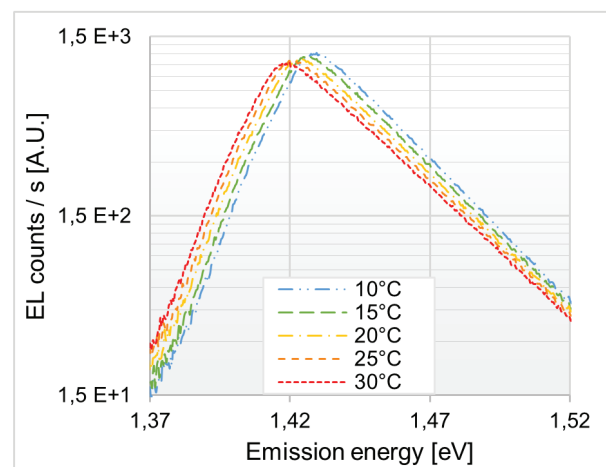


Figure 6: Spectral EL emission of SJ-SS GaAs LPC under constant injection current of 400 mA for various temperatures.

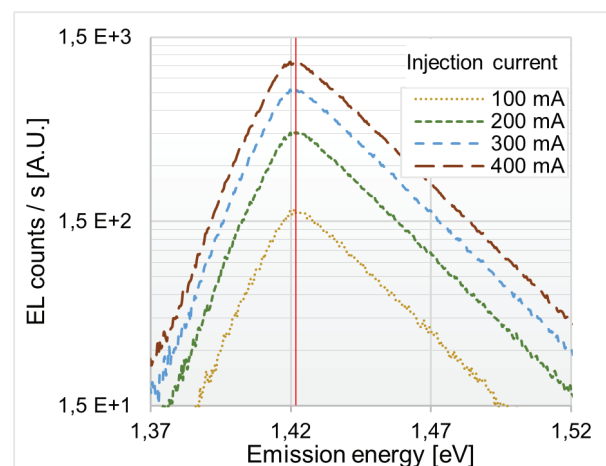


Figure 7: Spectral EL emission of a SJ-SS GaAs LPC at constant temperature of 25 °C at various injection currents. The red line marks the emission peak at 1.422eV ($\approx 872\ \text{nm}$).

To ensure maximal absorption the the photon energy has to be slightly smaller than the bandgap of the LPC absorber material [7]. However, the difference should be small, as the difference in photon and bandgap energy represents an energy loss. It is mainly converted

into heat due to thermalisation of the photo excited carrier towards the band edge. Consequently, a temperature induced drop of E_g leads to increased thermalisation losses for constant photon energy. In other words, since the energy needed to generate an electron-hole pair will decrease with increasing temperature, all excess energy carried by photons of constant wavelength will result in thermal losses. This in turn increases the device temperature even further until an equilibrium is reached.

Injection current dependent spectra at constant temperature are plotted in Figure 7. For the investigated range it can be seen, that the shape of the emission spectra is independent of the injected current.

6 Conclusions

A spatial EL analysis of a SJ-SS LPC sample provided insight on the current distribution and resistive losses of the device under test. It was shown that the magnitude of the EL signal depends on temperature. Thus, for quantitative analysis it is important to take the dependence on temperature into account.

Spatial EL under forward injection current of 1 mA showed that the material and manufacturing quality is homogeneous across the device. Under injection current of 400 mA, a drop in the EL signal from the top right to the lower left side was observed, which can be explained with non-ideal electrical contacting of the device. For optimal performance of the investigated sample, electrical contacts for both EL measurements and operation should be established equally in all four corners.

Temperature dependent spectral EL measurements gave insight into the change of bandgap with increasing temperature. For a Power-over-Fiber system, where the laser diode is typically actively cooled and, thus, the wavelength (=photon energy) stays constant, a temperature induced decrease of absorber bandgap leads to increased thermalisation losses, since photo generated carriers will lose the excess energy by interacting with the crystal lattice and thermalize down to the band edge.

7 Acknowledgments

The authors thank M. Bokalič for fruitful discussions about EL and measurement support and Kasimir Reichmuth for proofreading and comments on the manuscript. The authors acknowledge the financial support from the Slovenian Research Agency (program P2-0197 and PhD funding for R.K.).

8 References

1. A. Delamarre, L. Lombez, and J.-F. Guillemoles, "Characterization of solar cells using electroluminescence and photoluminescence hyperspectral images," *J. Photonics Energy*, vol. 2, no. 1, pp. 027004–1, 2012.
2. J. A. Giesecke, M. Kasemann, and W. Warta, "Determination of local minority carrier diffusion lengths in crystalline silicon from luminescence images," *J. Appl. Phys.*, vol. 106, no. 1, p. 014907, Jul. 2009.
3. U. Rau, "Reciprocity relation between photovoltaic quantum efficiency and electroluminescent emission of solar cells," *Phys. Rev. B*, vol. 76, no. 8, p. 085303, Aug. 2007.
4. C. Karcher, H. Helmers, M. Schachtner, F. Dimroth, and A. W. Bett, "Temperature-dependent electroluminescence and voltages of multi-junction solar cells," *Prog. Photovolt. Res. Appl.*, vol. 22, no. 7, pp. 757–763, Jul. 2014.
5. J.-G. Werthen, S. Widjaja, T.-C. Wu, and J. Liu, "Power over fiber: a review of replacing copper by fiber in critical applications," 2005, p. 58710C–58710C–6.
6. V. Sittakul, L. R. Clare, S. G. Burrow, X. C. Li, and M. J. Cryan, "Power-over-fibre for wireless applications," *Microw. Opt. Technol. Lett.*, vol. 53, no. 5, pp. 1027–1032, May 2011.
7. O. Höhn, A. W. Walker, A. W. Bett, and H. Helmers, "Optimal laser wavelength for efficient laser power converter operation over temperature," *Appl. Phys. Lett.*, vol. 108, no. 24, p. 241104, Jun. 2016.
8. J. Schubert, E. Oliva, F. Dimroth, W. Guter, R. Loockhoff, and A. W. Bett, "High-Voltage GaAs Photovoltaic Laser Power Converters," *IEEE Trans. Electron Devices*, vol. 56, no. 2, pp. 170–175, Feb. 2009.
9. R. Kimovec and M. Topič, "Comparison of Measured Performance and Theoretical Limits of GaAs Laser Power Converters under Monochromatic Light," *Electronics and Energetics* Vol. 30, No 1, DOI: 10.2298/FUEE1701093K, pp. 93 – 106, 2017.
10. K. Worms, C. Klamouris, F. Wegh et al, "Reliable and lightning-safe monitoring of wind turbine rotor blades using optically powered sensors," *Wind Energy*, 2016, DOI: 10.1002/we.2009
11. Y. Tanaka, T. Shioda, T. Kurokawa, J. Oka, K. Ueta, and T. Fukuoka, "Power line monitoring system using fiber optic power supply," *Opt. Rev.*, vol. 16, no. 3, pp. 257–261, 2009.
12. J. Turan, L. Ovsenik, and J. Turan Jr, "Optically Powered Fiber Optic Sensors," *Acta Electrotech. Inform. No*, vol. 5, no. 1, p. 3, 2005.
13. G. Bottger, M. Dreschmann, C. Klamouris, M. Hubner, M. Roger, A. W. Bett, T. Kueng, J. Becker, W. Freude, and J. Leuthold, "An Optically Powered

- Video Camera Link," *IEEE Photonics Technol. Lett.*, vol. 20, no. 1, pp. 39–41, Jan. 2008.
14. R. Peña and C. Algora, "One-watt fiber-based power-by-light system for satellite applications," *Prog. Photovolt. Res. Appl.*, vol. 20, no. 1, pp. 117–123, Jan. 2012.
 15. J. G. Werthen, M. J. Cohen, T. C. Wu, and S. Widjaja, "Electrically isolated power delivery for MRI applications," in *Proc. Int. Soc. Magn. Reson. Med. Annu. Meeting, Seattle, WA, 2006*, p. 1353.
 16. M. Bokalič, J. Raguse, J. R. Sites, and M. Topič, "Analysis of electroluminescence images in small-area circular CdTe solar cells," *J. Appl. Phys.*, vol. 114, no. 12, p. 123102, Sep. 2013.
 17. E. Oliva, F. Dimroth, and A. W. Bett, "GaAs converters for high power densities of laser illumination," *Prog. Photovolt. Res. Appl.*, vol. 16, no. 4, pp. 289–295, Jun. 2008.
 18. K. Wang, D. Han, and M. Silver, "The Power Law Dependence of Electroluminescence Intensity on Forward Current in a-Si:H p-i-n Devices," in *Symposium A – Amorphous Silicon Technology - 1994*, 1994, vol. 336, p. 861 (6 pages).
 19. K. J. Price, A. Vasko, L. Gorrelland, and A. D. Compaan, "Temperature-Dependent Electroluminescence from CdTe/CdS Solar Cells," in *Symposium B – Compound Semiconductor Photovoltaics, 2003*, vol. 763, p. B5.9 (6 pages).
 20. M. Seeland, R. Rösch, and H. Hoppe, "Quantitative analysis of electroluminescence images from polymer solar cells," *J. Appl. Phys.*, vol. 111, no. 2, p. 024505, Jan. 2012.
 21. Y. P. Varshni, "Temperature dependence of the energy gap in semiconductors," *Physica*, vol. 34, no. 1, pp. 149–154, Jan. 1967.
 22. C. D. Thurmond, "The Standard Thermodynamic Functions for the Formation of Electrons and Holes in Ge, Si, GaAs, and GaP," *J. Electrochem. Soc.*, vol. 122, no. 8, pp. 1133–1141, Aug. 1975.
 23. P. Lautenschlager, M. Garriga, S. Logothetidis, and M. Cardona, "Interband critical points of GaAs and their temperature dependence," *Phys. Rev. B*, vol. 35, no. 17, pp. 9174–9189, Jun. 1987.

Arrived: 31. 08. 2016

Accepted: 22. 09. 2016

Linear Incremental Displacement Measurement System with Microtransformers

Matija Podhraški¹, Janez Trontelj²

¹Letrika Lab d.o.o., Šempeter pri Gorici, Slovenia

²Laboratory for Microelectronics, Faculty of Electrical Engineering, Ljubljana, Slovenia

Abstract: The paper discusses an inductive microsensor system for displacement measurement comprising microtransformers. The primary windings of the microtransformers are excited with an AC source with a frequency of several MHz. The microtransformers are fabricated in internal metal layers of an integrated circuit using a conventional 350 nm commercial CMOS process, along with corresponding circuits for the processing of the microtransformers' output signals. The major advantage of such system is its cost-effectiveness due to its straightforward fabrication and the absence of the need for an external field generator, such as permanent magnets at Hall Effect encoders or a light source at optical encoders.

In a linear incremental encoder application, microtransformer output signals are modulated by a metal measurement scale positioned over the integrated microsystem, resulting in a combination of amplitude and phase modulation. The integrated circuit employs a fully-differential measurement channel with three-stage amplification and a mixer implemented with a Gilbert cell: the signal is demodulated using synchronous demodulation.

A prototype microsystem was designed, fabricated and evaluated, demonstrating a sensitivity of 0.99 V/mm with a copper target at an approximate microsystem-target distance of 200-250 μm .

Keywords: inductive sensor; eddy-current sensor; displacement sensor; ASIC; microtransformer; linear encoder

Sistem z mikrotransformatorji za inkrementalno merjenje linearne pomika

Izveček: Prispevek obravnava induktivni mikrosenzorski sistem za merjenje pomika na osnovi mikrotransformatorjev. Primarna navitja mikrotransformatorjev so vzbujana z izmeničnim virom frekvence nekaj MHz. Mikrotransformatorji so izdelani v internih metalnih slojih integriranega vezja, proizvedenega s konvencionalnim 350 nm komercialnim CMOS procesom, pridružena pa so jim tudi ustrezna vezja za procesiranje izhodnih signalov mikrotransformatorja. Glavna prednost takšnega sistema je njegova cenovna učinkovitost zaradi preproste izdelave in odsotnosti potrebe po zunanjem generatorju polja, kot so npr. trajni magneti pri Hallovih enkoderjih oziroma svetlobni viri pri optičnih.

V aplikaciji linearne inkrementalne enkoderja so izhodni signali mikrotransformatorja modulirani s kovinsko merilno letvijo, nameščeno nad integriran mikrosistem, kar se odraža v kombinaciji amplitudne in fazne modulacije. Integrirano vezje vsebuje popolno diferencialni merilni kanal s trostopenskim ojačenjem in mešalnik, izveden z Gilbertovo celico: signal je sinhronsko demoduliran.

Zasnovan, izdelan in izmerjen je bil prototipni mikrosistem z doseženo odzivnostjo 0,99 V/mm pri bakreni tarči in oddaljenosti med tarčo in senzorjem približno 200-250 μm .

Ključne besede: induktivni senzorji; senzorji na vrtnične tokove; senzorji pomika; namensko integrirano vezje; mikrotransformatorji; linearni enkoder

* Corresponding Author's e-mail: matija.podhraski@si.mahle.com

1 Introduction

The main difference of inductive position sensing concept in comparison to conventional magnetic encoders (which are based on Hall or magnetoresistive sensors) is in the use of an alternating magnetic field instead of a stationary magnetic field; sensors employ the principle of electromagnetic induction.

Two major types of inductive sensors are used [1], [2]. The first type is a dual-coil structure, similar to a transformer. The first coil is connected to an AC source, inducing the voltage in the second coil. If a conductive object is moved close to the coils, eddy currents are induced in the object. Due to the loss of energy through this mechanism, the voltage in the secondary coil is reduced [3]. The effect on the secondary voltage is adversary in the presence of a ferromagnetic object, improving the magnetic coupling between the coils [3]. The second type is based on the change of the coil inductance under the effect of a nearby object: if a coil is wired into a resonant circuit, its oscillation frequency changes when the object moves [2].

Inductive sensors benefit from their insensitivity to dust, which stands out as a strong advantage in an industrial environment in comparison to the optical sensors [4].

Magnetic and optical position encoders can be fabricated as application-specific integrated circuits (ASICs). However, for their use, external placement of magnetic field source or light source is needed. Inductive sensors are free from this requirement, since they generate the high frequency magnetic field by an integrated inductor. In this paper, we present a microelectronic implementation of a prototype inductive linear position encoder, operating with a passive measurement scale. The sensor elements are realized as microtransformers with the accompanying electronics fabricated together with the microtransformers in an ASIC using an unmodified 350 nm CMOS process.

2 Design

The discussed system operates similarly as a linear variable differential transformer (LVDT), as well as an eddy current sensor [1–3], [5]. The sensor is scaled to the size of a typical integrated circuit (several square millimeters). The design of the microtransformer setup used in the sensor is shown in Figure 1. Figure 2 displays the differential operation of the microtransformer. When a full half-period of a ferromagnetic scale is positioned over the first microtransformer, the coupling between

the primary and the secondary winding is the strongest for this microtransformer. Contrarily, the coupling is then the weakest for the second microtransformer as the void half-period is positioned over it [2], [3].

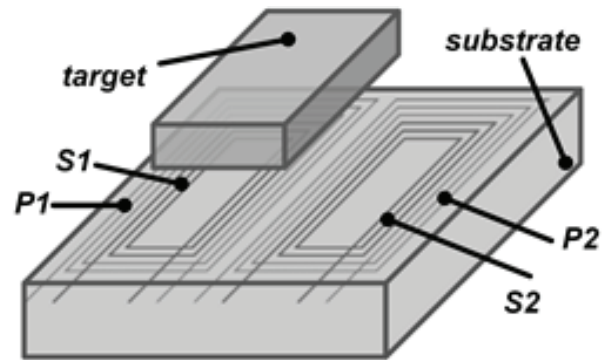


Figure 1: The structure of a microtransformer pair (P – primary, S – secondary winding) [2].

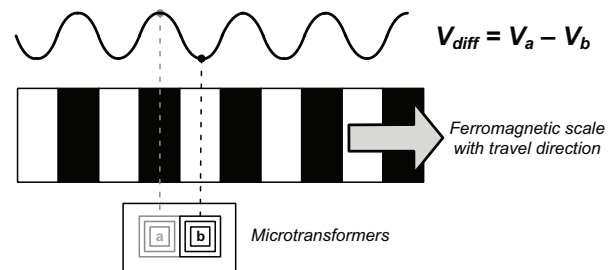


Figure 2: The differential operation of a microtransformer pair [2].

The differential voltage of the microtransformer pair V_{diff} is obtained by subtracting the secondary voltages of microtransformers V_a and V_b [3]. In the described situation (Figure 2), V_{diff} amplitude is maximal. As the scale

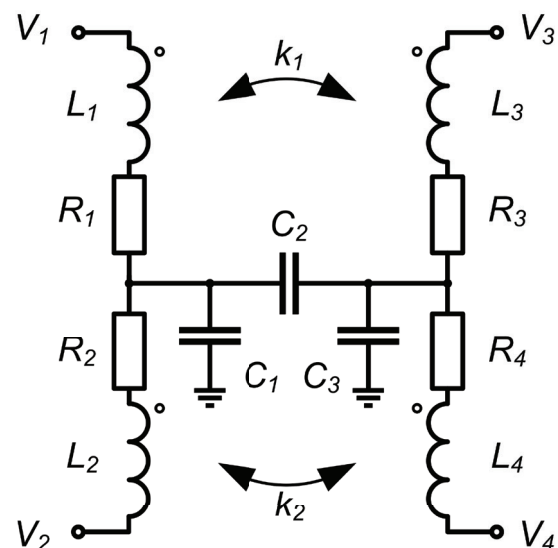


Figure 3: A model circuit of a microtransformer [3].

moves, the outputs change periodically. It should be noted that for a conductive (non-ferromagnetic) scale, the operation is adversary [5]. When a microtransformer is completely covered with a part of non-ferromagnetic metal, its induced voltage is minimal due to energy dissipation in the scale through the mechanism of eddy currents [3].

Using the presented differential principle, the signals which are common to both microtransformers in a pair (such as EMI and the capacitively transferred voltage) are subtracted [5].

The general design of the microsystem is presented in Figure 5 (a). It consists of a silicon die comprising the microtransformers along with analog front-end electronics for the generation of the differential signal [3]. The microtransformers are fabricated using standard CMOS technology metal layers. The total layer count is four. The external dimensions of the microtransformer primary and secondary windings are 755 by 500 μm and 576 by 314 μm , respectively [3]. Therefore the scale period P is 1 mm. Each winding of a microtransformer has 45 turns: three layers with 15 turns per layer are used, while the top metal layer is used for routing the connections [3]. The winding structure for a single winding is shown in Figure 4. Such structure is used for reducing the interwinding capacitance [3]. A model circuit of a microtransformer is shown in Figure 3, with the accompanying component values given in Table 1. Such circuit is insufficient to model the effects of the measurement scale on the output voltage of a microtransformer. So, finite element modeling was used to acquire the modulation characteristics as described in [3], [6].

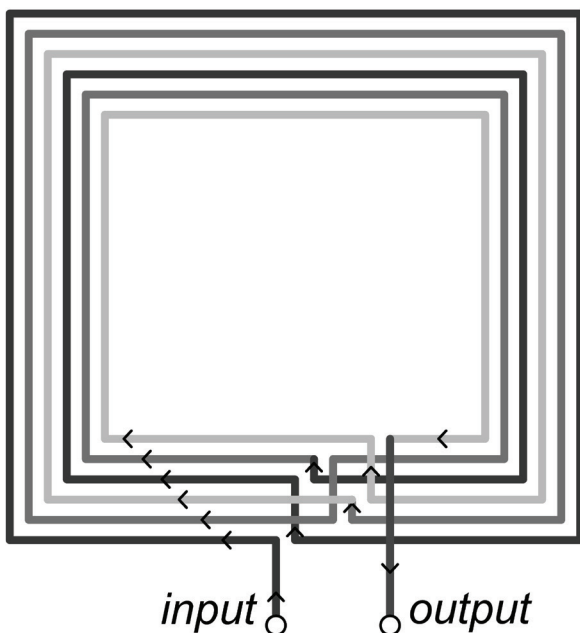


Figure 4: The microtransformer winding design [3].

Table 1: Component values in the model circuit [3].

Components	Value
R_1, R_2	2657 Ω
R_3, R_4	1816 Ω
L_1, L_2	1.16 μH
L_3, L_4	658 nH
C_1	3.55 pF
C_2	3.4 fF
C_3	2.39 pF
k_1, k_2	0.429

To improve the signal-to-noise ratio of the system, the output signals of the coils with same position relative to the scale period can be summed, as shown in Figure 5 (b). The primary windings are wired in parallel [2].

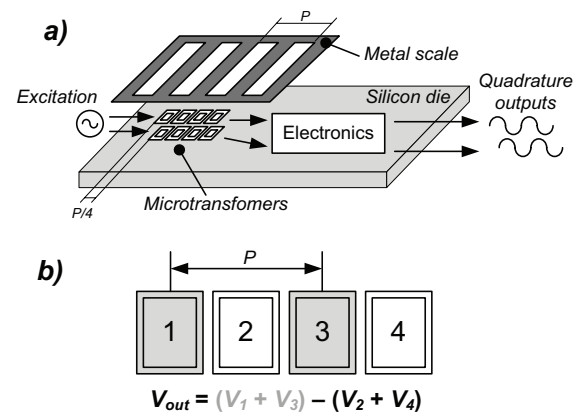


Figure 5: (a) A block representation of the presented microsystem with a metal scale of period P and quadrature output signals. (b) The implemented summation scheme [2].

The device comprises two channels shifted for a quarter of the scale period, i.e. quadrature output signals [3]. The quadrature principle is commonly employed in position encoders (e.g. optical [7] and Hall devices [8]), relying on (multiples of) two sensor elements with their position shifted by a half of the primary coil width (i.e. $\frac{1}{4}$ of the scale period P). Observing the phase shift of the quadrature signals allows the determination of the movement direction. If the signals have a sinusoidal shape, the arctangent function of their amplitude ratio enables a straightforward calculation of the displacement inside a single half-period [3].

$$x = \arctan\left(\frac{\sin x}{\cos x}\right) \tag{1}$$

A block diagram of a single measurement channel as implemented in the integrated circuit is shown in Figure 8. A fully differential channel setup is used, with

the subtraction of the positive and negative microtransformer output signal performed at the end of the chain (Stage 3).

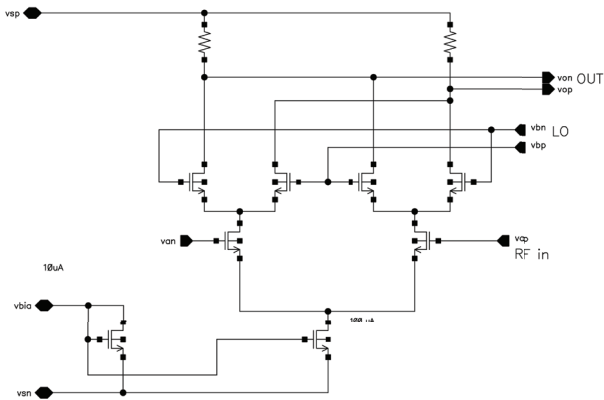


Figure 6: The Gilbert cell mixer implemented in the ASIC [6].

The first amplifier is wideband (72 MHz GBW), employing telescopic topology [3]. Then, the signal is mixed down to DC using a differential Gilbert cell CMOS mixer [6], shown in Figure 6. In the next two stages, signals are amplified at the baseband, also filtering out the remaining HF signal components [3].

3 Evaluation

To evaluate the performance of the microsystem, it was placed on a mechanical micromanipulator controlled by a computer, which was used to displace a measurement scale. Two scales (Figure 7) were used: scale (1) was made by laser cutting from transformer steel sheet

(0.35 mm thickness), and the second (2) was fabricated as a PCB (35 μm copper thickness) [3]. Due to the presence of gel coating needed for the IC protection, the thickness between the scale and the surface of the IC was no less than 250-300 μm [3].



Figure 7: Scales used for the evaluation [3].

First, the excitation frequency and the phase of the mixing signal were swept to determine the optimal parameters. The maximal peak-to-peak amplitude of the output signal was chosen as the figure of merit [3].

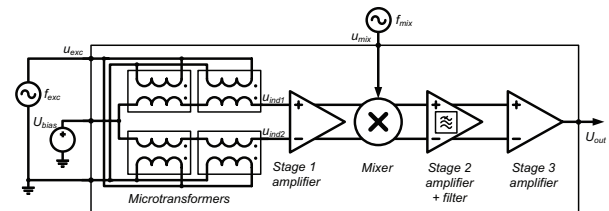


Figure 8: a block diagram of a single measurement channel implemented in the ASIC [3].

The output characteristics were recorded at the optimal excitation frequency f_{exc} and mixing signal phase φ_{mix} for the copper and steel scale with 20 μm positioning step. The results are given in Figure 9. The sensitivity S of the microsystem is defined (Equation 2) as the change of the output peak-to-peak voltage over a scale period P [3]:

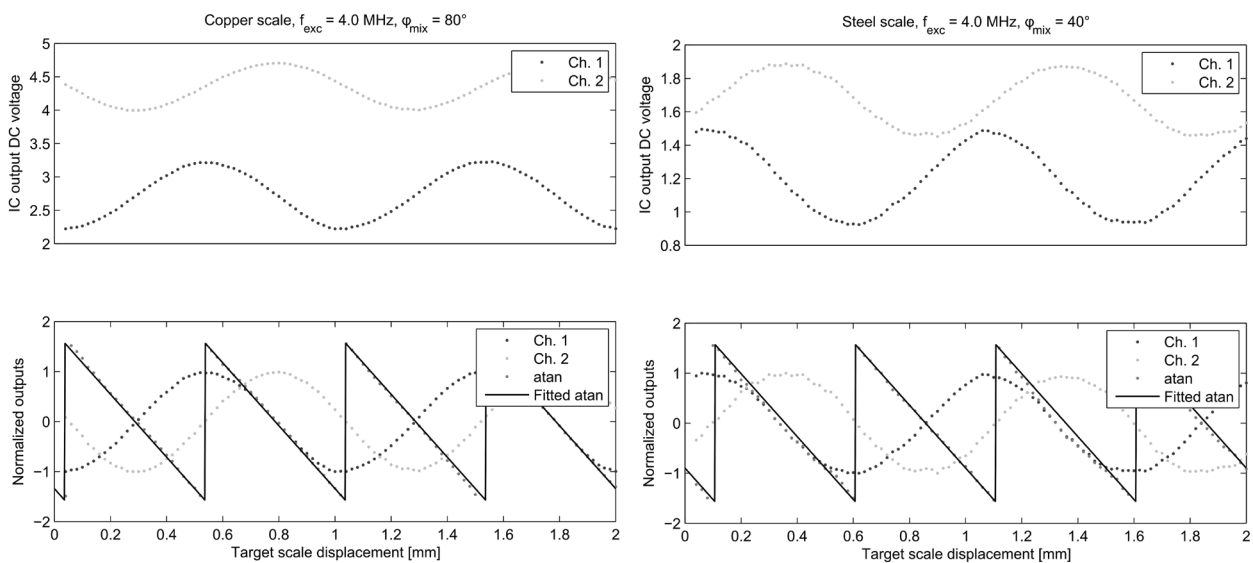


Figure 9: ASIC characterization results for both scale types. Results are compared to an ideal arctangent function.

$$S = \frac{\Delta U_{pp}}{P} \left[\frac{\text{V}}{\text{mm}} \right] \quad (2)$$

Sensitivities for the two scales as well as maximum and RMS values of the linearity error E are given in Table 2.

Table 2: Summarized measurement results [3].

	Copper scale	Steel scale
S (Ch. 1)	0.99	0.57
S (Ch. 2)	0.71	0.44
max (E)	18.79	33.05
rms (E)	6.89	11.32

4 Conclusion

The design and the evaluation of an integrated micro-transformer linear position measurement system were demonstrated. The system was evaluated with two scale types. It was discovered that various scales have different optimal excitation frequencies and phases of the mixing signal [3]. Therefore, a system should be adaptable to support the variation of these parameters. Considering the microtransformer sensitivity as well as the linearity error, better results were observed with the copper scale.

In our future work, we intend to redesign the measurement channel to reduce measurement noise by moving the major part of the amplification to the first amplifying stage, and to implement an on-chip frequency and phase-tunable oscillator, resulting in a true single-chip linear position encoder, having a significant potential for the encoder industry due to its cost-efficiency.

5 References

1. M. Podhraški and J. Trontelj, "Design and evaluation of a microcoil proximity sensing microsystem," *Conf. 2015 Proc. 51th Int. Conf. Microelectron. Devices Mater. Workshop Terahertz Microw. Syst. Sept. 23 - Sept. 25 2015 Bled Slov.*, vol. 2015, pp. 95–99, 2015.
2. M. Podhraški and J. Trontelj, "An integrated micro-transformer system for displacement measurement," *Inf. MIDEM*, vol. 46, no. 1, pp. 29–35, 2016.
3. M. Podhraški and J. Trontelj, "A Differential Monolithically Integrated Inductive Linear Displacement Measurement Microsystem," *Sensors*, vol. 16, no. 3, p. 384, Mar. 2016.
4. A. J. Fleming, "A review of nanometer resolution position sensors: Operation and performance," *Sens. Actuators Phys.*, vol. 190, pp. 106–126, Feb. 2013.
5. J. W. Bergqvist, Y. de Coulon, and H. de Lambilly, "Device for detecting position and movement by using magnetic field variation," US6043644 A, 28-Mar-2000.
6. M. Podhraški, "Integrirani mikrosenzorski sistemi z mikrotuljavicami," Univerza v Ljubljani, Ljubljana, 2016.
7. J. Rozman and A. Pletersek, "Linear Optical Encoder System With Sinusoidal Signal Distortion Below 60 dB," *IEEE Trans. Instrum. Meas.*, vol. 59, no. 6, pp. 1544–1549, Jun. 2010.
8. H. V. Hoang and J. W. Jeon, "Signal compensation and extraction of high resolution position for sinusoidal magnetic encoders," in *International Conference on Control, Automation and Systems, 2007. ICCAS '07, 2007*, pp. 1368–1373.

Arrived: 31. 08. 2016

Accepted: 22. 09. 2016

Control of electrical conductivity in 0.7BiFeO_3 - 0.3SrTiO_3 ferroelectric ceramics via thermal treatment in nitrogen atmosphere and Mn doping

Maja Makarovič^{1,2}, Julian Walker³, Evgeniya Khomyakova^{1,2}, Andreja Benčan^{1,2}, Barbara Malič^{1,2} and Tadej Rojac^{1,2}

¹Jožef Stefan Institute, Ljubljana, Slovenia

²Jožef Stefan International Postgraduate School, Ljubljana, Slovenia

³Materials Research Institute, Pennsylvania State University, USA

Abstract: In this work, the solid solution between polar BiFeO_3 (BFO) and non-polar SrTiO_3 (ST) with the composition $0.7\text{BFO}-0.3\text{ST}$ has been prepared by mechanochemical activation-assisted synthesis with particular emphasis on the characterization and control of the electrical conductivity of the resulting ceramics. According to X-ray diffraction analysis and scanning electron microscopy the incorporation of ST into BFO minimizes the formation of secondary phases, typically formed during the synthesis of unmodified BFO. The as-sintered ceramics exhibited a high electrical conductivity, which was suppressed by post-annealing in N_2 atmosphere. However, this approach showed two major drawbacks: i) re-oxidation of samples and thus increase in their conductivity when annealed in air to elevated temperatures (up to $\sim 450^\circ\text{C}$) and ii) increased conductivity by application of high electrical fields, resulting in a strong leakage-current contribution to the measured polarization-electric-field hysteresis loops. For these reasons, in order to reduce the conductivity, we propose here an alternative approach, i.e., doping with MnO_2 . Using the doping, the specific conductivity has been decreased and did not deteriorate when the samples were heated in air to elevated temperatures. Unlike in the case of N_2 -annealed samples, in the doped samples, saturated ferroelectric loops with negligible leakage-current contributions have been measured, revealing a coercive field of $E_c \sim 80 \text{ kV/cm}$ and a remanent polarization of $2P_r \sim 100 \mu\text{C/cm}^2$.

Keywords: ferroelectric; BiFeO_3 - SrTiO_3 ; electrical conductivity

Kontrola električne prevodnosti v feroelektrični keramiki 0.7BiFeO_3 - 0.3SrTiO_3 z žganjem v dušikovi atmosferi in dopiranjem z Mn

Izvleček: V tem prispevku smo z mehanokemijsko aktivacijo pripravili trdno raztopino med polarnim BiFeO_3 (BFO) in nepolarnim SrTiO_3 (ST) s sestavo $0.7\text{BFO}-0.3\text{ST}$, pri čemer je bil poseben poudarek na karakterizaciji ter kontroli električne prevodnosti pripravljene keramike. Glede na rezultate rentgenske praškovne difrakcije in vrstične elektronske mikroskopije, vgradnja ST v BFO zmanjša koncentracijo sekundarnih faz v keramiki, ki sicer tipično nastajajo pri sintezi nemedificiranega BFO. Tako pripravljena BFO-ST keramika je pokazala visoko električno prevodnost, ki pa je bila uspešno zmanjšana z naknadnim žganjem pri 750°C v atmosferi N_2 . Kljub temu je ta pristop pokazal dve pomanjkljivosti: i) ponovno oksidacijo ter posledično povečanje električne prevodnosti vzorcev, po tem ko so bili na zraku izpostavljeni povišanim temperaturam ($\sim 450^\circ\text{C}$) ter ii) povečanje prevodnosti pri visokem električnem polju, kar se odraža v velikem prispevku enosmernega električnega toka k izmerjeni histerezni zanki polarizacije v odvisnosti od električnega polja. Zaradi navedenih razlogov, smo se za zmanjševanje prevodnosti odločili za alternativni pristop, tj. dopiranje z MnO_2 . Z uporabo tega pristopa je bila specifična prevodnost zmanjšana in se ni spremenila po segrevanju vzorcev na zraku pri povišanih temperaturah. Za razliko od vzorcev žganih v atmosferi N_2 , je bil v zankah dopiranih vzorcev razviden zanemarljiv prispevek prevodnosti materiala; vrednost koercitivnega polja je bila $E_c \sim 80 \text{ kV/cm}$, remanentne polarizacije pa $2P_r \sim 100 \mu\text{C/cm}^2$.

Ključne besede: feroelektrik; BiFeO_3 - SrTiO_3 ; električna prevodnost

* Corresponding Author's e-mail: maja.makarovic@ijs.si

1 Introduction

Bismuth ferrite, BiFeO_3 (BFO), is of interest due to its ferroelectric and antiferromagnetic properties at room temperature and due to its high Curie temperature ($\sim 820^\circ\text{C}$), which make BFO a prime candidate for high-temperature piezoelectric applications [1]. The practical use of BFO has, however, been limited by several factors, including: i) the difficulty to prepare single-phase BFO in bulk form without the presence of secondary phases, which is related to the thermodynamic phase instability of BFO at the temperature range of ceramics processing, ii) the high electrical conductivity due to the mixed valence state $\text{Fe}^{4+}/\text{Fe}^{3+}/\text{Fe}^{2+}$ and iii) the high coercive field for ferroelectric domain switching [2]. One method to suppress the formation of secondary phases, improve the electrical insulation and maintain a relatively high Curie temperature is the incorporation of other ABO_3 perovskites, such as PbTiO_3 (PT)[3], CaTiO_3 (CT)[4], BaTiO_3 (BT)[5] and SrTiO_3 (ST)[6], in solid solutions with BFO. Pseudo-binary BFO- ABO_3 solid solution systems between BFO and other perovskites is also of great interest because of the possibility of inducing a morphotropic phase boundary (MPB) where piezoelectric properties are enhanced [7].

It has been shown in several cases that BFO-based solid solutions still exhibit high electrical conductivity. As a result, additional methods to improve the electrical insulation are required. In BFO, which is a p-type conductor, one such method is the annealing of the ceramics in an inert atmosphere with low partial pressure of oxygen, e.g., N_2 [8]. Another method is chemical doping with, e.g., La, Ga, Ti and Mn [5, 9–11]. In particular, Mn doping has been shown to be highly effective in improving the electrical resistivity of BFO-BT ceramics.

Among the BFO-based solid solutions, the solid solution between polar BFO and non-polar ST has been less investigated with little literature data regarding its electrical and electromechanical properties [6, 12, 13]. The dielectric and magnetic properties of this system as well as the potential to exhibit an MPB between a polar and non-polar phase, for which a large piezoelectric response has recently been predicted [14], make this solid solution system particularly interesting.

The aim of this work was to prepare a BFO-ST solid solution in the rhombohedral (ferroelectric) region of the phase diagram reported by Fedulov [6] with the composition containing 70 mol% of BFO (0.7BFO-0.3ST), and to measure the dielectric and ferroelectric properties. Dense ceramics with minimum amount of inhomogeneities were prepared by an alternative processing method, i.e., mechanochemical activation-assisted synthesis. In particular, the effect of post-annealing in

nitrogen and Mn doping on the electrical conductivity was investigated.

2 Experimental work

2.1 Synthesis of the solid solution

The solid solution with the composition 0.7BiFeO_3 - 0.3SrTiO_3 (0.7BFO-0.3STO) was prepared by mechanochemical activation-assisted synthesis using Bi_2O_3 (99.999%, Alfa Aesar), Fe_2O_3 (99.998%, Alfa Aesar), TiO_2 (99.8%, Alfa Aesar) and SrCO_3 (99.994% Alfa Aesar) as starting powders. After being separately milled in an absolute ethanol, the powders were weighed according to the stoichiometric ratio in a 35 g mixture and homogenized in a planetary mill (Retsch PM 400, Retsch, Haan, Germany) at 200 min^{-1} for 4 h in absolute ethanol. The mixture was then dried and high-energy milled in a Fritsch Pulverisette 7 Vario-Mill (Fritsch GmbH, Idar-Oberstein, Germany) for 40 h in an 80-ml tungsten carbide vial, filled with 14 tungsten carbide milling balls with diameters of 10 mm. The disk rotational frequency and the vial-to-disk rotational frequency were set to, respectively, 300 min^{-1} and -2 (the negative sign denotes the opposite directions of the rotations of the vial and the disk). After the high-energy milling, the mixture was re-milled in a planetary mill in an absolute ethanol at 200 min^{-1} for 4 h. Finally, the powder was dried, pressed into pellets with 150 MPa of uniaxial pressure and sintered in air at 1025°C for 2 h using a heating/cooling rate of $5^\circ\text{C}/\text{min}$.

2.2 Post-annealing in N_2

In order to reduce the electrical conductivity of the samples, the sintered samples were post-annealed in N_2 atmosphere. The samples were annealed in a nitrogen gas flow (N_2 4.6, Messer) at 750°C for 1 h with a heating/cooling rate of $2^\circ\text{C}/\text{min}$.

2.3 Mn doping

0.1 wt% of pre-milled MnO_2 (99.9%, Alfa Aesar) was added to the activated (high-energy milled) powder. The mixture was homogenized in a planetary mill with absolute ethanol at 200 min^{-1} for 4 h. The powders were then pressed into pellets and sintered in air at 1025°C for 2 h using a heating/cooling rate of $5^\circ\text{C}/\text{min}$.

2.4 Characterization of the sintered ceramics

The relative geometric density of sintered ceramics was determined using the theoretical density of 0.7BFO-0.3ST solid solution ($7.40\text{ g}/\text{cm}^3$). This theoretical den-

sity was evaluated based on the theoretical density of individual perovskites, i.e., BFO (8.34 g/cm) and ST (5.12 g/cm), and their volume proportion in the solid solution.

The phase composition of sintered ceramics was determined using X-ray powder diffraction (XRD) analysis (PANalytical X'Pert PRO diffractometer with $\text{CuK}\alpha_1$ radiation). The XRD patterns were recorded in a 2θ -range from 20° to 78° with a step of 0.016° and an acquisition time of 100 s. The microstructure of sintered ceramics was examined by field emission scanning electron microscope (FE-SEM, JSM-7600F, Jeol) equipped with a LINK ISIS 300 (Oxford Instruments, Abingdon, U.K.) energy dispersive X-ray spectrometer (EDXS).

For characterization of electrical properties, the sintered pellets were thinned to ~ 0.2 mm, polished and electroded with Au by sputtering. The dielectric permittivity and loss tangent as a function frequency were analyzed in the range 10^6 - 10^2 Hz using a HP4284A impedance analyzer (frequency range 10^6 - 10^2 Hz) and Kistler charge amplifier (frequency range 10^3 - 10^2 Hz). High-electric-field polarization and strain hysteresis loops were measured by applying to the samples single sinusoidal electric-field waveforms using an aixACCT TF 2000 analyzer equipped with a laser interferometer.

3 Results and discussion

3.1 Phase composition

Figure 1 shows the XRD patterns of 0.7BFO-0.3ST solid solution along with the end members of the solid solution (BFO and ST) for reference. The XRD pattern of 0.7BFO-0.3ST confirms the presence of the perovskite phase with no detectable secondary phases. By close inspection of the peaks of BFO and ST belonging to the $\{111\}_{pc}$ (pc denotes pseudo cubic notation) family of crystallographic planes (Figure 1 inset), it can be observed that BFO exhibits a pronounced $\{111\}_{pc}$ splitting to $(111)_{pc}$ and $(1\bar{1}\bar{1})_{pc}$ peaks due to the rhombohedral unit-cell distortion, while ST exhibits a single (111) peak because of its cubic structure. Relative to BFO, BFO-ST exhibit a much weaker $\{111\}_{pc}$ peak splitting, indicating that the structure is probably still rhombohedral but with a decreased lattice distortion (rhombohedral angle closer to 90° , where 90° corresponds to cubic lattice)

With respect to BFO, all perovskite peaks of BFO-ST are shifted towards higher 2θ angles, indicating a contraction in unit cell volume by the addition of ST to BFO.

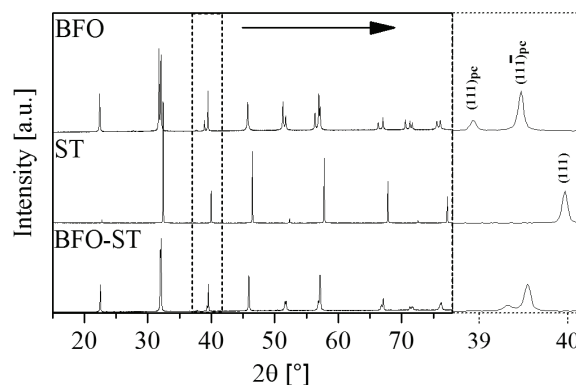


Figure 1: XRD patterns of BFO, ST and 0.7BFO-0.3ST solid solution. The inset on the right side of the figure shows an enlarged view of the peaks belonging to the $\{111\}_{pc}$ family of crystallographic planes.

3.2 Microstructure

The microstructure and phase composition of the sintered ceramics were investigated by FE-SEM (Figure 2). The ceramics exhibit a dense microstructure, consistent with the measured relative density (ρ_{rel}) of $\sim 97\%$. The chemical homogeneity of the rhombohedral perovskite matrix phase was investigated using EDXS analysis performed on 14 randomly selected points. The standard deviations calculated over all measurements for Bi, Fe, Sr and Ti were 0.7, 1.2, 1.9 and 2.1 %, respectively. The uncertainty of a standard-less EDS analysis was reported to be $\pm 5\%$ relative [15]. These results show that the deviations within the analyzed sample are smaller than the uncertainty of the method, indicating the homogeneous distribution of the elements. However, a closer inspection of the microstructure (see the inset in Figure 2) revealed small, submicron sized

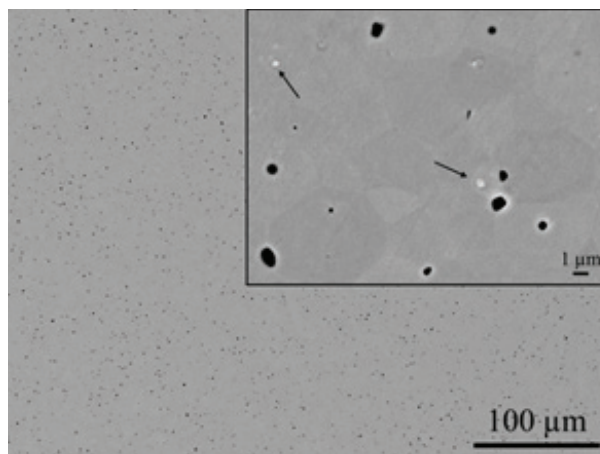


Figure 2: Backscattered electron SEM micrograph of sintered 0.7BFO-0.3ST ceramics. The inset on the right side shows inhomogeneities (marked with arrows).

chemically inhomogeneous inclusions, the concentration of which is evidently insufficient to be detected by XRD, since the ceramics was identified as single phase using XRD analysis (Figure 1).

3.3 Dielectric properties

The real part of the complex dielectric permittivity (ϵ'), the dielectric loss tangent ($\tan\delta$) and the real part of the complex electrical conductivity (σ') were studied as a function of frequency for the 0.7BFO-0.3ST ceramics. The real part of the electrical conductivity σ' for each frequency data point was calculated from the measured imaginary dielectric permittivity (ϵ_d'') and frequency ω using equation (1):

$$\sigma' = \omega \epsilon_0 \epsilon_d'' \quad (1)$$

where ϵ_0 is the permittivity of vacuum.

Four different samples have been analyzed: i) as-sintered (undoped) ceramics (\square), which was ii) post-annealed in N_2 at 750 °C (\circ), and iii) additionally annealed in air at ~450 °C after the N_2 annealing (\bullet) and iv) Mn-doped ceramics (∇).

The as-sintered ceramics (Fig. 3, \square) exhibit two relaxations in the measured frequency range, observed as two step-like features in ϵ' within the frequency range 10^1 - 10^5 Hz, which are accompanied by two peaks in $\tan\delta$. These relaxations result in high apparent ϵ' values at the low frequency limit ($\epsilon' > 10^5$ below 10^{-2} Hz). Such relaxation behavior in BFO has been earlier attributed to either Maxwell Wagner-like or polaron hopping conduction mechanisms [2], both in principle related to the elevated electrical conductivity of the ceramics.

After the sintered 0.7BFO-0.3ST ceramics were annealed in N_2 , the dielectric relaxations were largely suppressed (Fig. 3, \circ). From the frequency dependent σ' , it is possible to estimate the specific electrical conductivity (σ_0) using further expansion of equation 1 into equation 2:

$$\sigma' = \sigma_0 + \omega \epsilon_0 \epsilon_d'' \quad (2)$$

where ϵ_d'' is the imaginary part of the dielectric permittivity related to dielectric (or polarization) losses. At low frequencies, if the term $\omega \epsilon_0 \epsilon_d''$ is sufficiently small, σ' in principle reaches a plateau and σ_0 can be estimated as $\sigma' \approx \sigma_0$. Even though this plateau in σ' has not been reached in the as-sintered (Fig. 3c, \square) and N_2 -annealed (Fig. 3c, \circ) samples, the lower values of σ' of the last-mentioned sample in the low-frequency range indicate a reduction of the electrical conductivity, possibly related to the reduction of Fe^{4+} to Fe^{3+} ions during N_2 -annealing as earlier reported for BFO. [8] However,

after the same sample was annealed at ~450 °C in air, the dielectric relaxation was again observed. Therefore, the results suggest that the sample re-oxidizes during annealing in air, meaning that the annealing in N_2 has limited practical implications in reducing efficiently the electrical conductivity of BFO-ST.

Similar as in the case of N_2 -annealing, Mn doping suppressed the dielectric relaxation originally observed in the as-sintered and undoped sample, resulting in a similar ϵ' , $\tan\delta$ and σ' . In a strong contrast, however, the electrical conductivity and the associated relaxation of this doped composition did not deteriorate after the sample was heated in air at ~450 °C (not shown).

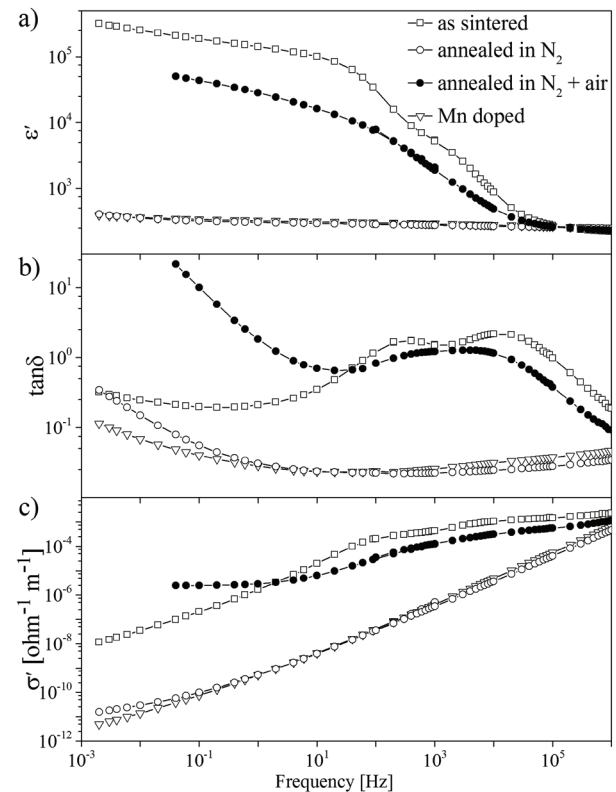


Figure 3: a) Room-temperature real part of complex dielectric permittivity (ϵ'), b) dielectric loss tangent ($\tan\delta$) and c) real part of complex electrical conductivity (σ') as a function of frequency for 0.7BFO-0.3ST as-sintered ceramics (\square), annealed in N_2 at 750 °C (\circ) and additionally annealed in air at 450 °C (\bullet), and doped with MnO_2 (∇).

3.4 Ferroelectric properties

The polarization-electric-field (P-E) hysteresis loops of 0.7BFO-0.3ST ceramics annealed in N_2 and doped with Mn are shown in Figure 4. The loops were measured at room temperature at 120 kV/cm and frequency of 100 Hz and 10 Hz for the annealed and the doped sample, respectively. The test frequencies were different be-

cause the N_2 -annealed ceramics experienced high leakage currents and dielectric breakdown at test frequencies below 100 Hz. Despite the difference in the test frequency, the comparison of the loops can still be used to achieve a qualitative assessment of the different high electric-field behavior of each ceramic. The P-E loop of the N_2 -annealed sample is not saturated and shows high leakage-current contribution, evidenced by the rounded shape of the loop. On the contrary, the P-E loop of Mn-doped sample shows approximately saturated loops, signified by the sharp corners at the maximum and minimum electric fields, with the coercive field $E_c \sim 80$ kV/cm and remanent polarization $2P_r \sim 100 \mu\text{C}/\text{cm}^2$. The inset on the right side of the figure shows the loops for the corresponding samples at 10 kV/cm. By comparing the loops of the N_2 annealed sample at 10 kV/cm and 120 kV/cm it can be observed, that there is an abrupt increase in conductivity at high electrical fields, which results in strong leakage-current contribution to the measured polarization-electric-field loops (rounded loop in Fig. 4).

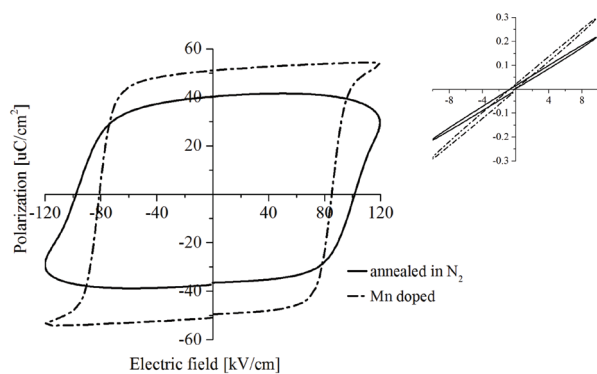


Figure 4: Room temperature P-E loops of 0.7BFO-0.3ST ceramics annealed in N_2 and Mn doped measured at 120 kV/cm. The inset on the right side shows P-E loops of the same samples measured at 10 kV/cm.

4 Conclusions

In the present report, ceramics with composition 0.7BFO-0.3ST were prepared by mechanochemical activation-assisted synthesis, with high chemical homogeneity and high bulk density. The as-sintered samples exhibited high electrical conductivity, which was successfully suppressed by i) post-annealing of the sintered samples in a nitrogen flow or ii) doping with Mn. However, the exposure of the annealed samples to elevated temperature in air resulted in re-oxidation of the samples and consequently re-gain of the high electrical conductivity. In addition, the P-E loops of post-annealed samples showed increased conductivity at high electrical fields, resulting in leakage-current

dominated P-E loops. In contrast to the post-annealing in N_2 atmosphere, the doping with Mn has been proven as an efficient method to reduce the electrical conductivity in this system. As expected, the conductivity of Mn-doped samples did not deteriorate when heated in air to elevated temperatures. The P-E loops were saturated with $E_c \sim 80$ kV/cm and $2P_r \sim 100 \mu\text{C}/\text{cm}^2$.

5 Acknowledgments

This work was supported by the Slovenian Research Agency (program P2-0105 and project J2-5483).

6 References

1. G. Catalan and J. F. Scott, "Physics and Applications of Bismuth Ferrite," *Adv. Mater.*, vol. 21, no. 24, pp. 2463–2485, Jun. 2009.
2. T. Rojac, A. Bencan, B. Malic, G. Tutuncu, J. L. Jones, J. E. Daniels, and D. Damjanovic, "BiFeO₃ Ceramics: Processing, Electrical, and Electromechanical Properties," *J. Am. Ceram. Soc.*, vol. 97, no. 7, pp. 1993–2011, Jul. 2014.
3. T. P. Comyn, S. P. McBride, and a. J. Bell, "Processing and electrical properties of BiFeO₃-PbTiO₃ ceramics," *Mater. Lett.*, vol. 58, pp. 3844–3846, 2004.
4. Q. Q. Wang, Z. Wang, X. Q. Liu, and X. M. Chen, "Improved Structure Stability and Multiferroic Characteristics in CaTiO₃-Modified BiFeO₃ Ceramics," *J. Am. Ceram. Soc.*, vol. 95, pp. 670–675, 2012.
5. S. O. Leontsev and R. E. Eitel, "Dielectric and Piezoelectric Properties in Mn-Modified (1-x)BiFeO₃-xBaTiO₃ Ceramics," *J. Am. Ceram. Soc.*, vol. 92, no. 25823, pp. 2957–2961, 2009.
6. Y. N. Fedulov, S.A., Pyatigorskaya, I., Venevtsev, "An investigation of the BiFeO₃-SrTiO₃ system," *Sov. Phys. - Crystallogr.*, vol. 10, no. 3, pp. 291–296, 1965.
7. H. Jaffe, B., Cook, W.R.J., Jaffe, *Piezoelectric Ceramics*, US. New York: Academic Press, 1971, p. 316.
8. N. Masó and A. R. West, "Electrical Properties of Ca-Doped BiFeO₃ Ceramics: From p-Type Semiconduction to Oxide-Ion Conduction," *Chem. Mater.*, vol. 24, pp. 2127–2132, 2012.
9. J. R. Cheng, R. Eitel, and L. E. Cross, "Lanthanum-modified (1-x)(Bi_{0.8}La_{0.2})(Ga_{0.05}Fe_{0.95})O₃-xPbTiO₃," *J. Am. Ceram. Soc.*, vol. 86, no. 12, pp. 2111–2115, 2003.
10. K. Kalantari, I. Sterianou, S. Karimi, M. C. Ferrarelli, S. Miao, D. C. Sinclair, and I. M. Reaney, "Ti-Doping to Reduce Conductivity in Bi_{0.85}Nd_{0.15}FeO₃ Ceramics," *Adv. Funct. Mater.*, vol. 21, pp. 3737–3743, 2011.

11. H. Yang, C. Zhou, X. Liu, Q. Zhou, G. Chen, H. Wang, and W. Li, "Structural, microstructural and electrical properties of $\text{BiFeO}_3\text{-BaTiO}_3$ ceramics with high thermal stability," *Mater. Res. Bull.*, vol. 47, no. 12, pp. 4233–4239, 2012.
12. S. Vura, P. S. Anil Kumar, A. Senyshyn, and R. Ranjan, "Magneto-structural study of the multiferroic $\text{BiFeO}_3\text{-SrTiO}_3$," *J. Magn. Magn. Mater.*, vol. 365, pp. 76–82, 2014.
13. Z. Z. Ma, Z. M. Tian, J. Q. Li, C. H. Wang, S. X. Huo, H. N. Duan, and S. L. Yuan, "Enhanced polarization and magnetization in multiferroic (1-x) $\text{BiFeO}_3\text{-xSrTiO}_3$ solid solution," *Solid State Sci.*, vol. 13, no. 12, pp. 2196–2200, Dec. 2011.
14. D. Damjanovic, "A morphotropic phase boundary system based on polarization rotation and polarization extension," *Appl. Phys. Lett.*, vol. 97, no. 6, p. 062906, 2010.
15. J. Goldstein, D. Newbury, D. Joy, C. Lyman, P. Echlin, E. Lifshin, L. Sawyer, and J. Michael, *Scanning Electron Microscopy and X-Ray Microanalysis*, Third. New York: KluwerAcademic/Plenum Publisher, 2003.

Arrived: 31. 08. 2016

Accepted: 22. 09. 2016

Boards of MIDEM Society | Organi društva MIDEM

MIDEM Executive Board | Izvršilni odbor MIDEM

President of the MIDEM Society | Predsednik društva MIDEM

Prof. Dr. Marko Topič, University of Ljubljana, Faculty of Electrical Engineering, Slovenia

Vice-presidents | Podpredsednika

Prof. Dr. Barbara Malič, Jožef Stefan Institute, Ljubljana, Slovenia

Dr. Iztok Šorli, MIKROIKS, d. o. o., Ljubljana, Slovenija

Secretary | Tajnik

Olga Zakrajšek, UL, Faculty of Electrical Engineering, Ljubljana, Slovenija

MIDEM Executive Board Members | Člani izvršilnega odbora MIDEM

Prof. Dr. Slavko Amon, UL, Faculty of Electrical Engineering, Ljubljana, Slovenia

Darko Belavič, In.Medica, d.o.o., Šentjernej, Slovenia

Dr. Slavko Bernik, Jožef Stefan Institute, Ljubljana, Slovenia

Prof. DDr. Denis Đonlagič, UM, Faculty of Electrical Engineering and Computer Science, Maribor, Slovenia

Prof. Dr. Leszek J. Golonka, Technical University Wroclaw, Poland

Leopold Knez, Iskra TELA d.d., Ljubljana, Slovenia

Dr. Miloš Komac, UL, Faculty of Chemistry and Chemical Technology, Ljubljana, Slovenia

Prof. Dr. Miran Mozetič, Jožef Stefan Institute, Ljubljana, Slovenia

Jožef Perne, Zavod TC SEMTO, Ljubljana, Slovenia

Prof. Dr. Giorgio Pignatelli, University of Perugia, Italia

Prof. Dr. Janez Trontelj, UL, Faculty of Electrical Engineering, Ljubljana, Slovenia

Supervisory Board | Nadzorni odbor

Prof. Dr. Franc Smole, UL, Faculty of Electrical Engineering, Ljubljana, Slovenia

Mag. Andrej Piriš, Iskra-Zaščite, d. o. o., Ljubljana, Slovenia

Igor Pompe, Ljubljana, Slovenia

Court of honour | Častno razsodišče

Emer. Prof. Dr. Jože Furlan, UL, Faculty of Electrical Engineering, Slovenia

Franc Jan, Kranj, Slovenia

Prof. Dr. Drago Strle, UL, Faculty of Electrical Engineering, Slovenia

Informacije MIDE

Journal of Microelectronics, Electronic Components and Materials

ISSN 0352-9045

Publisher / Založnik:

MIDEM Society / Društvo MIDE

Society for Microelectronics, Electronic Components and Materials, Ljubljana, Slovenia

Strokovno društvo za mikroelektroniko, elektronske sestavne dele in materiale, Ljubljana, Slovenija

www.midem-drustvo.si